ALMA MATER STUDIORUM
UNIVERSITÀ DI BOLOGNA

DOTTORATO DI RICERCA IN

IL FUTURO DELLA TERRA, CAMBIAMENTI CLIMATICI E SFIDE SOCIALI

Ciclo 37

Settore Concorsuale: 04/A4 - GEOFISICA

Settore Scientifico Disciplinare: GEO/10 - GEOFISICA DELLA TERRA SOLIDA

NUMERICAL APPROACHES TO SLOPE ANALYSIS: STABILITY AND COLLAPSE DYNAMICS

Presentata da: Martina Zanetti

Coordinatore Dottorato

Prof. Silvana Di Sabatino

Supervisore

Prof. Filippo Zaniboni

Co-supervisore

Prof. Alberto Armigliato

Esame finale anno 2025

"Forty-two,"
said Deep Thought, with infinite majesty and calm.

Douglas Adams, The Hitchhiker's Guide to the Galaxy

Abstract

In the last decades, growing attention has been devoted to the phenomenon of landslides, due to their increasing frequency and impact on both human lives and infrastructure. Within this context, slope stability analysis has become a key tool in order to prevent and mitigate landslide damage.

This work presents a comprehensive investigation into slope stability analysis, applying different algorithms across a variety of environmental settings. Here, two numerical methods are employed: the Second Order Cone Programming Finite Element Method (SOCP-FEM) and the more traditional Limit Equilibrium Method in its Minimum Lithostatic Deviation (MLD) formulation. Their application to diverse geological settings is illustrated, particularly in synthetic slopes and real-case scenarios such as the seabed stability analysis offshore Vado Ligure, the Tavernola landslide near Lake Iseo and the Salse del Dragone mud volcano (all found in the Italian territory).

A novel strategy for determining the sliding surface is introduced, developed initially in a synthetic case and subsequently tested in the real-case scenario of the Tavernola landslide, which poses a potential risk of collapsing into Lake Iseo. Furthermore, we developed a Proof of Concept

to link stability analysis with landslide dynamics and the generation of waves, addressing the multi-hazard risks associated with landslide events in lake environments.
Additionally, the first comprehensive study of the Salse del Dragone mud volcano is outlined, integrating field surveys, seismic characterization, and stability analysis.

This thesis provides a structured methodology for addressing uncertainties inherent in slope stability analysis across diverse and data-limited environments. By integrating advanced numerical methods and developing a novel strategy for sliding surface determination, this work offers a flexible approach adaptable to various geological settings. The developed methodology enhances the understanding of multi-hazard risks, such as those associated with landslides in lake and offshore settings, supporting a more comprehensive and reliable assessment of slope stability.

Contents

List of acronyms

List of Figures

List of Tables

Chapter 1

Introduction

Landslides are movements of a mass of rock, debris or earth down a slope under the influence of gravity [15]. They can involve processes such as flowing, sliding, toppling, falling, or spreading, and many exhibit a combination of these movements, either simultaneously or at different stages throughout their duration [16].
A variety of factors contribute to slope instability and the occurrence of landslides, including precipitation, snow melt, temperature fluctuations, seismic activity, volcanic eruptions, and human interventions. Among these, climate plays a significant role, particularly in driving precipitation and temperature patterns [17], [18], [19]: these phenomena are expected to have an impact on slope stability across different timescales and regions [20], [16]. For instance, the synthesis report of the 2023 Intergovernmental Panel on Climate Change [21] states that "Cryosphere-related changes in floods, landslides, and water availability have the potential to lead to severe consequences for people, infrastructure and the economy in most mountain regions *(high confidence)*". Therefore, a growing attention has been devoted to the study of landslides and slope stability.

Figure 1.1 shows the worldwide distribution of fatal landslides from 2004 to 2016 reported in the global fatal landslide database (GFLD) [1].
The majority of landslides occur in Asia (almost 75%), primarily in regions such as the Himalayas, India and southeastern China. In South America they are concentrated along the Andes cordillera and Brazil, while in Central and North America fatal landslides are more common in Costa Rica, Nicaragua, Honduras, Guatemala, southern Mexico, and the Caribbean islands. Catastrophic landslides are widely distributed throughout Europe too, with a great

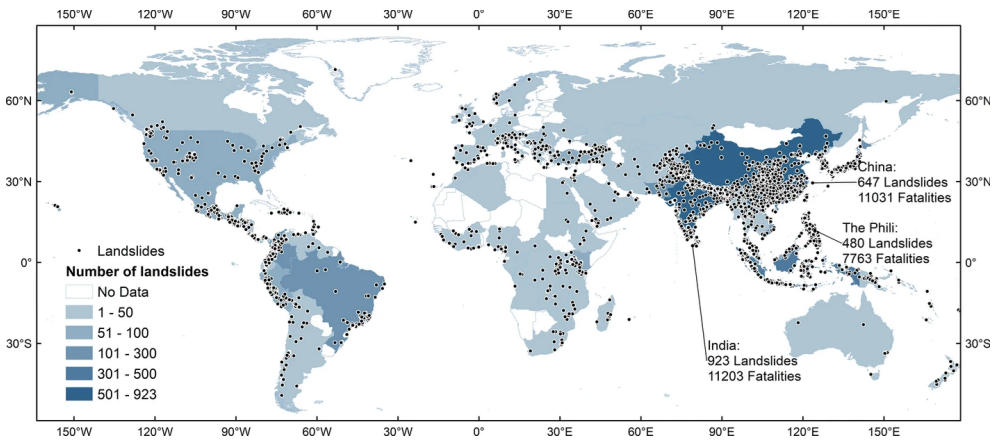

Figure 1.1. Worldwide distribution of fatal landslides from 2004 to 2016 reported in the global fatal landslide database [1].

concentration in mountainous areas. Moreover, almost 70% of them is situated on the Italian territory.

Focusing on the Italian territory, Figure 1.2 shows the map of landslide events with casualties from 1974 to 2023, retrieved from the Periodic Report on the Risk to the Italian Population from Landslides and Floods [2]. In the referred time period, landslides in Italy have caused 1087 casualties — including deaths and missing persons — over 1400 injuries, and more than 140000 evacuations across more than 1500 municipalities. These numbers clearly illustrate the frequency and severity of even small-scale landslides in Italy.
These statistics highlight the critical importance of studying slope stability, especially in a rapidly changing climate context. Improving our understanding and prediction of slope dynamics is crucial for the development of effective risk management strategies, which help reduce landslide impacts and protect lives and infrastructure.

The primary goal of this thesis is to establish a rigorous and comprehensive methodology for slope stability analysis, addressing the critical challenge of accurately assessing instability in the presence of significant uncertainties. Unlike traditional approaches, which often rely on oversimplified assumptions or limited parameter variations, this research proposes a refined, multi-method

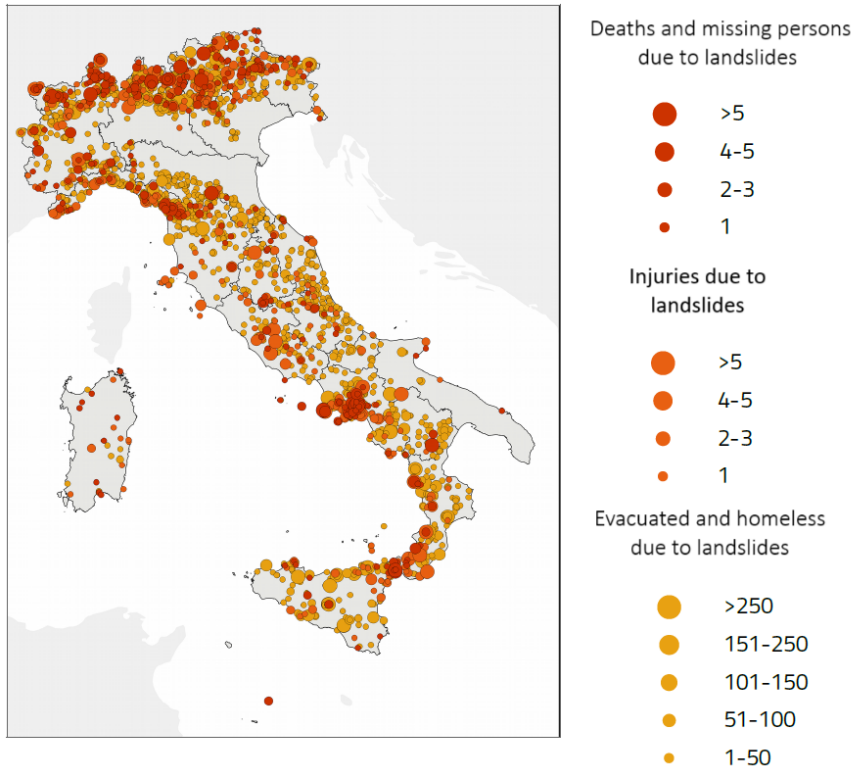

Figure 1.2. Map of landslide events with casualties in Italy from 1974 to 2023 [2].

framework that utilizes computational techniques to enhance reliability in geotechnical assessments.

This thesis presents an innovative strategy that leverages two advanced, two-dimensional stability analysis methods: the Second Order Cone Programming (SOCP)- Finite Element Method (FEM) and the Minimum Lithostatic Deviation (MLD) method. Each method brings distinct advantages—SOCP-FEM ensures mathematical robustness in optimization-based stability assessment, while the MLD method provides a refined approach to evaluating lithostatic stress deviations, addressing limitations in conventional Limit Equilibrium Methods (LEM). By combining these methodologies, the proposed

framework enhances the precision of stability evaluations and offers a structured approach for improved assessments.

A key innovation of this work is the multi-profile selection approach, which mitigates uncertainties associated with horizontal terrain variability. Unlike conventional single-profile methods, which may overlook localized instability mechanisms, this strategy captures spatial heterogeneity more effectively. Furthermore, in light of the often incomplete or absent data on geotechnical parameters, this methodology includes extensive parametric testing within realistic ranges. This approach not only identifies critical parameters that could induce soil failure but also provides insights into how well these parameters mirror actual conditions.

Moreover, unlike traditional methods that rely on predefined failure surfaces, this work introduces a methodology capable of identifying the slip surface a posteriori, directly from the analysis results. This represents a significant advancement over commercial software, which typically requires slip surfaces as input and then applies search algorithms to determine the critical Factor of Safety (FoS) . For example, Slide2 [22], GEOSTRU Slope Software [23], SLOPE/W [24] and Oasys Slope [25] all rely on a predefined set of slip surfaces, extracting the critical failure surface through an optimization process. On the other hand, software such as Plaxis 2D [26] and FLAC [27] do not require an input sliding surface but also do not directly provide the slip surface as output, requiring additional post-processing to extract it from the results. This makes the proposed approach original, as it offers a consistent framework where the slip surface is not an imposed assumption but an emerging result of the analysis itself, reducing bias and providing a more adaptive and objective stability assessment.

Additionally, where feasible, stability assessments are cross-validated using both the SOCP-FEM and MLD methods to rigorously evaluate the consistency and reliability of the results. Through this multifaceted approach, the study aims to establish a new benchmark in slope stability assessment, balancing methodological rigor with practical applicability across diverse contexts.

To illustrate the applicability and effectiveness of this strategy, the thesis examines case studies from diverse geological settings, spanning both submarine and subaerial environments, including:

- Offshore Seabed Stability for the Piombino Regasification Vessel Relocation: this study addresses the geotechnical challenges associated with seabed stability in offshore Vado Ligure, a site of strategic socioeconomic importance. In addition to gravitational loading, it considers water and seismic loads, providing a comprehensive assessment of stability in seismic-prone environments.
- Tavernola Landslide (Lake Iseo): this case study examines the Tavernola landslide near Lake Iseo, emphasizing its critical role in risk mitigation within a multi-hazard framework. Given the potential for a landslide-induced wave, the study integrates slope stability analysis, landslide dynamics, and wave propagation modeling, serving as a Proof of Concept (POC) for a comprehensive approach that can be adapted to other environments.
- Salse del Dragone Mud Volcano: this case study examines a complex geomorphological system that has not previously been analyzed from a stability perspective. The study focuses on an area with limited available data and, while it may appear to have low direct risk significance due to the absence of nearby infrastructure, it holds substantial scientific value. Characterizing the stability of this unique environment contributes to a deeper understanding of geomorphological processes in complex mud volcano systems, offering insights that may inform stability assessments in similarly data-scarce and challenging environments.

By systematically addressing limitations in existing methods and introducing a novel, multi-faceted stability assessment framework, this thesis makes a significant contribution to the field of geotechnical analysis. The proposed approach is designed to bridge the gap between theoretical rigor and practical applicability, ensuring that slope stability assessments are more reliable, adaptable, and informative for decision-making in complex and uncertain environments.

1.1 Stability analysis: an overview

In slope stability analysis, the most frequent quantity object of investigation is the FoS. This is typically defined as the ratio between the forces opposing to the destabilization and the forces driving movement. If the FoS is greater than one, the slope is considered stable; if it is less than one, the slope is considered unstable.
The most popular approach to compute the Factor of Safety of a slope has been for many years the Limit Equilibrium Method (LEM) [28], introduced in the early 20th century and developed thereafter until now [29]. More recently, alternative methods have been developed, such as the Limit Analysis (LA), several of which adopt a finite element approach.

Starting with Fellenius's early work [30], Limit Equilibrium Methods were expanded in the 1950s and 1960s by researchers like Bishop [31], Morgenstern and Price [32], Spencer [33], and Janbu [34].
The general concept behind this method is relatively straightforward: a soil mass is divided into a finite number of slices (or blocks), and the equilibrium of forces (and, in some formulations, of moments too) is assessed. Based on this analysis, and adopting a failure criterion that in almost all approaches coincides with the Mohr-Coulomb one, a Factor of Safety is calculated, determining the overall stability or instability of the slope. However, the theoretical challenge with this method lies in the fact that it involves more unknowns than equations, requiring assumptions to be made about the unknowns to achieve a feasible solution.
The different LEM formulations are related to different assumptions. In particular, Fellenius method considers the interslice forces equal to zero and does not account for the moment equilibrium.
As regards the Bishop method, the interslice forces are not null and it takes into account the equilibrium of moments. There are two different versions of this latter method: in the simplified case, the horizontal inter-slice forces are considered null, while in the generalized one a dependency between the horizontal and vertical components of the interslice forces is imposed.
The method of Janbu in its simplified and general formulation is similar to Bishop's, but the main difference is in the slip surface used: in Bishop case the slip surface must be circular, while the Janbu method can be used for any

slip surface.
The Spencer and Morgenstern-Price methods both satisfy force and moment equilibrium, and both can handle circular and non-circular slip surfaces. The key difference lies in how they treat interslice forces: Spencer assumes a constant ratio between interslice forces, while Morgenstern-Price allows this ratio to vary according to an interslice force function.
Among the major limitations of LEM, the two most remarkable ones are that 1) at least in the conventional analysis, the stress–strain relationship is absent, meaning that a fundamental piece of physics is missing, and 2) the failure surface must be assumed a priori. Another limitation of the method is that it may not give a unique Factor of Safety, making it not suitable as a reference for accuracy, if compared to alternative methods. On the other hand, one the main advantages of the LEM is its relatively straightforward implementation in computer codes and in the low computational resources required. In the next chapter we will see how the MLD method [35], [5] the alternative formulation of the limit equilibrium method used in this work, overcomes this issue.

As regards Limit Analysis (LA), it was developed around '50s by Drucker and Prager [36], [37]. LA is based on the lower- and upper-bound theorems of plasticity theory: they are used to bound the solution of a stability problem (in terms of FoS) from below and above [38]. This method models a slope assuming soil as a perfectly plastic rigid structure obeying an associated flow rule. While LA is a robust tool for estimating the FoS, its assumptions and simplifications—such as perfect plasticity, pre-defined failure mechanisms —can limit its applicability to more complex or real-world scenarios.

With the advancement of technology and numerical modeling techniques, alternative methods for studying slope stability have emerged. Most of them rely on the Finite Element Method (FEM), one of the advantages of which is that the FoS arises naturally, without the need to assume a specific failure mechanism (as required in limit equilibrium methods) [39]. In finite element analysis the slope is discretized in triangular elements, forming a mesh. Tipically, one of the following four stress-strain relationships is used: linear elastic, multi-linear elastic, hyperbolic, and elasto-plastic.
FEM is often combined with advanced techniques such as the Strength Reduction Method (SRM) or the Gravity Increase Method (GIM). In the SRM,

developed by Matsui and San [40], the strength parameters of the slope are decreased until slope becomes unstable and equilibrium solutions no longer exist. A series of trial FoS are applied to adjust the soil's strength parameters (specifically cohesion and friction angle): then, the adjusted soil's parameters are re-input in the model for equilibrium analysis and Factor of Safety is determined when the slope is no longer stable. Details of this approach will be discussed in Section 2.1.
The Gravity Increase Method (GIM) [41] follows a similar approach, incrementally increasing the gravitational force on a slope until it fails, and the FoS is then derived from the critical gravitational load at failure.

1.2 Thesis Outline

In Chapter 2 the two stability methods used in this thesis are thoroughly examined. Section 2.1 focuses on the SOCP-FEM method, developed by Wang et al. [3], [42] as part of Wang's doctoral research at the University of Bologna. First, the governing equations are presented, followed by a discussion on how to reformulate them into a variational formulation using the multi-field Hellinger-Reissner variational principle [43]. The process of discretizing the problem with finite elements is then explained, along with how to adapt it for use with MOSEK [4], a software package for solving large-scale mathematical optimization problems. Finally, the algorithm for determining the Factor of Safety, which involves the SRM, is described in detail.
Section 2.2 covers the second method explored in this work, the MLD method, variant of the Limit Equilibrium Method (LEM) [35], [5]. As with the first method, we present the governing equations, their discretization, and the minimum lithostatic deviation principle, which forms the basis of the method.

Chapter 3 focuses on applying the two methods to a synthetic slope and introduces a new technique developed to extract the sliding surface. First, the convergence of the SOCP-FEM solution for different mesh sizes is evaluated. Then, we present our sliding surface extraction strategy, which involves the computation of a new quantity, S, and the use of cubic spline interpolation. Section 3.2 outlines the validation process: the extracted surfaces from the combined SOCP-FEM and our proposed strategy will be used as input for the

MLD method. The resulting Factor of Safety will then be compared with the results from Cheng et al. [11]. Additionally, we will compare our results with sliding surfaces extracted using Cheng's method [44].

Chapter 4 illustrates the application of the MLD method to a real case study, the Vado Ligure pipeline. We explore the capabilities of the MLD software by conducting a stability analysis in a submarine environment under different seismic loads. Additionally, a sensitivity analysis is presented, varying the friction angle.

Chapter 5 presents the application of the SOCP-FEM method to a real case study, the Tavernola landslide, located along the slopes of Monte Saresano, bordering the Lake Iseo (northern Italy). In this chapter, we apply the new strategy developed to extract the sliding surface and compare our results with a sliding surface derived from detailed geotechnical investigations [8]. Furthermore, we propose a Proof of Concept (POC) to link the stability analysis with the landslide dynamics and possible landslide-generated wave in the lake. The output of our stability analysis will serve as the input for the dynamic simulation, thus developing a robust and reusable routine capable of analyzing the entire landslide event.

Lastly, Chapter 6 focuses on the study of the Salse del Dragone mud volcano, located in Emilia-Romagna, Italy. This is the most comprehensive study in this work, as it investigates a site that has not been extensively studied before. First, we describe the field surveys conducted to characterize the area. In Section 6.2.1, we present the Structure from Motion (SfM) photogrammetry analysis, outlining its key concepts and results. This analysis revealed significant variations in elevation and slope morphology, which was useful for the next steps.
Section 6.2.2 details the seismic characterization of the soil, carried out using both active and passive techniques. This analysis identified an interface at a depth of 10 meters, which may suggest the presence of a sliding body.
Finally, Section 6.3 addresses the stability of the site. We performed a stability analysis using both the MLD and SOCP-FEM methods, determining the overall stability of the slope.

The final chapter contains the main conclusions deducible from this work.

Chapter 2

SOCP-FEM and MLD methods

In this chapter, a detailed description of the two main algorithms used in the present study is provided. Specifically, the SOCP-FEM will be discussed in Section 2.1, focusing on its governing equations, the variational formulation and the numerical implementation.
Similarly, Section 2.2 will deal with the MLD method, providing an in-depth explanation of its underlying principles and of the development of its equations.

2.1 SOCP-FEM

In geotechnical engineering, slope stability analysis plays a vital role in assessing the safety and performance of slopes and earth structures. The use of the Finite Element Method (FEM) has become increasingly prevalent in this field due to its flexibility in handling complex geometries, and in allowing a detailed representation of the physical processes involved in slope failure, such as deformation and stress distribution.
Within this context, the Second-Order Cone Programming - Finite Element Method (SOCP-FEM) was developed by Wang et al. [42], [3] as part of a doctoral research project in geophysics at the University of Bologna. This thesis extends Wang's work, with specific advancements in the layering approach discussed in Section 6.3.2 and in the identification of the sliding surface, as illustrated in Chapter 3. These developments aim to further refine the method's accuracy and applicability in complex geotechnical contexts.
To illustrate the main methodological aspects of the approach, the following

sections will examine the fundamental equations of SOCP-FEM and outline its implementation. The key steps are as follows:

1. First, we will introduce the governing equations of the 2D problem;
2. Next, we will explain how these equations can be reformulated into a variational form using the multi-field Hellinger-Reissner variational principle [43];
3. We will then illustrate the discretization process using the finite element method;
4. We will describe how to transform the resulting discretized problem into a form suitable for Second Order Cone Programming;
5. Finally, we will explain the search algorithm used to determine the Factor of Safety for the slope.

2.1.1 Governing Equations

In this section the governing equations are summarized. In particular we are addressing 2D partial differential equations of rate-independent elasto-plastic plane-strain problems for a continuum medium. Beginning with the strain-displacement relationship, we will introduce the equilibrium equation, boundary conditions, and the constitutive relationship.

Strain-Displacement relationship

Assuming infinitesimal deformations, the infinitesimal strain tensor, ϵ, is defined as the symmetric part of the displacement gradient, representing how the displacement field u varies throughout the domain. In a two-dimensional plane-strain condition, the components of ϵ are given as $(\epsilon_{xx}, \epsilon_{yy}, 2\epsilon_{xy})$, which are denoted as $(\epsilon_x, \epsilon_y, 2\epsilon_{xy})$. The ϵ_{ij} elements can be written as follows:

$$\epsilon_{ij} = \frac{1}{2}\left(\frac{\partial u_i}{\partial x_j} + \frac{\partial u_j}{\partial x_i}\right) \tag{2.1}$$

where $\boldsymbol{x} = (x, y)$ is the position vector and $\mathbf{u} = (u_x, u_y)^T$ the displacement vector.

The strain-displacement relationship can be written as:

$$\boldsymbol{\epsilon} = \boldsymbol{\nabla} \boldsymbol{u} \tag{2.2}$$

or, in matrix form:

$$\boldsymbol{\epsilon} = \begin{bmatrix} \epsilon_x \\ \epsilon_y \\ 2\epsilon_{xy} \end{bmatrix} = \begin{bmatrix} \partial_x u_x \\ \partial_y u_y \\ \partial_y u_x + \partial_x u_y \end{bmatrix} \tag{2.3}$$

where the 2D gradient is $\boldsymbol{\nabla} = \left(\frac{\partial}{\partial x}, 0, \frac{\partial}{\partial y}; 0, \frac{\partial}{\partial y}, \frac{\partial}{\partial x}\right)^T \equiv (\partial_x, 0, \partial_y; 0, \partial_y, \partial_x)^T$.

Equilibrium Equation

The classical 2D static equilibrium equation is:

$$\boldsymbol{\nabla^T \sigma} + \mathbf{b} = 0 \quad \text{in } \Omega \tag{2.4}$$

where $\mathbf{b} = (b_x, b_y)^T$ is the body force, $\boldsymbol{\sigma} = (\sigma_x, \sigma_y, \sigma_{xy})^T$ is the stress vector and Ω a 2D domain with boundary $\partial\Omega$.

Boundary Conditions

The boundary conditions are relative to prescribed displacements and tractions. In particular:

$$\mathbf{u} = \mathbf{u}^P \quad \text{on } \Omega \tag{2.5}$$

$$\mathbf{N}\boldsymbol{\sigma} = \mathbf{t} \quad \text{on } \partial\Omega \tag{2.6}$$

with $\boldsymbol{u^P}$ the prescribed displacements, $\boldsymbol{t}$ the traction and $\mathbf{N} = (n_x, 0, n_y, 0, n_z, 0)^T$ with n_x and n_y being the cosine directions of the outward unit normal vector on the traction surface.

Constitutive Relationship

In the thesis we will adopt the Mohr-Coulomb criterion, which assumes an elasto-plastic constitutive relationship. The constitutive relationship is given by:

$$F(\boldsymbol{\sigma}) \leq 0 \tag{2.4a}$$

and

$$\boldsymbol{\epsilon} = \boldsymbol{\epsilon}^e + \boldsymbol{\epsilon}^p, \quad \boldsymbol{\epsilon}^e = \mathbb{C}\boldsymbol{\sigma}, \quad \boldsymbol{\epsilon}^p = \lambda \nabla_\sigma G, \quad G = G(\boldsymbol{\sigma}) \tag{2.4b}$$

where F is the yield function, $\boldsymbol{\epsilon}^e$ and $\boldsymbol{\epsilon}^p$ are the elastic and plastic strains, respectively, $\mathbb{C}$ is the elastic compliance matrix, λ is the plastic multiplier, and G is the plastic potential. As shown in Equation (2.4b), the strain is additively decomposed, and its incremental form is expressed as:

$$\Delta\boldsymbol{\epsilon} = \mathbb{C}\Delta\boldsymbol{\sigma} + \Delta\lambda \nabla_\sigma G(\boldsymbol{\sigma}) \tag{2.5}$$

For an associated flow rule, we have $G = F$. When the material undergoes purely elastic deformation, the plastic multiplier increment $\Delta\lambda = 0$ and $F(\boldsymbol{\sigma}) < 0$, whereas when the material yields, we have $\Delta\lambda > 0$ and $F(\boldsymbol{\sigma}) = 0$. This constraint is known as the complementary condition, expressed as:

$$\Delta\lambda F(\boldsymbol{\sigma}) = 0, \quad \Delta\lambda \geq 0 \tag{2.7}$$

This implies that the incremental form of the constitutive relationship is written as follows:

$$\begin{aligned} F(\boldsymbol{\sigma}) &\leq 0 \\ \Delta\boldsymbol{\varepsilon} &= \mathbb{C}\Delta\boldsymbol{\sigma} + \Delta\lambda \nabla_\sigma G(\boldsymbol{\sigma}) \\ \Delta\lambda F(\boldsymbol{\sigma}) &= 0, \quad \Delta\lambda \geq 0 \end{aligned} \tag{2.8}$$

2.1.2 Variational Formulation

The set of governing equations presented can be rearranged into a variational formulation. This means that all the equations will be unified into a single functional, subject to constraints, which will then be optimized by finding its

minimum or maximum.
The standard finite element analysis is derived from the principle of minimum potential energy or the principle of virtual work, where displacements or stresses serve as the primary field, while all other field variables are obtained from it. In contrast, the multi-field Hellinger-Reissner variational principle [43], which treats both displacements and stresses as primary fields, is used for static analysis. The corresponding functional is defined as:

$$\Pi(\boldsymbol{\sigma}, \mathbf{u}) = \int_{\Omega} \left(-\frac{1}{2} \Delta\boldsymbol{\sigma}^T \mathbb{C} \Delta\boldsymbol{\sigma} + \boldsymbol{\sigma}^T \nabla^T \mathbf{u} \right) d\Omega - \int_{\Omega} \mathbf{b}^T \mathbf{u} d\Omega - \int_{\partial\Omega} \mathbf{t}^T \mathbf{u} d(\partial\Omega) \tag{2.9}$$

The equivalence between this variational principle and the governing equations can be established by introducing an additional term s, as follows:

$$F(\boldsymbol{\sigma}_{n+1}) + s = 0, \quad s > 0 \tag{2.10}$$

This leads to the functional:

$$J = \Pi(\boldsymbol{\sigma}, \mathbf{u}) + \beta \ln s - \Delta\lambda (F(\boldsymbol{\sigma}_{n+1}) + s) \tag{2.11}$$

where β is a small constant, and the logarithmic barrier function ensures $s > 0$. By taking the functional derivatives, we derive the governing equations for static analysis:

$$\frac{\delta J}{\delta \Delta\mathbf{u}} = \begin{cases} \nabla^T \boldsymbol{\sigma} + \mathbf{b} = 0, & \text{in } \Omega \\ \mathbf{N}\boldsymbol{\sigma} = \mathbf{t}, & \text{on } \partial\Omega \end{cases} \tag{2.12}$$

$$\frac{\delta J}{\delta \boldsymbol{\sigma}} = \nabla(\Delta\mathbf{u}) - \mathbb{C}\Delta\boldsymbol{\sigma} - \Delta\lambda \Delta F(\boldsymbol{\sigma}) = 0 \tag{2.13}$$

$$\frac{\delta J}{\delta \Delta\lambda} = F(\boldsymbol{\sigma}) + s = 0 \tag{2.14}$$

$$\frac{\delta J}{\delta s} = \frac{\beta}{s} - \Delta\lambda = 0 \quad \longrightarrow \quad s\Delta\lambda = \beta \tag{2.15}$$

These equations correspond to the governing static analysis equations when β approaches 0. The flow rule $F = G$ is included in Equation 2.13, allowing the solutions to be obtained at the saddle point of the functional $\partial\Pi(\sigma, u) = 0$. Thus, the problem is transformed into a min-max optimization problem:

$$\min_{\mathbf{u}} \max_{\boldsymbol{\sigma}} \int_{\Omega} \left(-\frac{1}{2} \Delta\boldsymbol{\sigma}^T \mathbb{C} \Delta\boldsymbol{\sigma} + \boldsymbol{\sigma}^T \nabla^T \mathbf{u} \right) d\Omega - \int_{\Omega} \mathbf{b}^T \mathbf{u} d\Omega - \int_{\partial\Omega} \mathbf{t}^T \mathbf{u} d(\partial\Omega) \tag{2.16}$$

where internal work is maximized with respect to stresses, and total potential energy is minimized with respect to displacements. The incremental form of the min-max problem is:

$$\begin{aligned} \min_{\Delta\mathbf{u}} \max_{\boldsymbol{\sigma}_{n+1}} \Bigg(& -\frac{1}{2} \int_{\Omega} \Delta\boldsymbol{\sigma}^T \mathbb{C} \Delta\boldsymbol{\sigma} d\Omega + \int_{\Omega} \boldsymbol{\sigma}^T \nabla^T \Delta\mathbf{u} d\Omega \\ & - \int_{\Omega} \mathbf{b}^T \Delta\mathbf{u} d\Omega - \int_{\partial\Omega} \mathbf{t}^T \Delta\mathbf{u} d(\partial\Omega) \Bigg) \end{aligned} \tag{2.17}$$

subject to the constraint $F(\sigma) \leq 0$. The stress increment is $\Delta\sigma = \sigma_{n+1} - \sigma_n$ and Δu is the displacement increment.

2.1.3 FEM Discretization

We now proceed to the discretization of the problem using the Finite Element Method (FEM), which allows for the numerical approximation of the governing equations over a discrete domain. In this process, the initial body is divided into triangular elements, as shown in Figure 2.1. In order to do so, we use isoparametric elements, a type of finite element where the same shape functions are used to interpolate both the geometry (coordinates of the element) and the field variables (such as displacements) within the element.

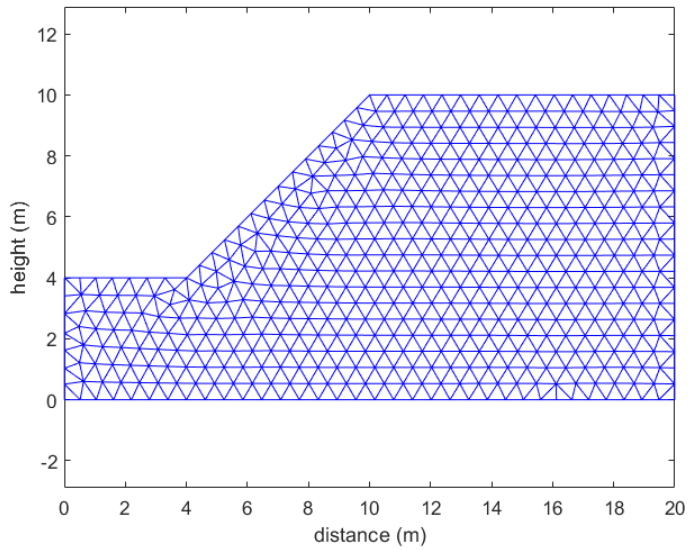

Figure 2.1. Example of a slope discretized using finite elements.

Using the standard finite element notation, we can write:

$$\boldsymbol{\sigma} \simeq \boldsymbol{N}_{\boldsymbol{\sigma}} \hat{\boldsymbol{\sigma}} \tag{2.18}$$

$$\mathbf{u} \simeq \boldsymbol{N}_{\boldsymbol{u}} \hat{\mathbf{u}} \tag{2.19}$$

where $\hat{\sigma}$ and $\hat{u}$ are the values assumed by the variables at the interpolation nodes, and $\mathbf{N}_\sigma$ and $\mathbf{N_u}$ are the matrices containing the interpolation shape functions for stress and displacement. This implementation relies on mixed isotropic triangular element (Figure 2.2): quadratic shape function for the displacement field and linear shape function for the stress field are considered. Therefore, we can write the shape functions in their natural coordinates (r,s,t=1-r-s), as follows:

$$\begin{aligned} &N_u^1 = (2t-1)t, \quad N_u^2 = (2r-1)r, \quad N_u^3 = (2s-1)s, \quad N_u^4 = 4rt, \\ &N_u^5 = 4rs, \quad N_u^6 = 4st, \\ &N_\sigma^1 = \left(2t - \frac{1}{3}\right), \quad N_\sigma^2 = \left(2r - \frac{1}{3}\right), \quad N_\sigma^3 = \left(2s - \frac{1}{3}\right) \end{aligned} \tag{2.20}$$

Using Equation 2.19 in Equation 2.2 we can write the strain-displacement

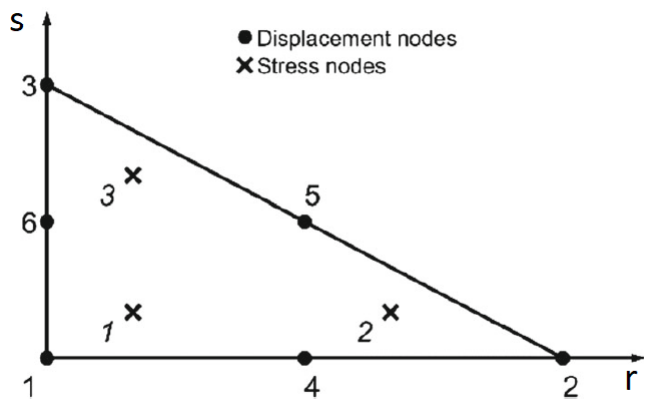

Figure 2.2. Example of mixed isotropic triangular element in the natural coordinate plane rs. Dots are displacement interpolation nodes, crosses the stress nodes. Adapted after [3].

relationship in its discretized form:

$$\epsilon = \nabla \mathbf{u} \simeq \nabla(N_u \hat{\mathbf{u}}) = (\nabla N_u)\hat{\mathbf{u}} = \mathbf{B}_u \hat{\mathbf{u}} \tag{2.21}$$

By combining Equation 2.18, 2.19 and 2.21 into Equation 2.17 we can obtain the discretized version of the variational formulation:

$$\begin{aligned} \min_{\Delta \mathbf{u}} \max_{\hat{\boldsymbol{\sigma}}_{n+1}} \quad & \hat{\boldsymbol{\sigma}}_{n+1}^T \mathbf{B} \Delta \hat{\mathbf{u}} - \mathbf{f}^T \Delta \hat{\mathbf{u}} - \frac{1}{2} \Delta \hat{\boldsymbol{\sigma}}^T \mathbf{C} \Delta \hat{\boldsymbol{\sigma}}^T \\ \text{subject to:} \quad & F(\hat{\boldsymbol{\sigma}}_{n+1}^j) \leq 0, \quad j = 1, \ldots, n_\sigma \end{aligned} \tag{2.22}$$

where the yield function F is imposed at each stress interpolation point, n_σ denotes the total number of stress interpolation points, n+1 indicates the step at which the variable is evaluated, and:

$$\mathbf{B} = \int_\Omega N_\sigma^T \mathbf{B}_u d\Omega \tag{2.23}$$

$$\mathbf{f} = \int_\Omega N_u^T d\Omega + \int_{\partial\Omega} N_u^T t d(\partial\Omega) \tag{2.24}$$

$$\mathbf{C} = \int_\Omega N_\sigma^T \mathbb{C} N_\sigma d\Omega \tag{2.25}$$

Since the minimization part of Equation 2.22 can be solved analytically, it can be incorporated into the constraints of the min-max problem, reducing it to a maximization problem as follows:

$$\begin{aligned} \max_{\hat{\boldsymbol{\sigma}}_{n+1}} \quad & -\frac{1}{2} \Delta \hat{\boldsymbol{\sigma}}^T \mathbf{C} \Delta \hat{\boldsymbol{\sigma}} \\ \text{subject to:} \quad & \mathbf{B}^T \hat{\boldsymbol{\sigma}}_{n+1} - \mathbf{f} = 0 \\ & F(\hat{\sigma}_{n+1}^j) \leq 0, \quad j = 1, \ldots, n_\sigma \end{aligned} \tag{2.26}$$

2.1.4 Numerical Implementation

The maximization problem described by Equation 2.26 can be now be tranformed into a Second Order Cone Programming optimization problem. The standard form of this kind of problems is the following:

$$\min_x c^T x \quad \text{subject to} \quad Ax = b, \quad x \in \mathcal{Q} \tag{2.27}$$

where A is a matrix, b and c are vectors, $\mathcal{Q}$ a convex cone and x is the vector containing the optimization variables.
Figure 2.3 provides a schematic representation of the cones used in this analysis, i.e. 3-dimensional quadratic cones and rotated quadratic cones. It is

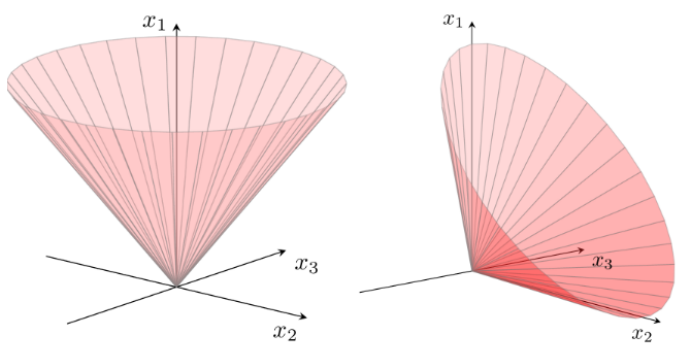

Figure 2.3. On the left is a schematic representation of the boundary of a quadratic cone, defined by the inequality $x_1 \geq \sqrt{x_2^2 + x_3^2}$. On the right is the boundary of a rotated quadratic cone, described by the equation $2x_1x_2 \geq x_3^2, x_1, x_2 \geq 0$. [4].

possible to demonstrate that the SOCP-FEM problem equivalent to Equation

2.26, is :

$$
\begin{aligned}
\min_{x_{n+1}} \quad & m \\
\text{subject to:} \quad & \mathbf{B}^T \hat{\boldsymbol{\sigma}}_{n+1} + \mathbf{E}_u^T \hat{\mathbf{r}} = \mathbf{f}, \\
& -\mathbf{H}\hat{\boldsymbol{\sigma}}_{n+1} + \boldsymbol{\chi}^j = \mathbf{d}, \quad j = 1, \dots, n_\sigma, \\
& -\hat{\boldsymbol{\sigma}}_{n+1}\mathbf{C}^{1/2} + y = 0, \\
& n = 1, \\
& (m, n, y) \in \mathcal{Q}_r^3, \\
& \boldsymbol{\chi}^j = (\chi_1^j, \chi_2^j, \chi_3^j) \in \mathcal{Q}^3, \quad j = 1, \dots, n_\sigma,
\end{aligned}
\tag{2.28}
$$

$$
\text{with:} \quad \mathbf{H} = \begin{bmatrix} -\sin\phi & -\sin\phi & 0 \\ 1 & -1 & 0 \\ 0 & 0 & 2 \end{bmatrix}, \quad \mathbf{d} = \begin{bmatrix} 2c\cos\phi \\ 0 \\ 0 \end{bmatrix}
$$

$$
\begin{aligned}
(\chi_1, \chi_2, \chi_3) \in \mathcal{Q}^3 &= \{(\chi_1, \chi_2, \chi_3) \in \mathbb{R}^3 \mid \chi_1 > \sqrt{\chi_2^2 + \chi_3^2}\}, \\
(m, n, y) \in \mathcal{Q}_r^3 &= \{(m, n, y) \in \mathbb{R}^3 \mid 2mn > y^2; \quad m, n \geq 0\}, \\
\mathbf{x} &= \{\hat{\boldsymbol{\sigma}}_{n+1}, \boldsymbol{\chi}, \mathbf{y}, m, n, \mathbf{r}, \mathbf{0}\}.
\end{aligned}
$$

The SOCP problem in Equation 2.28 reformulates the quadratic term $\frac{1}{2}\Delta\hat{\sigma}^T\mathbf{C}\Delta\hat{\sigma}$ as the minimization of the scalar m, subject to equality constraints involving y and $n = 1$, and a rotated quadratic constraint $(m, n, y) \in \mathcal{Q}_r^3$. Similarly, the yield criterion $F(\hat{\sigma}_{n+1}^j)$ is transformed into linear and conic constraints involving auxiliary variables χ^j, ensuring conic feasibility. The matrix $\mathbf{E}_u^T$ is a is a matrix of indices that allows assessing the prescribed displacement and $\hat{\mathbf{r}}$ is a new variable, i.e. the nodal reaction force: both quantities derive from the numerical implementation of the boundary conditions. For the details of this computation see Wang et al. [42].
It is then possible to write our problem in the form of Equation 2.27, as follows:

$$
\mathbf{c} = \Big[\mathbf{0}; \mathbf{0}; \mathbf{0}; 1; 0\Big] \tag{2.29}
$$

$$\mathbf{A} = \begin{bmatrix} \mathbf{B}^T & \mathbf{0} & \mathbf{0} & 0 & 0 & 0 \\ -H & \text{diag}(1) & \mathbf{0} & 0 & 0 & 0 \\ -\mathbf{C}^{1/2} & \mathbf{0} & \text{diag}(1) & 0 & 0 & 0 \\ \mathbf{0} & \mathbf{0} & \mathbf{0} & 0 & 0 & 1 \end{bmatrix} \tag{2.30}$$

$$\mathbf{b} = \Big[\mathbf{f}, \mathbf{d}, 0, 1\Big] \tag{2.31}$$

$$\text{blx} = b, \quad \text{bux} = b \tag{2.32}$$

where blx and bux are the lower and upper limits of Ax. The resulting problem can now be solved using MOSEK [4], a software package designed for solving large-scale mathematical optimization problems. In particular, the main steps of the algorithm are:

1. Update the optimization variables based on the previous state or initial condition;
2. Assemble the global matrices $\mathbf{B}$, $\mathbf{C}$,$\mathbf{f}$, $\mathbf{H}$, and $\mathbf{d}$;
3. Formulate the SOCP problem by defining the vectors $\mathbf{b}$, $\mathbf{c}$ and the matrix $\mathbf{A}$ as in Equation 2.30, 2.31;
4. Solve the SOCP problem using MOSEK with the quantities defined in step 3;
5. Extract the following results from the solution:
   - The stress $\hat{\sigma}_{n+1}$;
   - The nodal displacements $\Delta\mathbf{u}$;
   - The strain tensor $\boldsymbol{\epsilon}$;
   - The strain tensor increment $\Delta\boldsymbol{\epsilon}$;
6. Return to step 1, updating the incremental step index $i = i + 1$.

2.1.5 Factor of Safety search algorithm

Among the various methods used to retrieve the FoS, the SOCP-FEM approach employs the SRM. In this method the soil properties — specifically cohesion (c) and internal friction angle (ϕ) — are gradually reduced with each iteration, weakening the soil's strength. The reduction factor (RF) is defined as follows:

$$\mathrm{RF} = \frac{c}{c'} \tag{2.33}$$

$$\mathrm{RF} = \frac{\tan\phi}{\tan\phi'} \tag{2.34}$$

where c' and ϕ' are the reduced cohesion and friction angle. The FoS is determined as the RF value at which the system reaches the stability-instability threshold, meaning that any further reduction in c' and ϕ' would cause instability. However, it is important to clarify that true instability—where the numerical solution does not converge—occurs only when FoS < 1. In this case, any additional reduction in geotechnical parameters would result in theoretically infinite displacements. Conversely, when FoS > 1, the computed displacements remain finite and consistent with the static equilibrium equations, indicating that the system remains stable.

The FoS search algorithm implemented in the SOCP-FEM software follows these steps:

1. An initial range $[RF_1, RF_2]$ is defined for the Reduction Factor (RF).
2. A bisection method is applied to iteratively search for the critical RF value.
3. The process continues until the interval width falls below a predefined tolerance (typically 10^{-3}, 10^{-4}). At this point, the algorithm converges, and the RF value at convergence is taken as the FoS.
4. The slope is unstable if:
    - The optimization solution becomes infeasible, or

- The maximum incremental displacement exceeds a defined threshold (typically 0.01 m to 10 m), which depends on the mesh domain and study objectives.

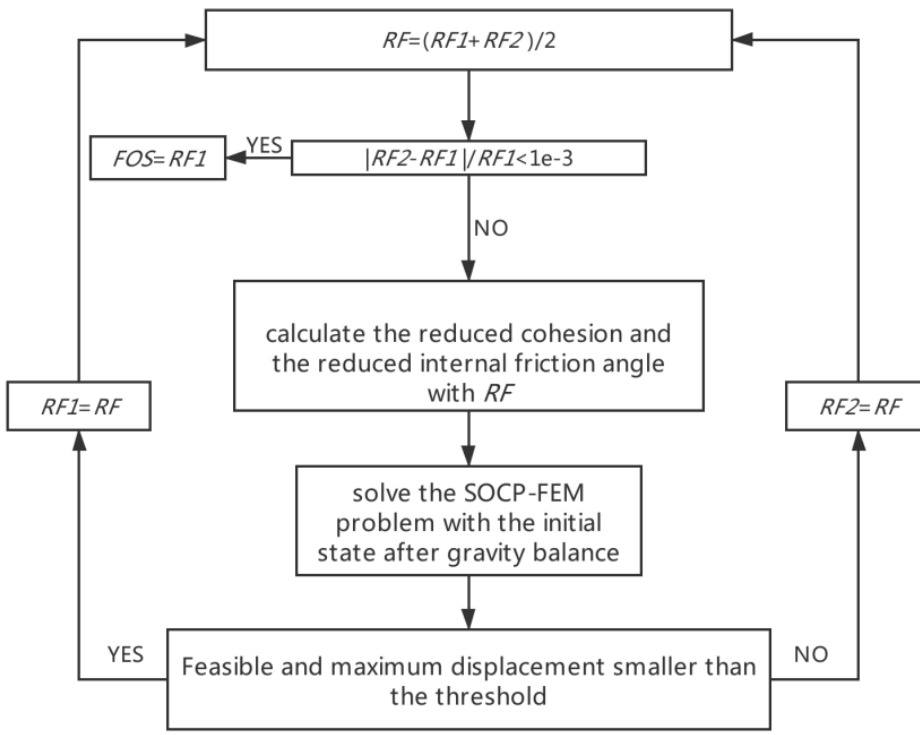

Figure 2.4. Search strategy for FoS [3].

2.2 MLD

The Minimum Lithostatic Deviation (MLD) method is a robust approach for slope stability analysis, developed by Tinti and Manucci [35], [5], and has been applied in several studies [45], [46], [47] to assess stability in different types of geomorphological environments (e.g., alpine regions, volcanic islands, etc.).
This method relies on the classic LEM, which considers the soil mass divided into finite slices or blocks and investigates the equilibrium of forces and moments. From this, the Factor of Safety is determined. However, the method faces a theoretical challenge: there are more unknowns than equations, needing assumptions to resolve the system and reach a solution. The MLD method aims to address this issue by introducing a new parameter called 'lithostatic deviation' and an associated principle.
In the next sections we are going to introduce the governing equations of the problem and their discretization, as well as the MLD principle.

2.2.1 Governing Equations

Figure 2.5 shows a schematic representation of a 2D body divided into slices. The body lies in the x-z plane and it is considered to be uniform along the horizontal axis y. The sliding body is bounded by the sliding surface $z_1(x)$ and the topographic profile $z_2(x)$. Each slice has an infinitesimal width Δx, a finite height $z_2(x) - z_1(x)$, and is comprised between $x - \frac{1}{2}\Delta x$ and $x + \frac{1}{2}\Delta x$. The governing equations can be derived by imposing the balance of forces and torques for each slice, which are functions of the horizontal coordinate x. In particular, we have:

- $w(x)$, the slice weight per unit area;
- $D(x)$, an external pressure acting on the topographic profile;
- $P(x)$, the pressure at the base of the slice;
- $S(x)$, the shear stress at the base of the slice;
- $E(x)$ and $X(x)$, the horizontal and vertical components of the inter-slice forces;
- $A(x)$, the component of the torque along the axis y.

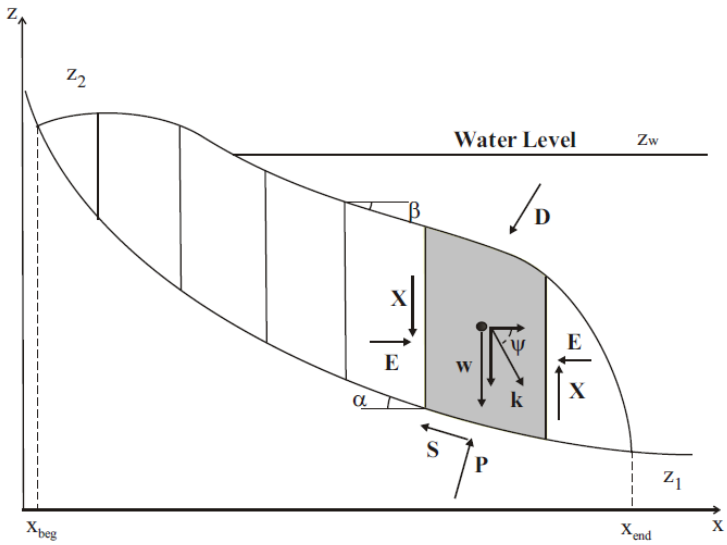

Figure 2.5. Sketch of the vertical cross-section of the sliding body cut into slices, after [5].

Therefore, the resulting set of governing equations is the following (see [35] for more details):

$$\frac{d}{dx}E + P\tan\alpha - S - D\tan\beta = -wk\cos\psi \tag{2.35}$$

$$\frac{d}{dx}X + P + S\tan\alpha - D = (1 + k\sin\psi)w \tag{2.36}$$

$$\frac{d}{dx}A - z_1\frac{d}{dx}E - X - D\tan\beta(z_2 - z_1) = -wk\cos\psi(z_B - z_1) \tag{2.37}$$

$$FoS \cdot S = \bar{c}^* + P\tan\bar{\phi}' \tag{2.38}$$

$$\text{with} \quad \bar{c}^* \equiv \bar{c}' - u\tan\bar{\phi}'$$

Equations 2.35 and 2.36 represent the balance of the horizontal and vertical components of the forces, while Equation 2.37 is the balance of the torque. $\alpha(x)$ and $\beta(x)$ are the slope angles at the base and at the top of the slice; $w(x)$ is the weight of the slice, defined as:

$$w(x) = g \int_{z_1}^{z_2} \rho(x, z)\, dz$$

where $\rho(x, z)$ is the density. In Equation 2.37 the torque is evaluated at the center of mass of the slide, $z_B(x)$, which is:

$$z_B(x) = \frac{\int_{z_1}^{z_2} \rho(x, z)\, z\, dz}{w(x)}$$

D(x) represent the load on the upper surface, i.e. the water load, expressed as:

$$D(x) = \rho_w g\, [z_w - z_2(x)] \quad \text{for } z_2(x) < z_w$$

$$D(x) = 0 \quad \text{for } z_2(x) \geq z_w$$

where z_w is the water level and ρ_w the water density. The seismic load is also considered in Equations 2.35, 2.36, 2.37: it is assumed to act at the centre of mass of the slice along the direction ψ and to be proportional to the slice weight through the coefficient k.
Equation 2.38 embodies the Limit Equilibrium Method: close to instability shear stress S and shear strength S_{max} tend to be equal on all the sliding surface. So, by means of Equation 2.38 it is imposed that shear strength and stress are proportional via the coefficient FoS, the safety factor, and that FoS may be used to mark the boundary between stable ($FoS > 1$) and unstable ($FoS < 1$) regions [5]. According to the Mohr-Coulomb law, S_{max} can be written as:

$$S_{\max}(x) = \bar{c}'(x) + [P(x) - u(x)] \tan \bar{\phi}'(x) \tag{2.39}$$

where $u(x)$ is the pore pressure, $\bar{c}'(x)$ and $\bar{\phi}'(x)$ are the averages of the soil cohesion and friction angle.
Lastly, the boundary conditions are required. In particular it is imposed that

all inter-slice forces and torques are zero at both the beginning and the end of the sliding body:

$$E(x_{\text{beg}}) = E(x_{\text{end}}) = 0 \tag{2.40}$$

$$X(x_{\text{beg}}) = X(x_{\text{end}}) = 0 \tag{2.41}$$

$$A(x_{\text{beg}}) = A(x_{\text{end}}) = 0 \tag{2.42}$$

The final set of governing equations is formed by three first-order ordinary differential equations (Equations 2.35, 2.36 and 2.37) completed by the corresponding boundary conditions and by an additional relationship 2.38. The five unknown functions are $S(x)$, $P(x)$, $E(x)$, $X(x)$ and $A(x)$ while the sliding surface $z_1(x)$ is assumed to be known a priori.

2.2.2 Discretization

Equation 2.38 can be used to express $S(x)$ in terms of $P(x)$ and to rearrange, after some manipulation, the system of governing equations as follows:

$$\begin{aligned} \frac{dE}{dx} + P\alpha_E &= \beta_E, \\ \frac{dX}{dx} + P\alpha_X &= \beta_X, \\ \frac{dA}{dx} + P\alpha_A - X &= \beta_A \end{aligned} \tag{2.43}$$

where the following parameters, all known functions of the problem, have been introduced:

$$\begin{aligned}
\alpha_E &= \tan\alpha - \frac{\tan\bar{\phi}'}{FoS} \\
\beta_E &= \frac{\bar{c}^*}{FoS} + D\tan\beta - k\cos\psi\, w \\
\alpha_X &= 1 + \frac{\tan\alpha\,\tan\bar{\phi}'}{FoS} \\
\beta_X &= D - \frac{\bar{c}^*}{FoS}\tan\alpha + (1 + k\sin\psi)\, w \\
\alpha_A &= z_1\alpha_E \\
\beta_A &= D\tan\beta\,(z_2 - z_1) - k\cos\psi\,(z_B - z_1)\, w + z_1\beta_E
\end{aligned} \tag{2.44}$$

The computational domain $[x_{\text{beg}}, x_{\text{end}}]$ is now divided into N equal intervals of length Δx, with nodal points x_i, $i \in [0, N]$. As a result, the body is partitioned into N vertical slices, and all variables are discretized accordingly. In particular, the pressure P and all the coefficients given by equation 2.44 are taken at the mid-points of the intervals, while the inter-slice forces $E(x)$, $X(x)$ and the torque $A(x)$ are taken at the nodal points.
Keeping this in mind, it is possible to demonstrate that the following equations correspond to the initial set of governing equations and related boundary conditions:

$$\mathbf{\Gamma e} + \mathbf{A_E p}\Delta x = \mathbf{b_E}\Delta x \tag{2.45}$$

$$\mathbf{\Gamma x} + \mathbf{A_X p}\Delta x = \mathbf{b_X}\Delta x \tag{2.46}$$

$$\mathbf{\Gamma a} + \mathbf{A_A p}\Delta x - \mathbf{\Omega X}\Delta x = \mathbf{b_A}\Delta x \tag{2.47}$$

$$\mathbf{X} - \mathbf{F_1 v} = \mathbf{F_2 q} \tag{2.48}$$

where $\mathbf{\Gamma}$ and $\mathbf{\Omega}$ are rectangular N×(N-1) matrices, in the form:

$$\mathbf{\Gamma} = \begin{pmatrix} 1 & 0 & 0 & 0 & 0 & 0 \\ -1 & 1 & 0 & 0 & 0 & 0 \\ 0 & -1 & 1 & 0 & 0 & 0 \\ \vdots & \vdots & \vdots & \vdots & \vdots & \vdots \\ 0 & 0 & 0 & -1 & 1 & 0 \\ 0 & 0 & 0 & 0 & -1 & 1 \end{pmatrix} \quad \mathbf{\Omega} = \frac{1}{2} \begin{pmatrix} 1 & 0 & 0 & 0 & 0 & 0 \\ 1 & 1 & 0 & 0 & 0 & 0 \\ 0 & 1 & 1 & 0 & 0 & 0 \\ \vdots & \vdots & \vdots & \vdots & \vdots & \vdots \\ 0 & 0 & 0 & 1 & 1 & 0 \\ 0 & 0 & 0 & 0 & 1 & 1 \end{pmatrix} \tag{2.49}$$

and p is defined as $p_i = p(x_i - \Delta x/2)$, for $i \in [1, N]$. Similarly, the vectors $\mathbf{b_E}$, $\mathbf{b_X}$, and $\mathbf{b_A}$ are: $b_{E,i} = \beta_E(x_i - \Delta x/2)$, $b_{X,i} = \beta_X(x_i - \Delta x/2)$, $b_{A,i} = \beta_A(x_i - \Delta x/2)$.
The coefficient α_E is discretized into a diagonal $N \times N$ matrix $\mathbf{A_E}$ with diagonal elements $(A_E)_{i,i} = \alpha_E(x_i - \Delta x/2)$. Analogous matrices $\mathbf{A_X}$ and $\mathbf{A_A}$ are defined in the same way.
For forces and torques, since these are zero at the boundaries, the attention is restricted to the internal nodes of the domain. Therefore, the unknown function $E(x)$ is transformed into the $(N-1)$ component vector $\mathbf{e}$, where $e_i = E(x_i)$, for $i \in [1, N-1]$. The same applies to the vectors $\mathbf{X}$ and $\mathbf{a}$, with $X_i = X(x_i)$ and $a_i = A(x_i)$.
For what concerns Equation 2.48, some additional considerations are required: putting together equations 2.45, 2.46 and 2.47 we obtain a system with 3N equations and (4N-1) unknowns, resulting in N-3 unknowns more than equations. In order to overcome this issue, some assumptions must be made. The strategy adopted in the MLD method is to expand the function of vertical forces, $X(x)$ over a basis of analytical known functions $f_k(x)$ (in particular, a Fourier series expansion), that is truncated to the first m terms. The expression is as follows:

$$X_i = f_{i1}v_1 + f_{i2}v_2 + \sum_{k=1}^{m-2} g_{ik}q_k \tag{2.50}$$

where q_k and g_{ik} are the known parameters and related functions while the two unknowns are v_1 and v_2. Equation 2.48 can be derived by introducing the appropriate 2-component vector v, (m-2) component vector q and the two matrices F_1 and F_2 (respectively of (N-1)×2 and (N-1)×(m-2) dimension).

Therefore, we can write the discretized system of equations as:

$$\begin{pmatrix} \boldsymbol{\Gamma} & 0 & 0 & \boldsymbol{A_E} & 0 \\ 0 & \boldsymbol{\Gamma} & 0 & \boldsymbol{A_X} & 0 \\ 0 & -\boldsymbol{\Omega}\Delta x & \boldsymbol{\Gamma} & \boldsymbol{A_A} & 0 \\ 0 & \boldsymbol{I} & 0 & 0 & -\boldsymbol{F}_1 \end{pmatrix} \begin{pmatrix} \boldsymbol{e} \\ \boldsymbol{X} \\ \boldsymbol{a} \\ \boldsymbol{p}\Delta x \\ \boldsymbol{v} \end{pmatrix} = \begin{pmatrix} \boldsymbol{b_E}\Delta x \\ \boldsymbol{b_X}\Delta x \\ \boldsymbol{b_A}\Delta x \\ \boldsymbol{F}_2\boldsymbol{q} \end{pmatrix} \tag{2.51}$$

which is a system of 4N-1 linear equations in 4N-1 unknowns and very suitable for inversion.

2.2.3 MLD Principle

All the traditional methods used in the limit-equilibrium approach consider the FoS as an unknown parameter, and make the attempt to overcome the non-uniqueness of the solution by making assumptions about the interslice forces. The innovative part of MLD method in respect to the other LEMs is the introduction of the Minimum Lithostatic Deviation in order to convert the limit-equilibrium method to a minimization problem, where the Safety factor FoS is a free parameter.
The Minimum Lithostatic Deviation is defined as:

$$\delta = W^{-1} \left[\frac{1}{(x_{\text{end}} - x_{\text{beg}})} \int_{x_{\text{beg}}}^{x_{\text{end}}} \left(E(x)^2 + X(x)^2 \right) dx \right]^{1/2} \tag{2.52}$$

where:

$$W = \frac{1}{x_{\text{end}} - x_{\text{beg}}} \int_{x_{\text{beg}}}^{x_{\text{end}}} w(x)\, dx \tag{2.53}$$

Here, δ represents the average magnitude of the inter-slice forces, normalized by the weight of the sliding mass. This parameter equals zero only if the functions $E(x)$ and $X(x)$ are zero everywhere, a condition that can be achieved solely by a homogeneous, uniform layer in lithostatic equilibrium on a constant slope. Therefore, δ quantifies the deviation from lithostatic equilibrium, allowing to identify the equilibrium state as the one that satisfies all equilib-

rium equations and corresponds to the smallest δ value.
Lastly, the value of the parameter FoS (Factor of Safety) that corresponds to the minimum δ is considered the final result of the limit-equilibrium analysis. In its current implementation, the MLD formulation does not yet include a systematic search for the most critical slip surface associated with the minimum FoS. Instead, in the applications presented in this thesis, we adopt a trial-based approach, where plausible slip surfaces are selected based on geological and geotechnical considerations. This means that multiple trials are performed using different predefined slip surfaces, which are chosen based on morphological, geophysical, and geological data.

It is worth noting that even commercial stability analysis software follows a similar approach: they do not perform a truly global search but rather evaluate a large number of potential slip surfaces and identify the one associated with the lowest FoS. The efficiency and accuracy of this process depend on the complexity of the algorithm used for surface generation and evaluation.

Chapter 3

Application: a Synthetic Case

In this chapter, the key problem of the identification of the critical failure surface for a given slope is addressed. The adopted strategy foresees the application of the two approaches described in Sections 2.1 and 2.2 to the synthetic cases proposed in Cheng et al. [11], who discussed the same problem by adopting the LEM an the SRM methods. The analysis begins with the application of the SOCP-FEM method, wherein the convergence of the solution is evaluated across various mesh resolutions.
Following this, a strategy is developed to extract the sliding surface from the obtained results. This subsequently serves as input for the MLD method, which is employed to validate the accuracy of the analysis.
Lastly, we will compare our results in terms of sliding surfaces with the one provided by Cheng et al. [11].

3.1 SOCP-FEM application

The synthetic case study involves a uniform soil slope with a height of 6 meters and a 45-degree angle. The overall dimensions of the profile are 10 meters in height and 20 meters in width, as illustrated in Figure 3.1.
The first step of our analysis focused on studying the convergence of the solution. We chose one of the cases examined in [11] and [3]. Specifically, the geotechnical parameters used are listed in Table 3.1.

We then proceeded to generate multiple meshes, starting from a coarse one and then refining it. In particular the values of the parameter h, defined as

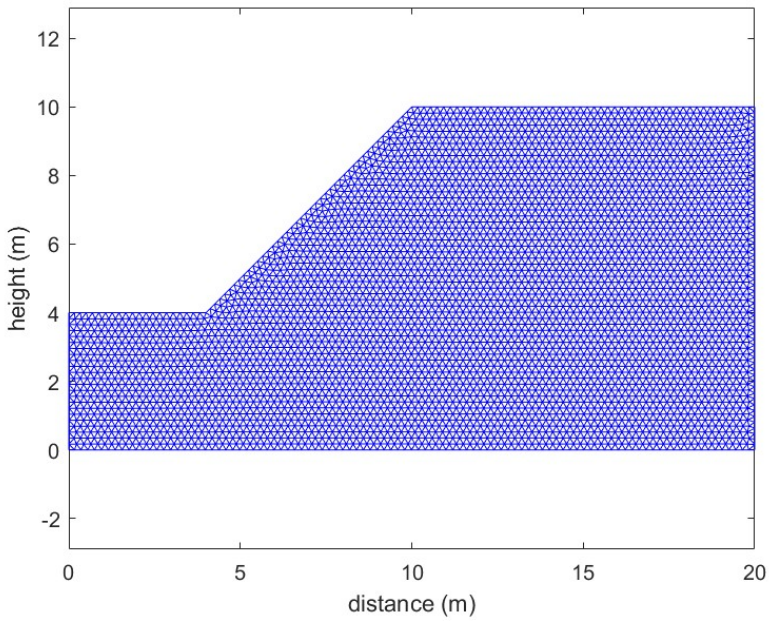

Figure 3.1. Example of mesh for the synthetic scenario.

Table 3.1. Geotechnical parameters of the Synthetic case.

Density (kN/m^3)	Cohesion (kPa)	Friction Angle (°)	Elastic Modulus (MPa)	Poisson Ratio
20	5	5	14	0.3

the diameter of the smallest of the circles that circumscribe each element of the grid, are listed in Table 3.2.

For each generated mesh, we performed a stability analysis and then assessed the convergence of the solution in terms of the Factor of Safety. The results are presented in Figure 3.2.

The FoS exhibits a clear trend, approaching a plateau around 0.42, with the difference between consecutive solutions decreasing to less than 0.40% from

Table 3.2. Mesh dimension from the coarsest to the finest.

Mesh ID	h	Number of Nodes	Number of Elements
h1	1.0	739	340
h2	0.8	1149	538
h3	0.6	2027	964
h4	0.4	4530	2191
h5	0.3	8101	3952
h6	0.2	18230	8967
h7	0.15	32174	15891
h8	0.10	73027	36218
h9	0.05	291554	145187

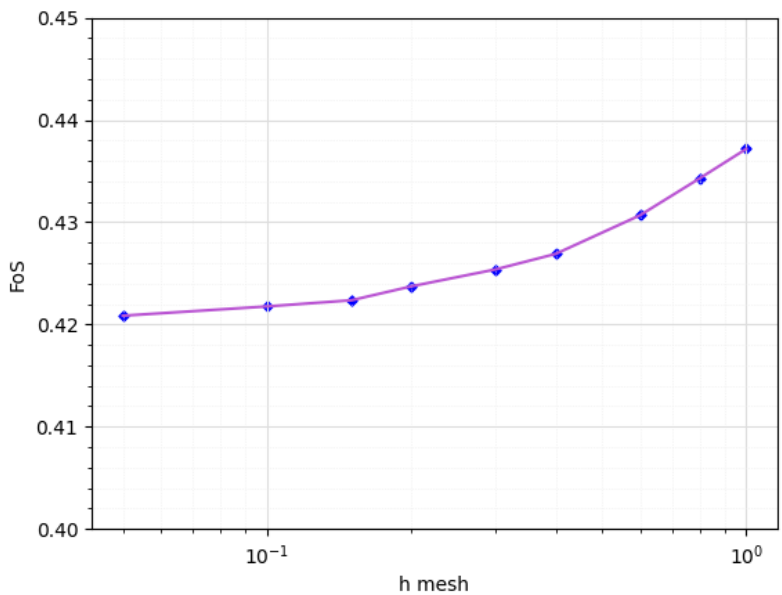

Figure 3.2. Convergence of the solution in terms of FoS.

mesh h4 to h9. This indicates a high level of convergence and stability in the results as we refine the mesh. These findings are consistent with values reported in the existing literature [11], [3]. In particular, they align well with the two different methods tested by Cheng et al. [11], which produce a Factor of Safety ranging between 0.41 and 0.43.

The methods referenced in their study include the Limit Equilibrium Method (LEM) and the Strength Reduction Method (SRM). The agreement between our results and those well-established methods highlights the accuracy and reliability of our approach, further validating our method in capturing the behavior of sliding surfaces and ensuring the stability analysis remains robust across different configurations. This comparison provides additional confidence that our model can effectively predict stability in various scenarios, aligning closely with recognized methodologies in geotechnical analysis. By examining how these surfaces influence the stability results within the MLD framework, we can determine the robustness and overall effectiveness of our approach.

3.1.1 Determination of the Sliding Surface

The SOCP-FEM method can provide us with several interesting physical quantities as output, which have been used to develop a strategy for extracting the sliding surface. In particular from our analysis we are able to retain, among the other, the following quantities:

- the displacement field;
- the three components of the strain tensor (ϵ_{xx}, ϵ_{yy}, ϵ_{xy});
- the three components of the stress tensor (σ_{xx}, σ_{yy}, σ_{xy}).

We focused primarily on two key quantities: the displacement field and the strain tensor, with the aim of reproducing the sliding surface.
This is clearly evident in the displacement data (see Figures 3.3 to 3.6 for selected meshes). Displacement reveals both the magnitude and direction of deformation under applied loads (in our case, gravitational forces only). Regions with significant displacement typically indicate zones of potential failure or instability. Moreover, large displacements are often associated with shear

failure, which directly contributes to the formation of the sliding surface. By analyzing the displacement vectors, we can identify both the direction of movement and the precise location of the failure plane.

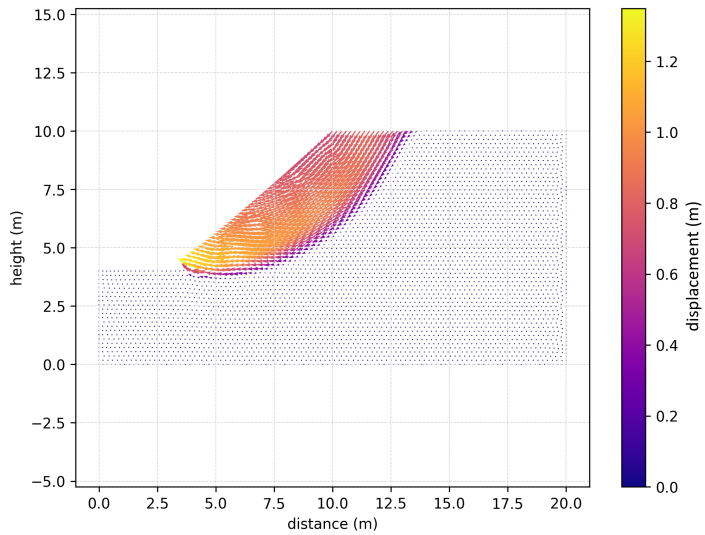

Figure 3.3. Displacement field for mesh h4.

However, for the purpose of identifying a thin, localized zone that represents the sliding surface, strain analysis is more suitable. Given the fundamental role that shear strain plays in landslide mechanics, influencing both slope stability and deformation behavior, we chose to focus on it. Strain allows for a more accurate detection of the failure band, highlighting areas where the material undergoes significant internal deformation, which is crucial for accurately defining the sliding surface.
Shear strain is essential in landslide mechanics because it directly influences the formation and propagation of shear zones or slip surfaces—areas where sliding primarily occurs. These shear zones are regions where strain is concentrated, leading to material weakening and, potentially, catastrophic failure if the shear stress surpasses the material's strength. Scientific literature emphasizes the importance of understanding shear strain in landslides:

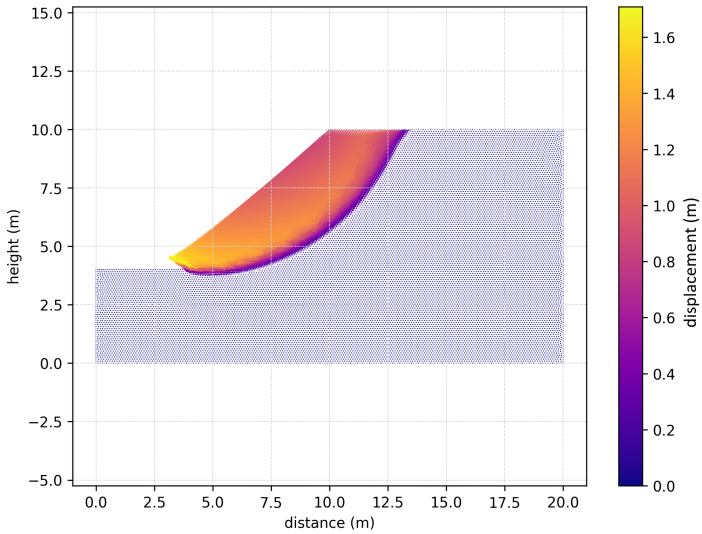

Figure 3.4. Displacement field for mesh h6.

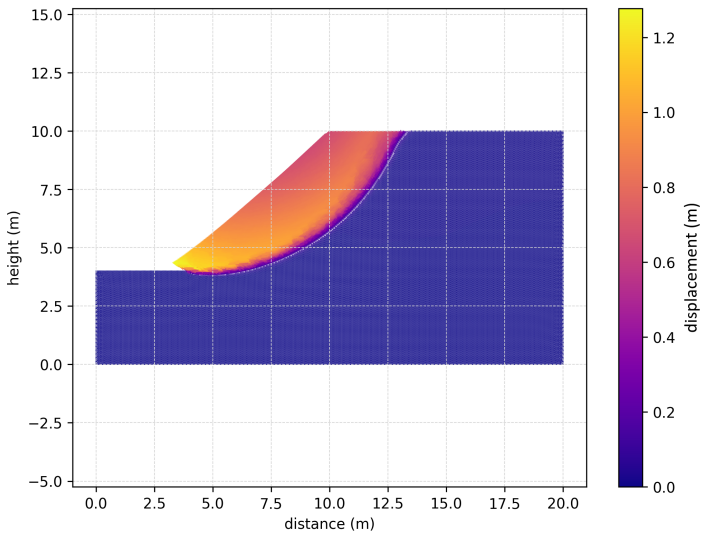

Figure 3.5. Displacement field for mesh h8.

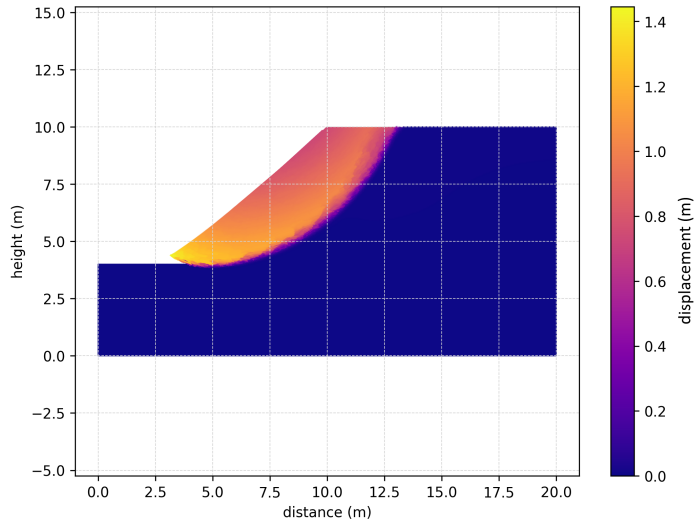

Figure 3.6. Displacement field for mesh h9.

- Shear resistance and strain softening: the shear resistance of materials within a landslide is essential for slope stability. Strain softening, where material strength diminishes with increasing strain, can lead to progressive failure. Monitoring shear strain is therefore vital in predicting these failure points and assessing slope behavior under stress [48].
- Residual shear strength: after the initial failure, the residual shear strength of the material dictates the ongoing movement of the landslide. Understanding residual shear strain behavior is crucial for evaluating the potential for reactivation in dormant or slow-moving landslides [49].

As the mesh is refined, the strain tensor reveals a distinct, sharply defined band in each of its components. Figures 3.7, 3.8, 3.9, and 3.10 illustrate the ϵ_{xy} component, i.e. the shear strain.

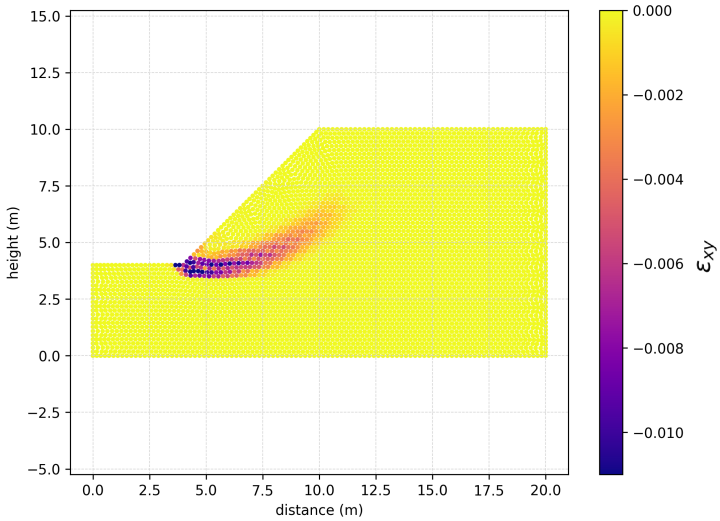

Figure 3.7. Shear strain for mesh h4.

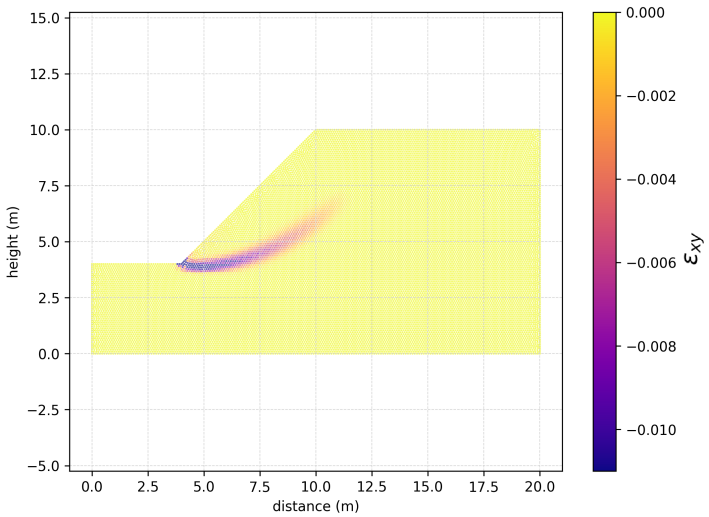

Figure 3.8. Shear strain for mesh h6.

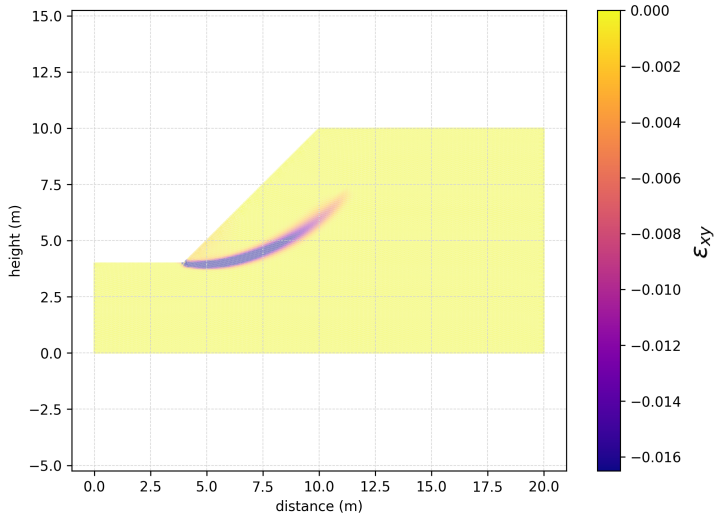

Figure 3.9. Shear strain for mesh h8.

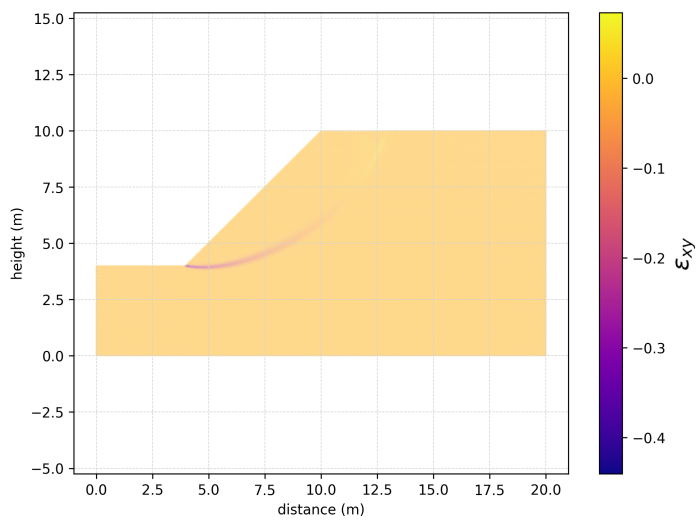

Figure 3.10. Shear strain for mesh h9.

One method, inspired by previous studies [50], involves computing a quantity that is always positive and easy to manage, based on the strain tensor. The equation is the following:

$$S = \sqrt{\epsilon_{ij}\epsilon_{ij}} \tag{3.1}$$

Through the computation of S, we identified a distinct and sharply defined band that marks the maximum values of this quantity (Figures 3.11 to 3.14). This band provided a clear indication of the areas most affected by strain, making it a crucial element in our analysis. The final step involved the definition of a straightforward strategy to extrapolate the sliding surface from this band, ensuring that the process was both direct and efficient. In order to do so, we decided to start with the most basic approach, divided into two steps:

- Selecting the region of the domain containing the highest values of S using a simple polygon (Figure 3.15);
- Interpolating the resulting data with a cubic spline, using the values of S as weights.

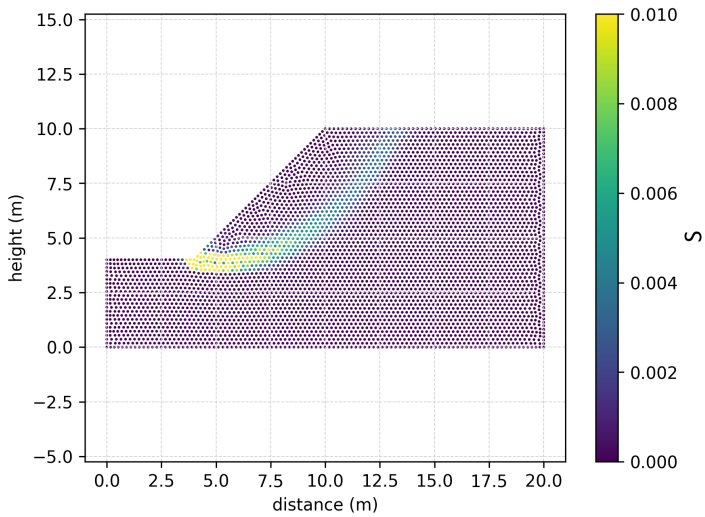

Figure 3.11. S for mesh h4. The nodes are color coded with the values of S.

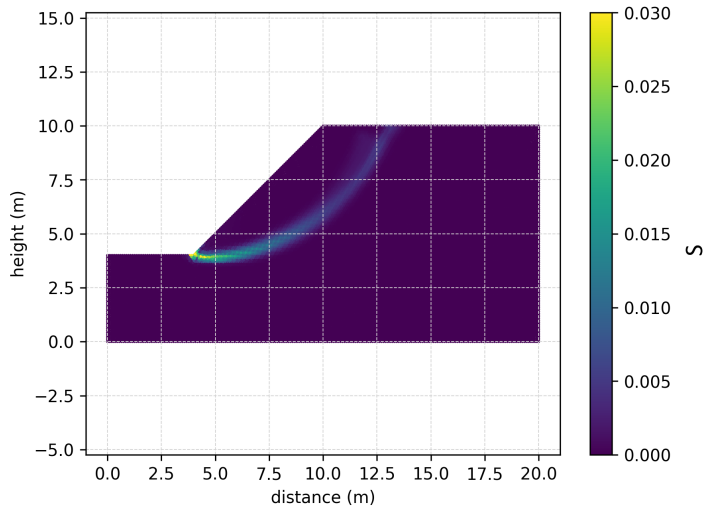

Figure 3.12. S for mesh h6. The nodes are color coded with the values of S.

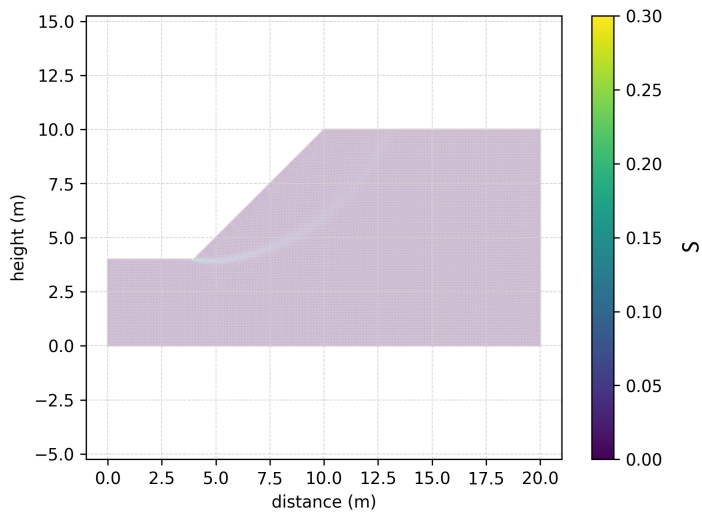

Figure 3.13. S for mesh h8. The nodes are color coded with the values of S.

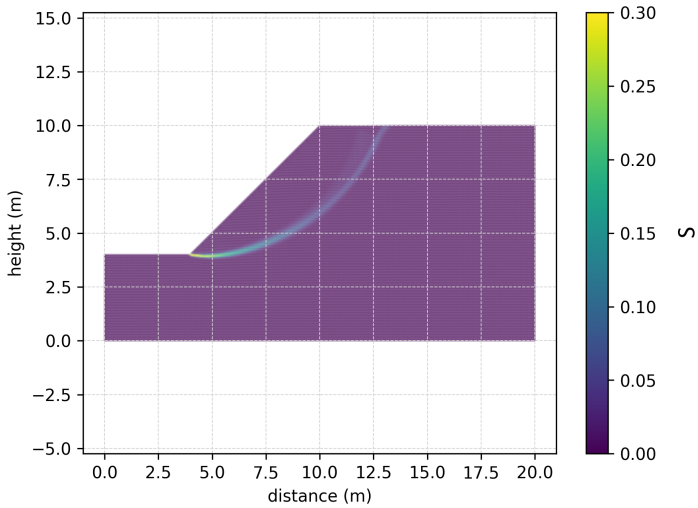

Figure 3.14. S for mesh h9. The nodes are color coded with the values of S.

The outcome of this strategy is highly promising. The approach is not only simple and straightforward but also effectively replicates the band of maximum S values. This is clearly illustrated in Figure 3.16, where the sliding surfaces extracted through this method are plotted together in different colors. As shown, these surfaces closely follow the regions of maximum strain, aligning well with the expected behavior.

To provide a more focused view, Figure 3.17 highlights four out of the nine extracted sliding surfaces. In this figure, the alignment with the areas of maximum strain is even more evident, demonstrating the robustness of this method in capturing the critical zones of deformation.

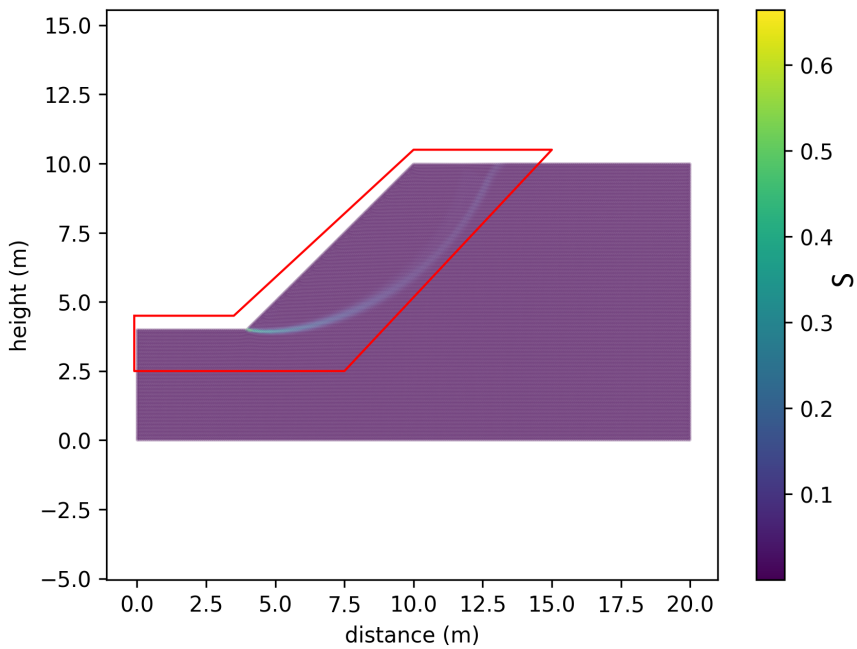

Figure 3.15. S for mesh h9. The nodes are color coded with the values of S. In red, the polygon outlines the area used to select the nodes for interpolation.

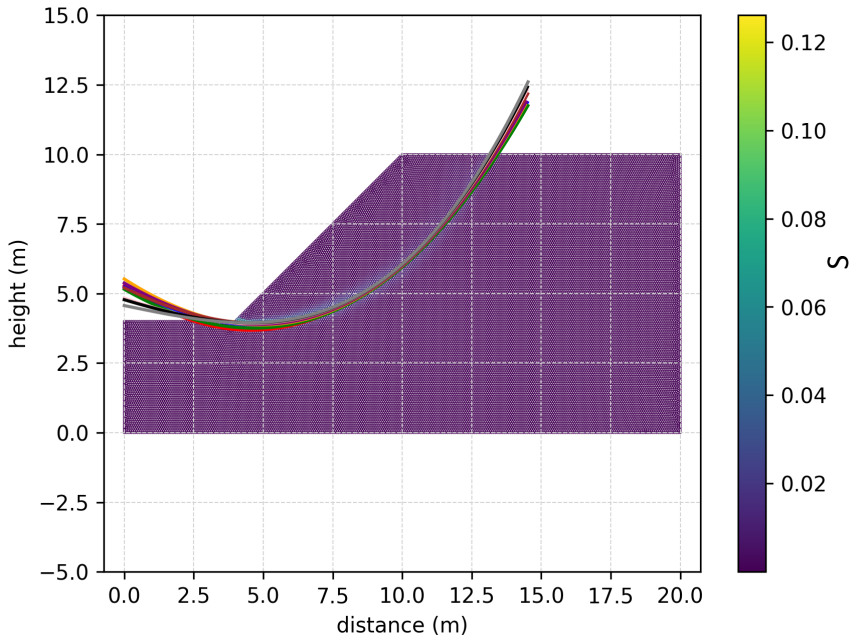

Figure 3.16. All nine extracted sliding surfaces, corresponding to meshes h1 through h9, are shown in the following colors: red, blue, green, orange, purple, brown, pink, black, and grey. The nodes are color coded according to the values of S.

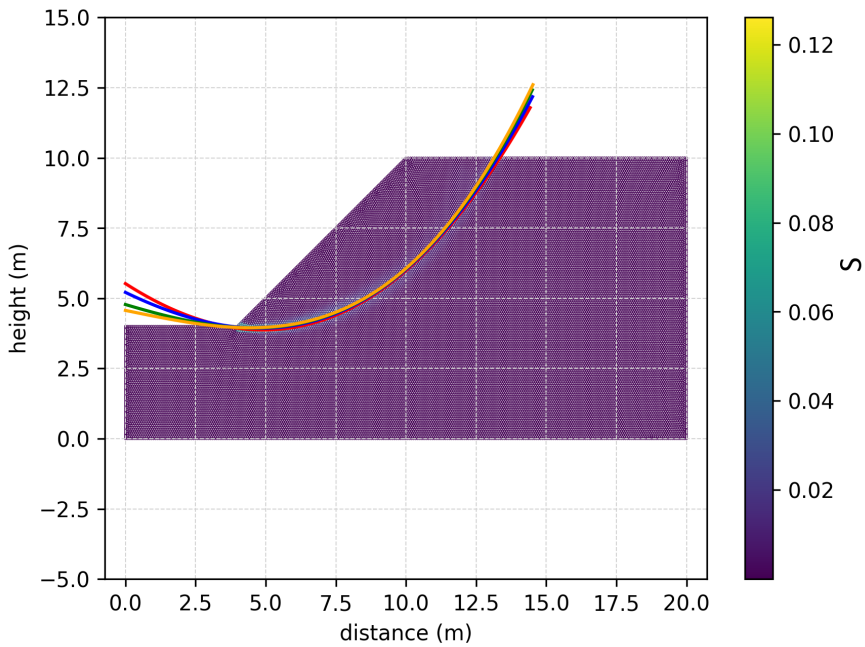

Figure 3.17. Four of the sliding surfaces extracted: h4 in red, h6 in blue, h8 in green and h9 in orange. The nodes are color coded according to the values of S.

3.2 Validation

This section focuses on evaluating the robustness of our method for extracting sliding surfaces. To thoroughly assess this, we revisited the same case study introduced at the beginning of Section 3.1, expanding the analysis by considering three additional scenarios. These scenarios maintain the same slope geometry, soil density ($20kN/m^3$), elastic modulus (14 MPa) and Poisson ratio (0.3), but differ in terms of cohesion and friction angle, following the approach outlined in [3] and [11].
For each scenario, we conducted a stability analysis using the SOCP-FEM algorithm to identify the sliding surface, which was then used as input data for the MLD software. The comparison between the two algorithms, particularly in terms of the FoS, enables us to evaluate the consistency and reliability of the sliding surfaces produced by our method. By examining how these surfaces influence the stability results within the MLD framework, we can determine the robustness and overall effectiveness of our approach.

The results of this analysis are reported in Table 3.3. The four sliding surfaces extracted for each scenario are shown in Figure 3.18.

Table 3.3. Factor of Safety for the four cases tested. The Limit Equilibrium Method (LEM) and the Strength Reduction Method (SRM) results are taken from Cheng et al. [11]. Diff1 represents the percentage difference in absolute value between SRM and SOCP-FEM, while Diff2 is the percentage difference between SOCP-FEM and MLD.

Case ID	Cohesion (kPa)	Friction Angle (°)	LEM	SRM	SOCP-FEM	MLD	Diff1	Diff2
1	5	5	0.41	0.43	0.42	0.43	2.3 %	2.3 %
2	5	15	0.70	0.73	0.71	0.69	2.7 %	2.8 %
3	5	25	0.98	1.03	0.99	0.96	3.9 %	3.0 %
4	5	35	1.28	1.35	1.30	1.27	3.7 %	2.3 %
5	2	5	0.25	0.26	0.26	0.25	0 %	0 %
6	2	45	1.35	1.44	1.38	1.37	4.1 %	1.5 %
7	20	5	1.06	1.20	1.17	1.12	2.5 %	5.6 %

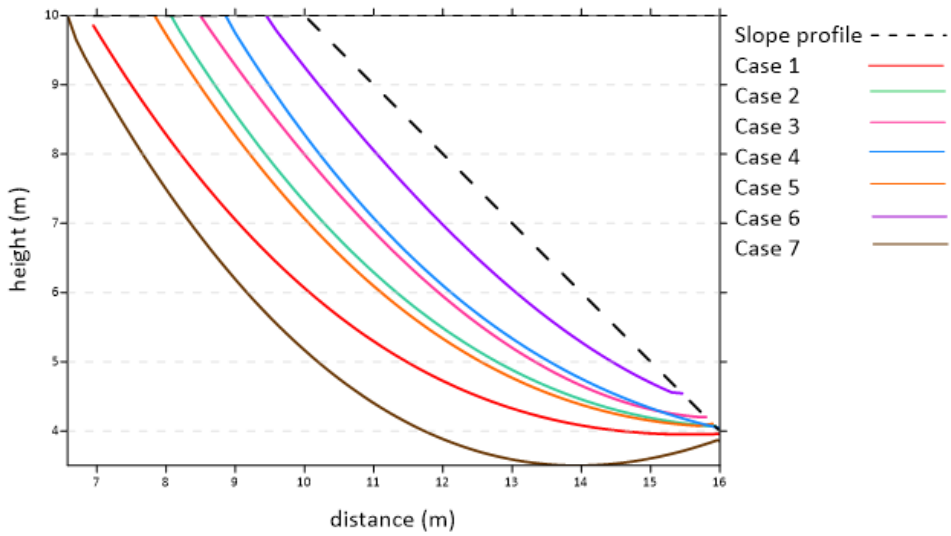

Figure 3.18. The seven sliding surfaces extracted from the SOCP-FEM software and used in the MLD analysis.

Lastly, we compared our extracted sliding surfaces with those provided by Cheng et al. [11], for both the Limit Equilibrium Method (LEM) and the Strength Reduction Method (SRM). The critical failure surface in their work is evaluated by the modified simulated annealing technique as proposed by Cheng [44].
This comparison was limited to cases 5, 6, and 7, as they are the only ones also included in the referenced work. Figures 3.19, 3.20, and 3.21 show the three sliding surfaces: the black and red lines represent the two surfaces provided by Cheng et al., while the blue line represents the one derived from our method. Since our FEM-based approach is also rooted in the SRM, it is expected to show similarities with Cheng et al.'s SRM-derived surface. However, some notable differences arise depending on the soil properties:

- In low-cohesion soils (Case 5 and Case 6), our failure surface is shifted further upslope and towards the right compared to those from Cheng et al. [11]. This suggests that our method may capture a different failure

mechanism, possibly due to variations in how stress redistribution is managed during the reduction process.

- As the friction angle increases, the right end of the failure surface moves closer to the crest, aligning more with the LEM-derived surface. This is consistent with the fact that higher internal friction leads to more localized failure [51].
- In Case 7, where the soil has higher cohesion and a lower friction angle, our result initially follows the SRM-based surface but intersects with the LEM-based surface near the crest. This suggests that, in cohesive materials, our method produces a failure surface that shares characteristics of both approaches.

These differences highlight how our SOCP-FEM approach reacts to variations in soil properties, offering an alternative way to identify failure mechanisms directly from the numerical response of the system, making it more adaptable to complex stress redistributions.

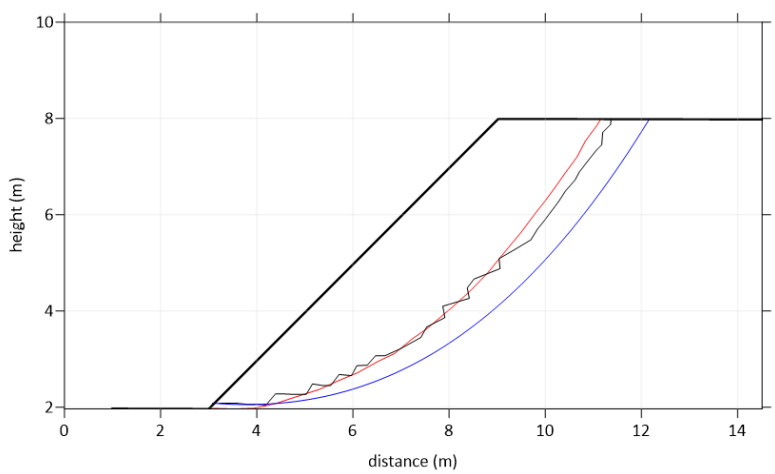

Figure 3.19. Comparison of the extracted sliding surfaces for Case 5. The bold black line represents the ground profile, the red line corresponds to the LEM, the thin black line to the SRM, and the blue line represents our approach.

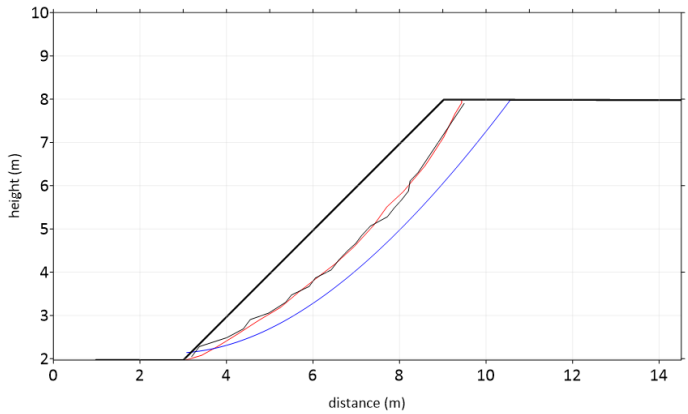

Figure 3.20. Comparison of the extracted sliding surfaces for Case 6. The bold black line represents the ground profile, the red line corresponds to the LEM, the thin black line to the SRM, and the blue line represents our approach.

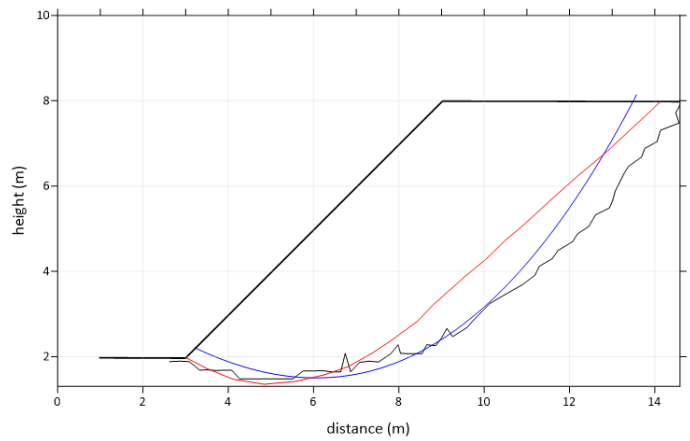

Figure 3.21. Comparison of the extracted sliding surfaces for Case 7. The bold black line represents the ground profile, the red line corresponds to the LEM, the thin black line to the SRM, and the blue line represents our approach.

Chapter 4

The Vado Ligure offshore: a possible site to host a Floating Storage and Regasification Unit

This chapter presents an application of the MLD method to a problem of high industrial and environmental relevance: the foreseen transfer of the Floating Storage and Regasification Unit (FSRU) presently installed at the Piombino (Tuscany) harbor to the Vado Ligure (Liguria) offshore. Only the MLD method was used in this analysis, as the SOCP-FEM method is currently not capable of accounting for water loading.
In the first Section we are going to introduce the study site and the motives of this analysis. Section 4.2 will deal with the stability analysis itself: first, we will introduce all the necessary considerations regarding the various input parameters required by the software, then we will proceed with evaluating the results from the stability analysis.
Lastly, Section 4.3 will present the sensitivity analysis conducted to assess the effects of varying the geotechnical parameters that characterize the soil.
This chapter was primarily written to be included in the technical report prepared in 2023 by the Tsunami Research Team at the University of Bologna, commissioned by T.EN Italy Solutions S.p.A. [52].

4.1 Study site

Vado Ligure is a coastal town in the Liguria region (northwestern Italy), located along the Ligurian Sea. It is situated about 50 kilometers west of Genoa

and near the city of Savona (Figure 4.1).
This area was selected for the relocation of the Piombino regasification vessel, which is scheduled for the second half of 2026. This choice was driven not only by the need for a regasification terminal in the central-northern region of the country, where gas consumption is higher, but also for its proximity to the national gas transmission network. The relocation strengthens energy security for industrial and residential needs, while minimizing environmental impacts by keeping the facility offshore.
To rigorously evaluate the safety and feasibility of the planned relocation, T.EN Italy Solutions S.p.A. commissioned the Tsunami Research Team of the University of Bologna to conduct the following essential studies:

1. the assessment of the impact of potential tsunamis generated by earthquakes and landslides in the offshore area of Vado Ligure, where the FSRU mooring is located;
2. the study of the seabed stability along the pipeline connecting the mooring to the mainland.

In this chapter, we will focus exclusively on the seabed stability analysis, as it is the main subject of this thesis.

Figure 4.1. Location of the study area near Vado Ligure (red star) along the Ligurian coast, with a zoomed-in view of the offshore region under investigation.

4.2 Stability analysis

As already mentioned, this study aims to assess the stability of the seabed along the section of the gas pipeline that connects the mooring to the mainland (red line in Figure 4.2). As shown in the map, the initial part of the pipeline, near the mooring, , marked by a red star in the plot, is located close to the head of a submarine canyon carving the shallow water platform, about 2 km east of the port of Vado Ligure.
In the absence of detailed studies in the area, which describe potential unstable masses along this submarine structure, it was decided to identify a series of transects that intersect the pipeline and partially cover the steep slope characterizing the canyon. As a result, ten profiles were obtained, whose extent is shown in green in Figure 4.2.

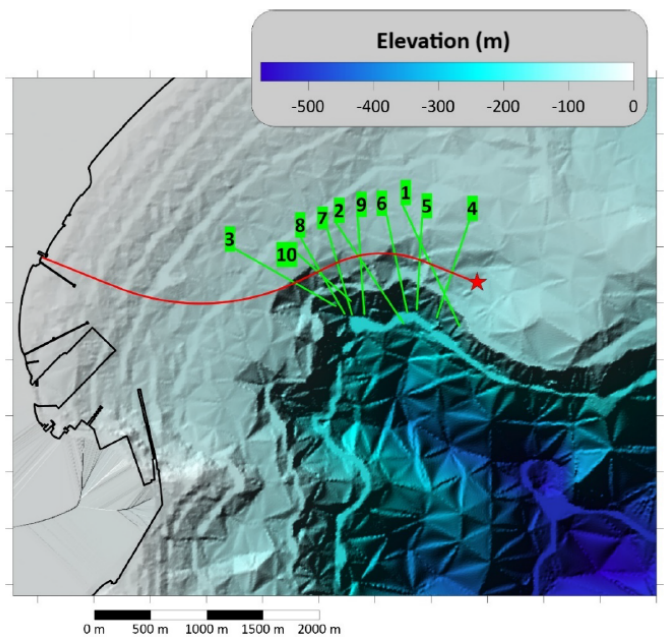

Figure 4.2. Transects considered for the stability analysis using the MLD method (in green). The extent of the pipeline connecting the mooring (represented by the red star) to the mainland is shown in red.

Below are reported the considerations made for the creation of the necessary inputs for the application of the code.

Topographic profile: for the detailed studies of instability, we used the bathymetric dataset provided by T.EN Italy Solutions. The total area covered by the dataset is of approximately 25 km^2, with a a 50-meter resolution and referenced in the UTM 32N coordinate system. The topographic profiles were obtained as vertical sections of this bathymetry, taken along the transects shown in Figure 4.2.

Slip surface profile: this information allows us to identify the mass whose stability is being studied. In the absence of detailed information on the geology and local structures that would allow us to define failure surfaces, it was decided to define, for each studied transect, a series of slip surfaces identified by circular arcs. These arcs intersect the seabed and encompass the pipeline. Although this approach involves a simplified geometry, it allows for a quick assessment of seabed stability over a broad range of potential events. In this study, three circular arcs were considered as potential slip surfaces for each transect.
To establish a reference for the landslide volume to be reproduced, we relied on the MaGIC database (Marine Geohazards along the Italian Coasts, funded by the Department of Civil Protection from 2007 to 2012 [53]). The MaGIC project focused on studying and assessing the hazards of the seabed along the Italian coastlines, with the aim of providing useful elements for risk mitigation and emergency management.
Within the scope of the project, several shallow-water events were identified along the Ligurian coast. Based on the event geographically closest to our area of interest, a landslide scenario was reconstructed using purely morphological considerations, representing small-volume detachments that typically occur in shallow waters, often at the head of the various submarine canyons cutting into the Ligurian margin. Using our circular arcs, we then aimed to reproduce volumes compatible with those reconstructed through this method.
Table 4.1 contains the geometrical parameters of the landslide scenario used as reference.

Table 4.1. Geometric parameters for the landslide scenario.

Volume ($10^6 m^3$)	Area ($10^3 m^2$)	Average initial thickness (m)	Maximum initial thickness (m)
2.88	182.5	15.8	29.9

Geotechnical parameters: similarly, due to the lack of specific details about the studied area, a simplified approach was chosen, considering the mass involved in the stability study to be homogeneous, without stratification. Regarding the geotechnical parameters required by the numerical code, the values derived from the study by Ai et al. [12], concerning the Ligurian Sea area (although not specifically the Vado Ligure), were used. Table 4.2 lists the density, cohesion, and internal friction angle parameters used for these analyses.

Table 4.2. Geotechnical parameters retrieved from Ai et al. [12].

Density (kN/m^3)	Cohesion (kPa)	Friction Angle (°)
17.25	7	31

Seismic load coefficient: an analysis of the Parametric Catalog of Italian Earthquakes (CPTI15 v4.0.0) [6] reveals a notable occurrence of historical earthquakes with moderate magnitudes (4–5) in the Vado Ligure area. Larger historical earthquakes have estimated epicenters along the coastal region near and west of Imperia, as shown in Figure 4.3. Among these, the earthquake on 23/02/1887, with a magnitude of 6.3, stands out as one of the most severe events in Liguria, resulting in over 650 fatalities.
To further improve this analysis, we also refer to the DISS database [7], a georeferenced and parameterized catalog of tectonic structures and active faults capable of producing earthquakes with magnitudes exceeding 5.5. Figure 4.3 shows both the Composite Seismogenic Source (in red) and the Individual Seismogenic Source (in green). The proximity to the coast and the maximum expected magnitude (Mw = 7.4) further confirm the need to seriously consider seismic loading when conducting the seabed stability analysis.

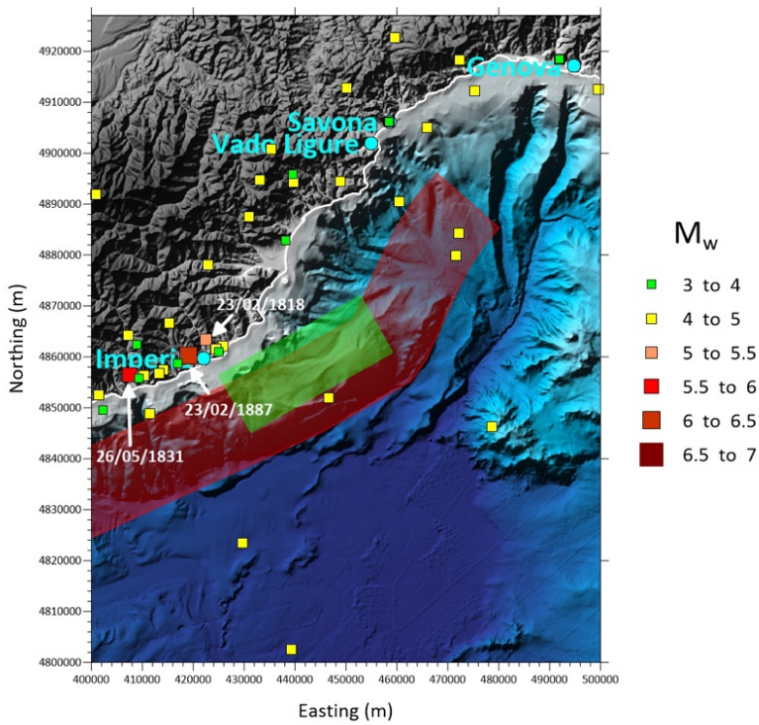

Figure 4.3. Historical earthquakes from the CPTI15 catalog [6] and seismogenic sources from the DISS [7].

Given this context, both water level and seismic load are essential inputs in the MLD software. The water level information is included in the bathymetry, whereas the seismic load requires further evaluation. This factor is included in the equations for calculating the FoS as a parameter representing the maximum ground acceleration in its vertical and horizontal components. This inevitably simplifies the situation, as a dynamic event is described by a single static, instantaneous value. However, using the maximum value can be considered a reasonable compromise between accurately representing the natural phenomenon and minimizing the computational effort required.
There are various strategies that can be adopted to assign the seismic load. For example, we can refer to the Italian Seismic Hazard Map MPS04 [54], [55],

which provides estimates of the expected Peak Ground Acceleration (PGA) across Italy. Specifically, this is expressed as a fraction of the gravitational acceleration g, representing the horizontal ground acceleration with a 10% probability of being exceeded over 50 years, based on rigid soils. Figure 4.4 shows the values for the 16th, 50th, and 84th percentiles along the western coast of the Ligurian Sea. In the most extreme case, expected values for the Vado Ligure area (highlighted in red) are below 0.08 g.
To account for the inevitable uncertainties inherent in this approach, which, for example, does not allow for consideration of potential local amplifications, a sensitivity analysis was conducted on the studied cases with respect to PGA, varying it between 0.2 g and 0.7 g.

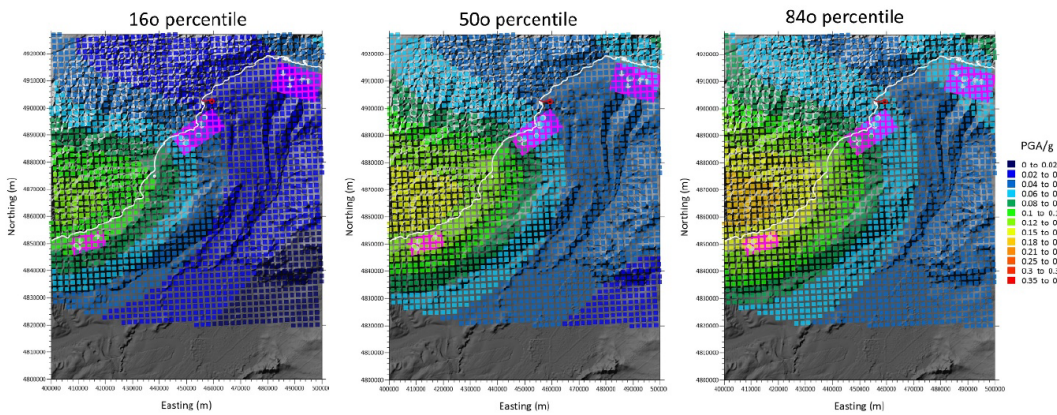

Figure 4.4. Seismic hazard maps extracted from MPS04, showing the 10% probability of exceedance over 50 years for PGA/g, with three different percentiles. The FSRU mooring area is highlighted in red, while the areas potentially destabilized according to the MaGIC database are shown in fuchsia.

4.2.1 Stability analysis results

Based on all the input data considerations presented in the previous section, the MLD code was applied to the whole set of scenarios. As previously noted, for each transect, three possible circular arcs were hypothesized as slip surfaces (circles A, B, and C).
As an additional sensitivity analysis, the angle defining the direction of the PGA was varied between -45° and 45°: negative angles indicate a PGA directed upwards, while positive angles indicate a downward direction.
For each configuration (comprising transect – circular arc – PGA/g value – PGA angle), a value for the Factor of Safety was obtained. Table 4.3 shows the lowest FoS value obtained for each transect and circular arc, corresponding to the highest PGA/g value used. It can be noted that the critical instability value, FoS = 1, is never crossed: indeed, no configuration shows a FoS value below 2. The transects with the lowest values are 2, 7, 8, and 9. As shown in Figure 4.5, which illustrates the position of the transects and the minimum FoS value for all configurations considered for each of them, those closest to instability (i.e., with the lowest FoS values, shown in red) are located at the head of the submarine canyon. The mooring area, on the other hand, near transects 1 and 4, appears to be more stable based on these results.

Table 4.3. FoS values obtained for the considered landslide cases, referring to a PGA/g value of 0.7. Yellow cells correspond to the lower FoS (less than 3).

No. Transect	Minimum FoS (Arc A)	Minimum FoS (Arc B)	Minimum FoS (Arc C)
1	6.03	3.87	4.58
2	2.50	2.16	2.22
3	4.15	2.74	3.55
4	3.50	3.88	3.07
5	2.66	3.73	2.96
6	3.80	3.54	4.25
7	2.48	3.18	2.64
8	3.31	2.26	2.52
9	2.15	2.63	2.15
10	5.98	2.77	4.12

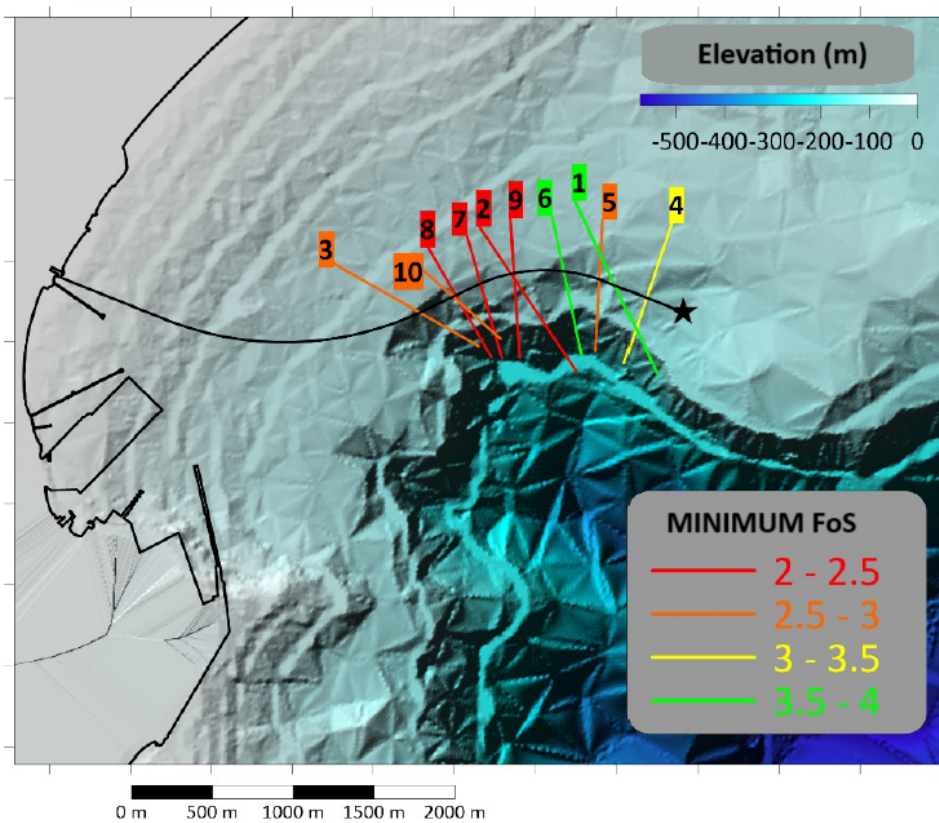

Figure 4.5. Map of the transects used for the stability study: the color codes correspond to the minimum FoS value obtained for each transect, based on the different configurations studied.

Figures 4.6, 4.7, 4.8 show the stability study results for 3 transects for each selected slip surface. The three selected profiles are numbers 1, 4, and 5, which are the closest to the mooring. In the graphs on the left, the slip surface is represented by a pink circle, the sea level is indicated by the light blue dashed line, and the red diamond marks the position of the pipeline along the bathymetric profile. On the right, three curves are shown for each circle, each representing a different value of the PGA inclination angle. These curves illustrate the dependency of the FoS on ground acceleration, expressed as PGA/g.

It can be observed that, in every scenario, the PGA angle that minimizes the Factor of Safety corresponds to 0° (i.e., completely horizontal PGA). In no case does the curve representing the variation of FoS with respect to PGA/g intersect the red dashed line, which identifies the critical value FoS = 1, thus confirming an overall stable condition.

When analyzing the individual transects, a variation in results can be seen based on the slip surface (for example, see the graphs for transect 5 in Figure 4.8). As the landslide volume increases, the curves shift downward toward the critical value (Circles A and C, representing the largest mass, shows the lowest FoS values), but without ever reaching the point of instability.

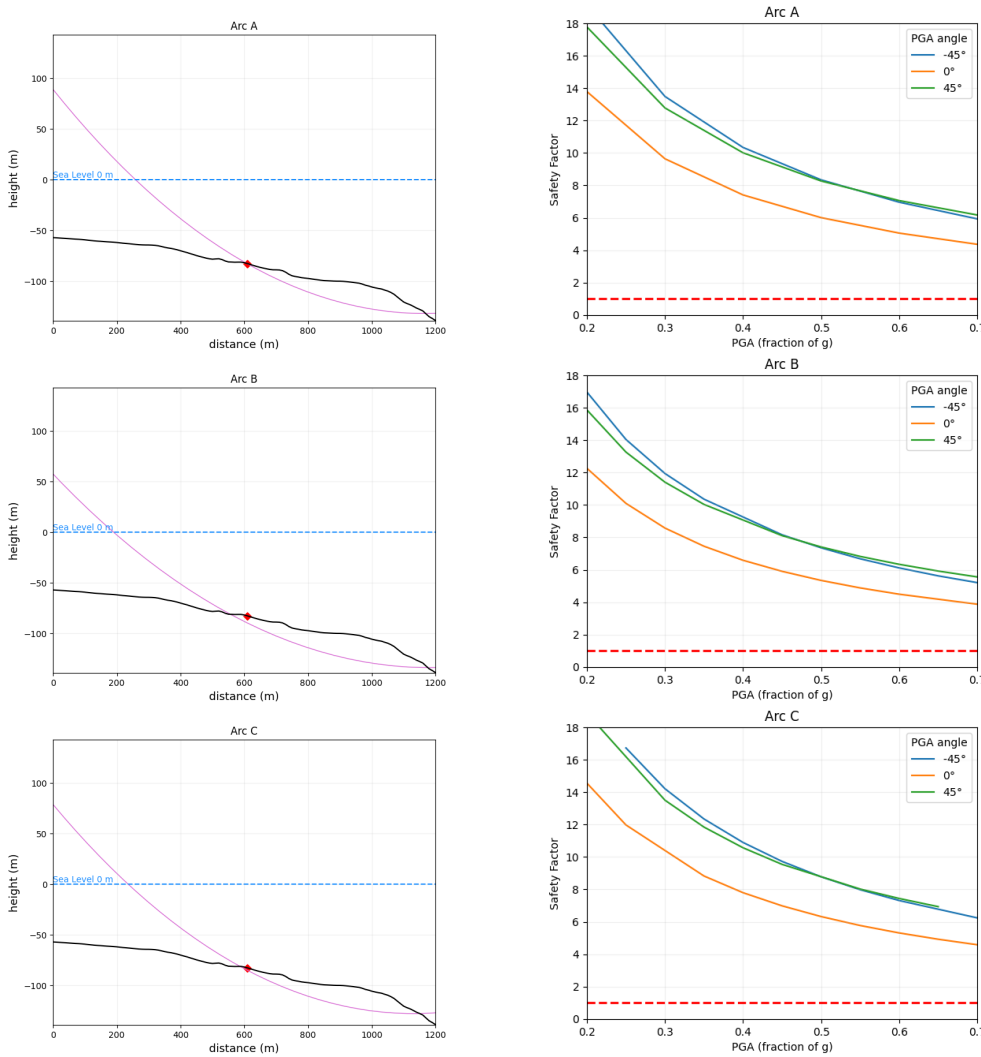

Figure 4.6. Transect 1 (see map in Figure 4.5). Left graphs: Bathymetric profiles (in black), circles identifying the slip surface (in pink), pipeline position along the profile (red diamond), and sea surface (light blue dashed line). Right graphs: Variation of FoS value with respect to PGA/g, for three different inclination angles -45°, 0°, 45°. The red dashed line represents the critical FoS value.

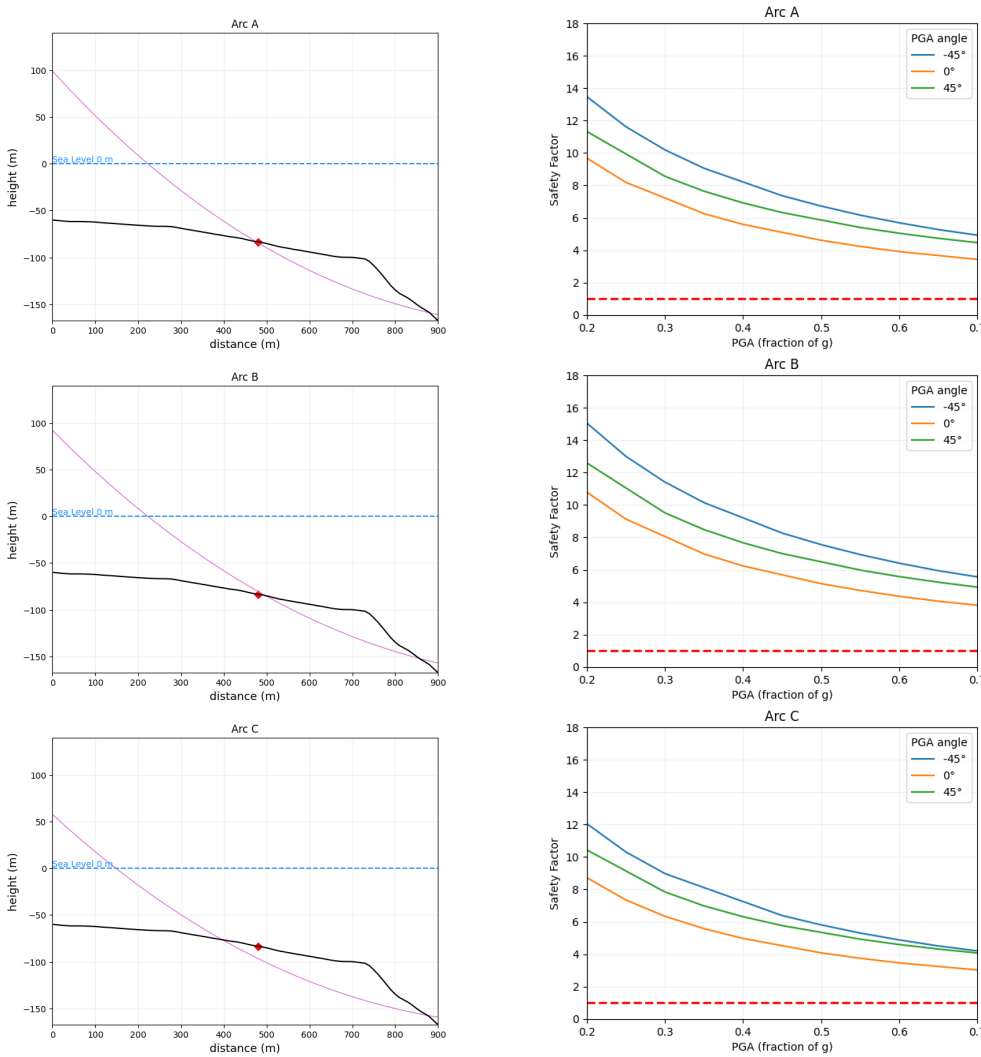

Figure 4.7. Transect 4 (see map in Figure 4.5). Left graphs: Bathymetric profiles (in black), circles identifying the slip surface (in pink), pipeline position along the profile (red diamond), and sea surface (light blue dashed line). Right graphs: Variation of FoS value with respect to PGA/g, for three different inclination angles -45°, 0°, 45°. The red dashed line represents the critical FoS value.

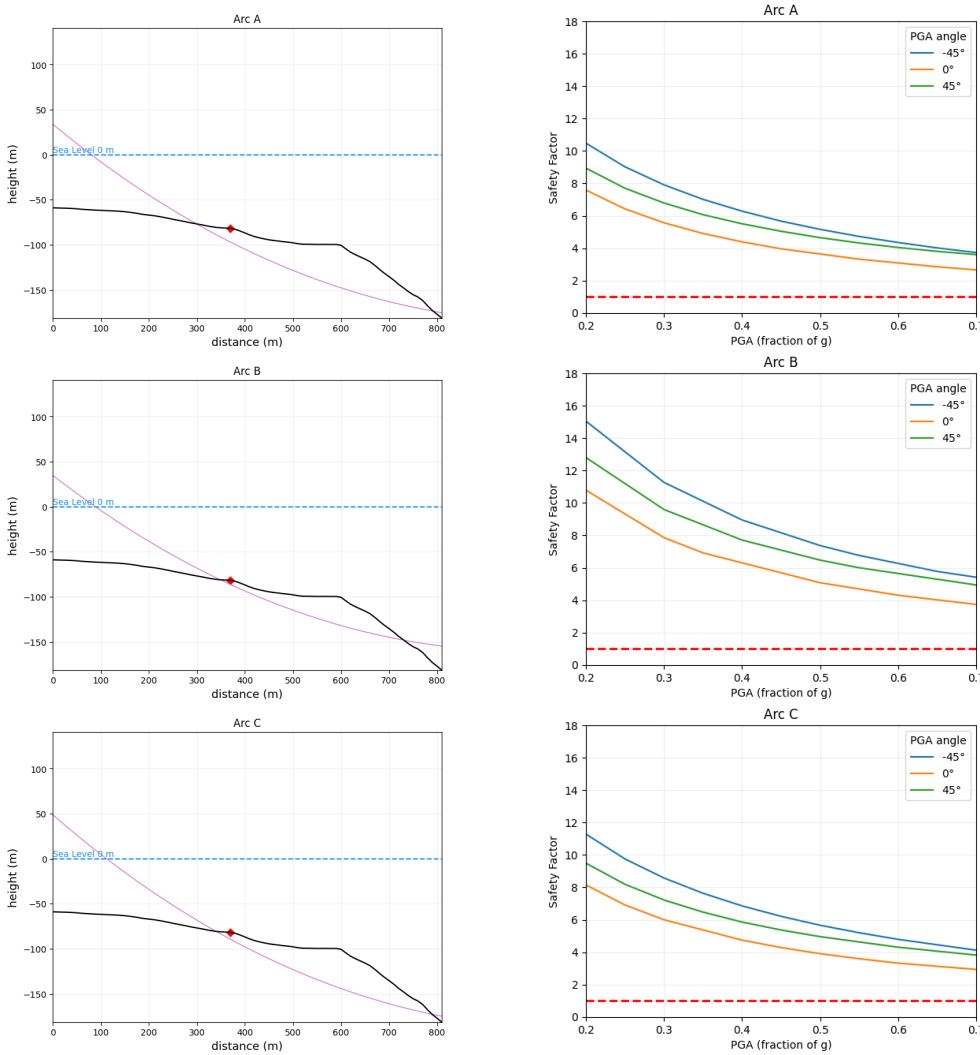

Figure 4.8. Transect 5 (see map in Figure 4.5). Left graphs: Bathymetric profiles (in black), circles identifying the slip surface (in pink), pipeline position along the profile (red diamond), and sea surface (light blue dashed line). Right graphs: Variation of FoS value with respect to PGA/g, for three different inclination angles -45°, 0°, 45°. The red dashed line represents the critical FoS value.

4.3 Sensitivity Analysis

To assess the effects of varying the geotechnical parameters that characterize the soil, it was decided to modify the value of the internal friction angle ϕ. Starting from the reference value used previously (31°), it was increased and decreased by 3° (resulting in 28° and 34°). The results for transect 8 are shown in Figure 4.9, which displays the FoS curves with respect to PGA/g as the inclination angle of the latter varies.
It is clear that increasing the friction angle causes the curves to move further away from the critical FoS value, indicating an increase in slope stability. Conversely, a decrease of just 3° in the ϕ parameter causes a significant drop in FoS values, even falling below 2 for Circle B.
It is essential to highlight the lack of specific studies on the geotechnical soil characterization in the Vado Ligure area, which limits established methods for seabed stability analysis in this context. As a result, the selection of geotechnical parameter intervals in this study was largely subjective, though based on reasonable assumptions, introducing some degree of uncertainty.
Even with these approximations, the results suggest that the project is not expected to face any stability issues related to the seabed.

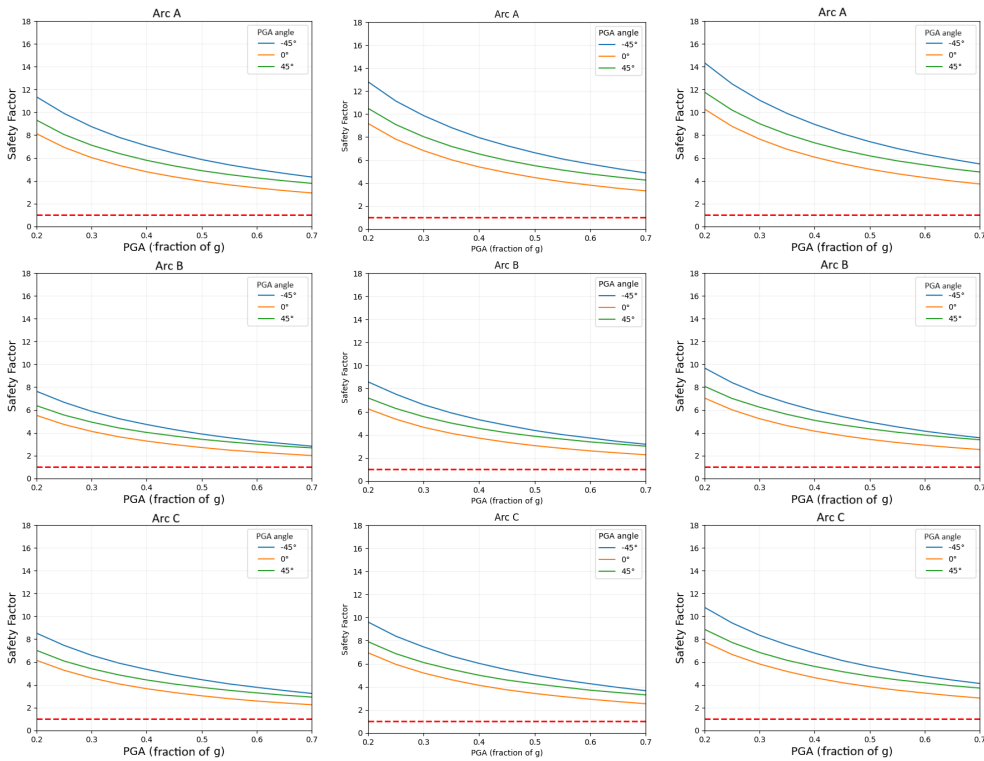

(a) $\phi = 28°$ **(b)** $\phi = 31°$ **(c)** $\phi = 34°$

Figure 4.9. Sensitivity analysis of the Factor of Safety with respect to internal friction angle ϕ. The three circles of transect 8 are considered (see map in Figure 4.5). The three curves refer to different values of the PGA inclination angle.

Chapter 5

Tavernola Landslide

This chapter presents the application of the SOCP-FEM method to the Tavernola landslide, located near Lake Iseo in Italy. After defining the problem in Section 5.1, stability analysis is conducted using the SOCP-FEM algorithm, following the workflow outlined in Chapter 3. The slope profile is studied using various meshes with different resolutions, and the convergence of the extracted sliding surfaces is assessed. Comparisons are made with sliding surfaces derived from geotechnical investigation, followed by an evaluation of the area and position of the sliding surface.
Lastly, in Section 5.3, we propose an approach to link our result to the study of collapse dynamics: we will introduce Kratos Multiphysics (hereafter referred shortly to as Kratos), a framework for building parallel multi-disciplinary simulation software. In particular we will focus on the Particle Finite Element Method (PFEM), a strategy that combines the finite element solution of the governing equations in Lagrangian form with an efficient remeshing strategy to deal with large deformation problems [56]. The results of this analysis are reported in Section 5.3.2.

5.1 Study Site

The Iseo Lake is the fourth largest lake in northern Italy, with a surface area of around 60.9 km^2. It is situated in Lombardy, and forms a natural boundary between the provinces of Bergamo and Brescia (Figure 5.1). The basin reaches a maximum depth of 256 meters and its surface has an average elevation of 185 meters a.s.l. [57], [58]. It is enclosed by mountains from 1000 to 1400 meters a.s.l. [59] in its northern and central part and the main inflow and outflow of

the lake is represented by the Oglio River and its tributaries. Additionally, Monte Isola Island in the central part of the lake is one of the largest lake islands in Europe with a surface area of $\approx 4\ km^2$ and peak elevation of around 235 meters a.s.l. [58]. The lake basin was originated by Pleistocene glacier activity, that reshaped a late Miocene erosional canyon [60].

Figure 5.1. Map of the Iseo Lake area.

The area affected by the landslide is located on the eastern slopes of Monte Saresano, on the western shore of Lake Iseo. More specifically, it lies on the border between the municipality of Tavernola Bergamasca and the municipality of Vigolo, as shown in Figure 5.2 [61]. The area is characterized by significant tectonic complexities, including folds, faults, and thrust surfaces. Locally, these structures identify bedding planes inclined in a manner conducive to landslides on the slopes. Historical landslides have occurred in this area, at least from the 1970s up to the most recent significant event in

Figure 5.2. Zoom on the Landslide area.

2021 [61], [62]. Indeed, at the beginning of 2021, this landslide began moving in a concerning manner, prompting authorities to intensify constant monitoring. A study was also conducted to assess the potential tsunami that could be triggered by the landslide in the lake, along with an evaluation of the possible flooding along its shores [63].

5.2 Stability Analysis and Sliding Surface Determination

We conducted a stability analysis with the SOCP-FEM method, in order to test our strategy to extract sliding surfaces in a real case scenario.
First, we needed to select a 2D profile of the landslide. To do so we used a topo-bathymetric grid with a consistent spacing of 10 meters, generated by combining topographic and bathymetric data of the lake, provided by Profes-

sor Crosta's team from the University of Milano-Bicocca [8]. This grid, developed by the Tsunami Research Team from the University of Bologna [63], covers the central area of Lake Iseo. It includes the western zone impacted by the landslide and the village of Tavernola Bergamasca, with Monte Isola situated in the middle, directly facing the landslide, and extends along the eastern shore from Marone to Sulzano, as shown in Figure 5.3.

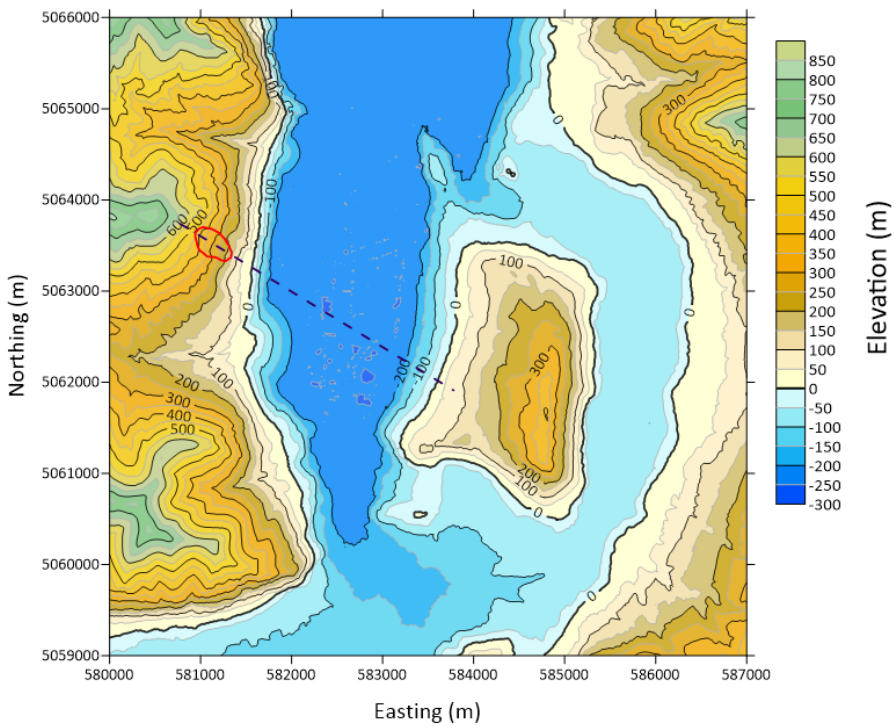

Figure 5.3. Topo-bathymetric grid of the area of interest. Axis coordinates are given in the UTM 32N coordinate system. The red polygon represent the Tavernola landslide, while the black dashed line is the chosen profile.

We then proceeded to extract a transect along the maximum slope gradient, in order to better characterize the landslide process (Figure 5.4).

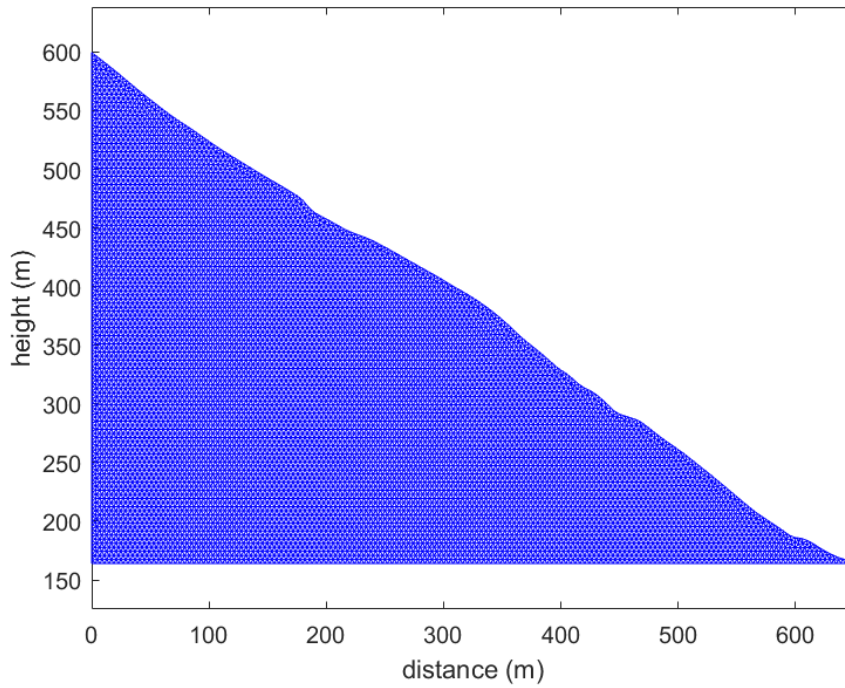

Figure 5.4. Profile and mesh for the Tavernola landslide. The height is intended relative to the lake level. In this case, the h parameter is set to 4, meaning a resolution of 2 meters.

The geotechnical parameters for this study were retrieved from the technical report by Casagli et al. [62]. In their study the slope is considered as a homogeneous body, completely dry, and made of a single material with a specific weight of 25 kN/m^3. They conducted 3D sensitivity analysis for friction and cohesion to determine their range of values for these geotechnical parameters that represent the critical conditions of the ongoing phenomenon along the slope. In our case, we aimed to identify a combination of parameters that would lead the slope to failure, as our focus also included the dynamic aspects of the landslide.
Therefore, the final combination of geotechnical parameters chosen is the one reported in Table 5.1.

Table 5.1. Geotechnical parameters for Tavernola landslide.

Density (kN/m^3)	Cohesion (kPa)	Friction Angle (°)	Elastic Modulus (MPa)	Poisson Ratio
25	30	27	14	0.3

We then proceeded to verify the convergence of our stability analysis in terms of the FoS, using different mesh resolutions. The tested meshes are summarized in Table 5.2. As shown in Figure 5.5, the Factor of Safety approaches a plateau around 0.83 for finer meshes. Even with coarser meshes, the errors are limited to the third decimal place, ensuring a reliable solution.

Table 5.2. Mesh discretizations from the coarsest to the finest for the Tavernola landslide.

Mesh ID	h	Number of Nodes	Number of Elements
h1	12	4907	2340
h2	10	6860	3307
h3	8	10495	5110
h4	7	13559	6632
h5	6	18295	8986
h6	5	26174	12897
h7	4	40621	20050

Comparing our 2D results with the 3D ones provided by Casagli et al. [62], their Factor of Safety (FoS) is reported as 1.05. This difference is expected: typically, the FoS in 3D analyses is higher than in 2D analyses, with studies indicating that discrepancies range between 3% and 30% [64].
The 3D modeling was conducted using SVSLOPE, a LEM-based software, part of the SVOffice package (SoilVision Systems Ltd) [65]. This software requires a predefined slip surface as input, which, in the case of Casagli et al. [62], was derived from geotechnical data. The Factor of Safety was computed using the Janbu simplified method for forces.

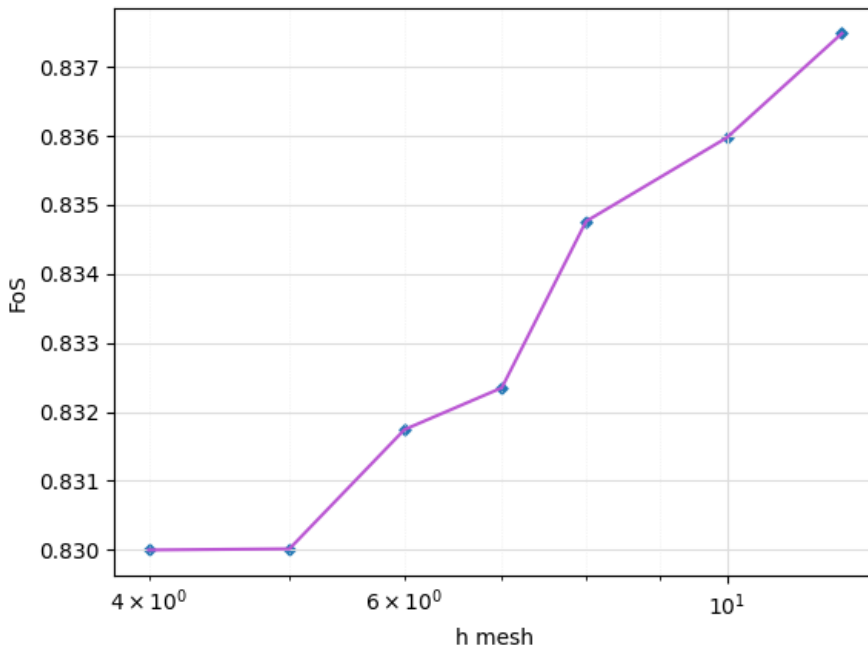

Figure 5.5. FoS for different resolution meshes. X axis is in log-scale.

The main reason for the discrepancy between 2D and 3D results lies in geometrical simplifications. In 2D models, the slope is assumed to be infinitely long and uniform along the third dimension (perpendicular to the cross-section), which simplifies the problem but often leads to conservative results. In contrast, real-world slopes exhibit more complex geometries, better captured by 3D models. These models account for the actual shape, variations in width and height, material distribution, and additional lateral support from surrounding materials [66], [67].

Following the general workflow of our strategy, we computed the S quantity, as defined in Chapter 3. Figure 5.6 illustrates the computation of S for the finest mesh analyzed (h7), revealing a well-defined and distinct strain band. Figure

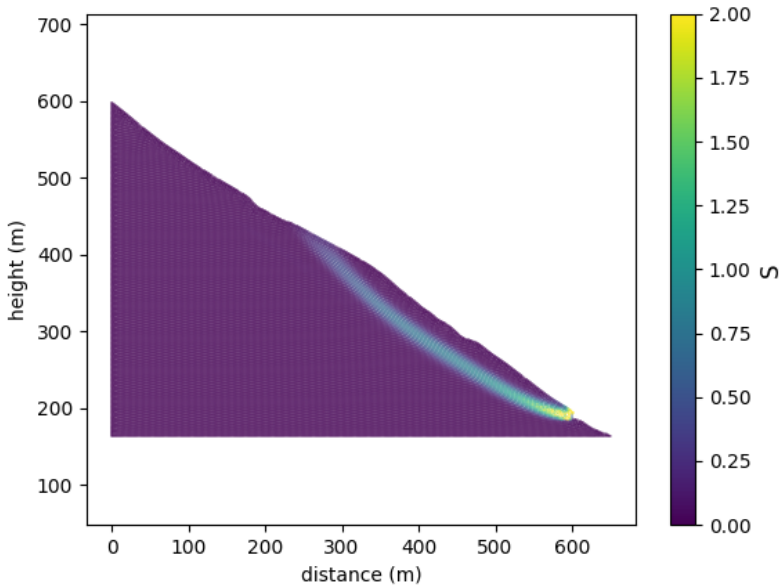

Figure 5.6. S quantity for h7 mesh.

5.7 shows the results of the cubic spline interpolation. As the mesh is refined, the curves clearly converge, with the mean maximum difference between the most distant points being 4.8 meters, which is satisfactory for our purposes. The mean maximum distance between the curves was calculated as follows: first for each x-value the maximum distance between the curves was calculated as the difference between the maximum and minimum y-values at that point, then the average of all the maximum distances was computed, providing a single representative value of the distance between the curves.

The final step of the strategy outlined in Chapter 3 involves using the obtained sliding surface as input for the MLD method and comparing the results in terms of the Factor of Safety. The sliding surface used as input is extracted from the finest mesh, h7, resulting in a Factor of Safety of 0.85 from the MLD method—2.4% higher than the value obtained with the SOCP-FEM.
Lastly, as far as concerns slope stability, we were able to compare our result

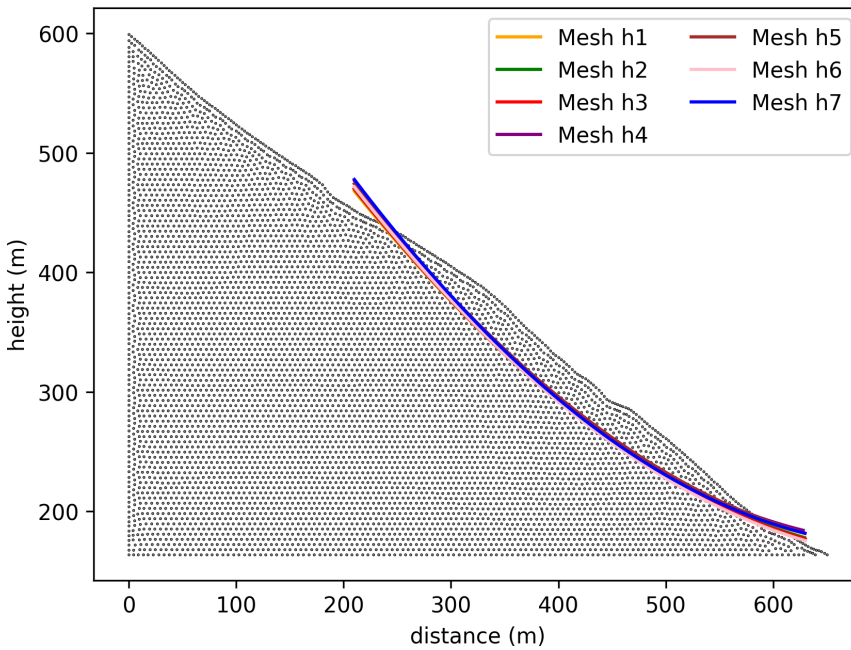

Figure 5.7. Extracted sliding surfaces for the seven different mesh tested.

with a sliding surface retrieved by geotechnical measurements. In particular the data used for the reconstruction of the sliding surface involve inclinometric measurements, HVSR (Horizontal to Vertical Spectral Ratio) measurements, geophysical sections and extensometric measurements [8].
The results of this analysis in comparison with our sliding surface (extracted from the finer mesh h7) can be seen in Figure 5.8.
The position of the failure surfaces obtained in this work (blue line) and by Crosta el al. [8] (red line) is quite similar. The main differences are exhibited in the upper part of the slope, where the red line extends deeper than the blue line. The two curves approximately coincide between the 350 m and 200 m elevation marks; however, the blue surface indicates a landslide body that ends ≈ 10 meters below the one outlined by the red line. We performed a simple estimate of some basic quantities, to compare the two surfaces. Results are summarized in Table 5.3. Our strategy in this case underestimates the

volume/unit width (m^2) of about 20%, while the total length and maximum depth of the surface is smaller than the one from Crosta et al. [8]. Despite these discrepancies, it is important to note that our method is applied to a continuous and homogeneous mass, not considering weak layers and rupture surfaces that exist in every real configuration, and that can be captured only by detailed geotechnical investigations. Given these limitations, the results still provide a reasonable approximation of the actual sliding surface.

Table 5.3. Comparison between the sliding surface extracted with our method and the one provided by Crosta et al. [8].

	SOCP-FEM	Crosta et al. (2021)
Volume/unit width (m^2)	12000	10000
Length (m)	430	460
Maximum depth (m)	30	45

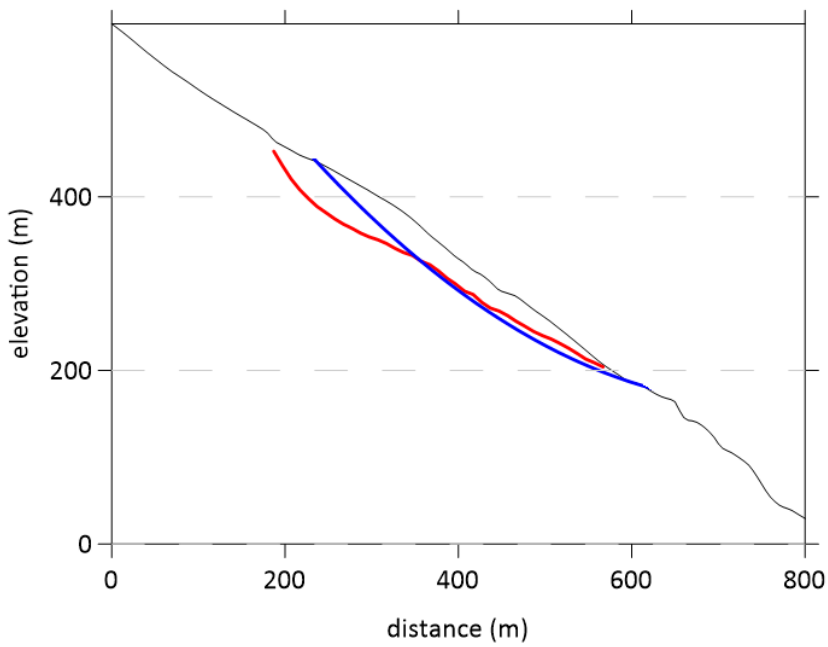

Figure 5.8. Comparison between our sliding surface (in blue) and the one retrieved from Crosta et al. [8] (in red).

5.3 Landslide Generated Wave Simulation

The last part of this study for the Tavernola landslide focused on the development of a POC that links the slope stability analysis and the consequent sliding surface extraction to the dynamic simulation of the landslide and of the landslide generated wave. Our purpose is to use the output of our stability analysis as input for the dynamic simulation, thereby developing a robust and reusable routine capable of analyzing the entire landslide event. This routine will encompass the whole process from the initial stability assessment, which focuses on the onset of the landslide, to the final stage, which includes simulating the potential tsunami triggered by the event. In this way, we aim to create an easy-to-use solution that connects the different stages of analysis, ensuring consistent, accurate, and efficient simulations that can be used in various case studies.
In order to do so we relied on Kratos Multiphysics, a framework for building parallel multi-disciplinary simulation software [68], [69]. It provides various tools that simplify working with finite element applications and offers a unified platform for smooth interaction between them. Kratos has an efficient and flexible data structure that can safely store any type of data. The framework uses Python scripting to define core procedures, which enhances its flexibility in use. It also supports parallel computing for both Shared Memory Machines (SMMs) and Distributed Memory Machines (DMMs). Additionally, it includes tools that help applications adapt their algorithms to these architectures, with scalability tested on systems with thousands of cores.
In particular, we used the Particle Finite Element Method (PFEM) formulation, that will be described in the following Section.

5.3.1 Particle Finite Element Method for LGW

The Particle Finite Element method solves the governing equations in a Langrangian framework combining the Finite Element Method (FEM) with a robust remeshing technique [70]. This method is commonly used to solve fluid-structure interaction (FSI) problems involving large deformations and large free surface motion and splashing waves [71], [72], [73].
The PFEM formulation used in this study relies on the computation of the standard infinitesimal equations for a viscous incompressible fluid. They can

be written, in a Lagrangian frame at the current time t, as follows:

$$\rho \frac{\delta v_i}{\delta t} - \frac{\delta \sigma_{ij}}{\delta x_j} - b_i = 0 \qquad \text{(Momentum Balance)}$$

$$\frac{\delta v_i}{\delta x_i} - \frac{1}{k}\frac{\delta p}{\delta t} = 0 \quad i, j = 1, n_d \quad in \quad \Omega \qquad \text{(Mass Conservation)}$$

where v_i is the velocity along the i-th global axis, ρ is the density of the fluid, σ_{ij} are the total stresses, b_i are the body forces, p is the absolute pressure, k the bulk modulus, n_d is the number of space dimensions and Ω is the fluid domain.
The total stresses equation is

$$\sigma_{ij} = s_{ij} - p\delta_{ij} \tag{5.1}$$

where δ_{ij} is the Kronecker delta, and s_{ij} are the viscous deviatoric stresses, i.e.:

$$s_{ij} = 2\mu \left(\dot{\epsilon_{ij}} - \frac{1}{3}\frac{\delta v_k}{\delta x_k}\delta_{ij} \right) \tag{5.2}$$

In the latter equation μ represents the viscosity and the strain rates $\dot{\epsilon_{ij}}$ are:

$$\dot{\epsilon_{ij}} = \frac{1}{2}\left(\frac{\delta v_i}{\delta x_j} + \frac{\delta v_j}{\delta x_i} \right) \tag{5.3}$$

In the PFEM, the above governing equations are integrated and discretized following a standard Finite Element Method (FEM) procedure. To facilitate the remeshing procedure, linear shape functions are used for both the velocity and pressure fields. Due to the incompatibility of these fields for a incompressible material solution, stabilization is required. In this formulation the finite calculus (FIC) method is employed. For more details, see [74], [75] and [76].
The general workflow of the PFEM algorithm can be summarized in the following steps [72]:

1 Remove all elements from the mesh and maintain the nodes;

2 Generate a triangular (or tetrahedral) mesh using the Delaunay Triangulation;

3 Recognize the physical boundaries of the domain using the Alpha Shape method.

4 Solve the governing equations of the problem for the time step increment with a Lagrangian FEM;

5 Update the mesh nodes position;

6 Before starting the new time step solution, check mesh distortion. If the mesh is distorted go to STEP 1, otherwise go directly to STEP 4.

5.3.2 Dynamic Simulation Results

The dynamic simulation was performed using the transect extracted from the topo-bathymetric grid in Figure 5.3. The resulting profile has a length of ≈ 4200 meters including Monte Isola Island and a maximum elevation of ≈ 500 meters above the lake water level, as shown in Figure 5.4.

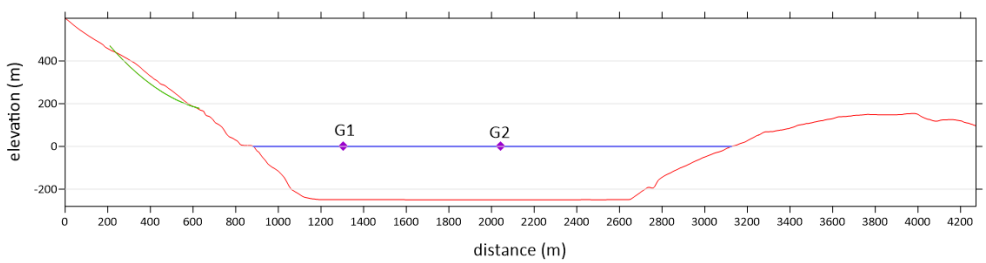

Figure 5.9. The red line represents the topo-bathymetric profile used for the dynamic simulation. The green line shows the sliding surface extracted from the finer mesh, as described in Section 5.2. The 0 height corresponds to the lake level, represented by the blue line. Violet symbols indicate the tide gauges positions. G1 x coordinate is 1306 m, while G2 is situated at 2042 m from the beginning of the profile.

The landslide body was modeled as frictional viscoplastic medium inspired to the Bingham model [56], while the water body was treated as a standard Newtonian fluid. The parameters for both models are summarized in Table 5.4.

We used multiple meshes with varying resolutions, both uniform and non-uniform, to assess the computational time needed for the analysis. The refined meshes are designed in order to have a fine resolution only where this is really required, namely in landslide run-out and impact zones. In particular:

mr1 : mesh with local refinement. The landslide and the impact zone are discretized with a mesh size of 5m. In the rest of the domain, the elements size is 20m. The total number of elements in the initial mesh is 12620 (Figure 5.10).

mr2 : mesh with local refinement. The landslide and the impact zone are discretized with a mesh size of 5m. In the rest of the domain, the elements size is 15m. The total number of elements in the initial mesh is 14279.

mu1 : uniform mesh of elements size 6m. The total number of elements in the initial mesh is 30646.

mu2 : uniform mesh of elements size 5m. The total number of elements in the initial mesh is 43957.

Table 5.4. Parameters for both the water and the sliding body.

	Landslide	Water Body
Constitutive Law	Frictional Viscoplastic	Newtonian
Density (kN/m^3)	25	10
Dynamic Viscosity ($Pa \cdot s$)	$1 \cdot 10^{-3}$	$1 \cdot 10^{-3}$
Bulk Modulus (Pa)	$2.1 \cdot 10^{9}$	$2.1 \cdot 10^{9}$
Friction Angle (°)	27	–
Cohesion (kPa)	30	–

Each analysis was performed over a total duration of 120 seconds, sufficient for the first wave front to reach Monte Isola Island. The simulations were deliberately not extended further to prevent spurious results from refraction effects, as the simulations were conducted in a 2D framework.

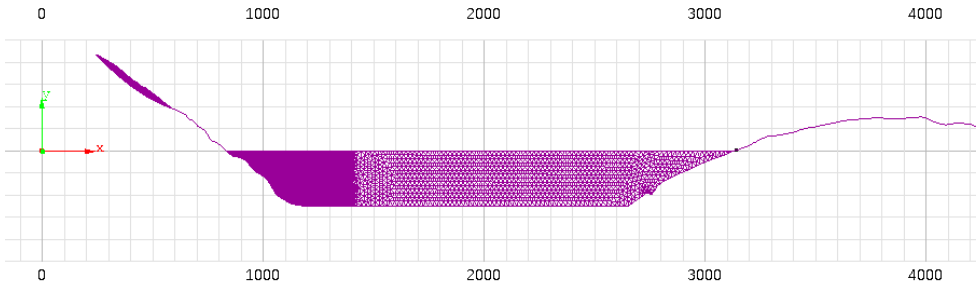

Figure 5.10. Non-uniform resolution mesh: the landslide and the impact area are treated with a 5 meter resolution mesh, while the rest of the water body has a 20 meter resolution (mr1).

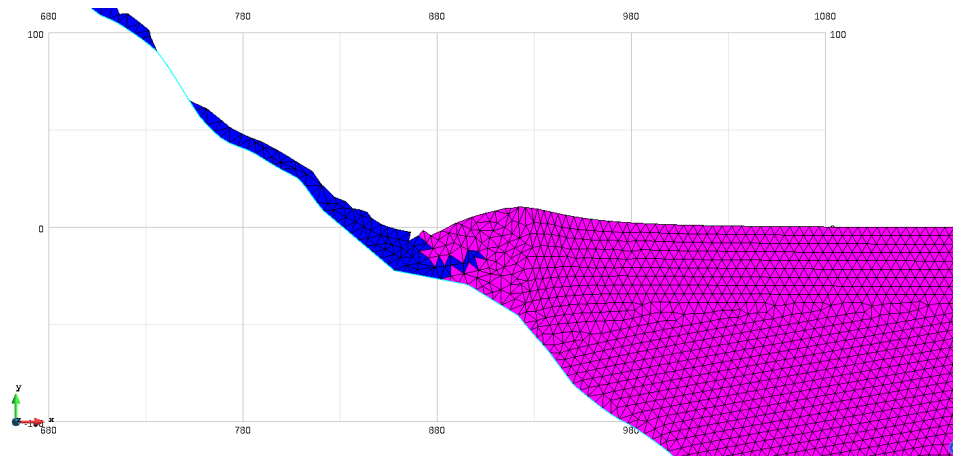

Figure 5.11. Mesh mu2 at t = 44 seconds. In blue the sliding mass, in pink the water body.

The landslide takes ≈ 40 seconds to reach the water basin. Figures 5.11 and 5.12 show the mesh at t = 44 seconds and t = 65 seconds for mesh mu2 : as we can see, the elements remain regular despite the large deformations of the bodies. Not all the sliding mass falls in the lake, but the most of it accumulates on the slope. The mass can be considered completely still after 60 seconds from the trigger. Figure 5.13 shows the final landslide deposition area after the impact with the water mass.

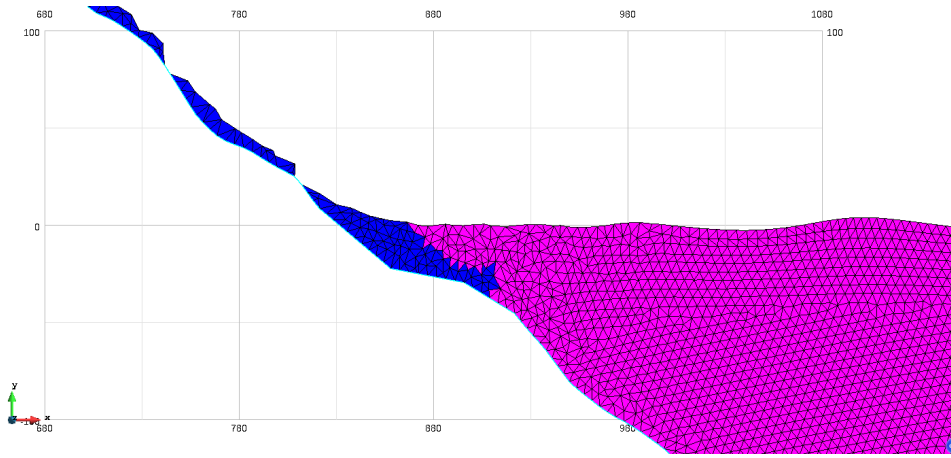

Figure 5.12. Mesh mu2 at t = 65 seconds. In blue the sliding mass, in pink the water body.

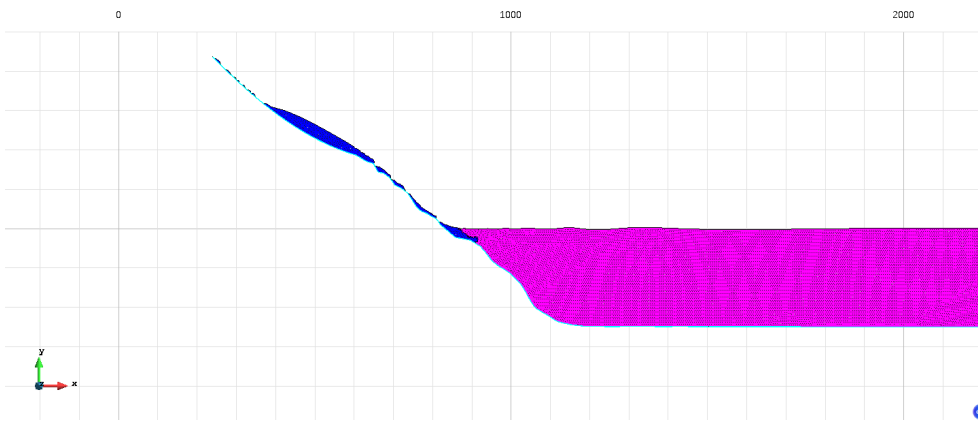

Figure 5.13. Landslide deposition area after the impact, for mesh mu2. In blue the sliding mass, in pink the water body.

The analyses show that the PFEM is able to reproduce the complete landslide generated wave scenario and all phenomena involved, namely, landslide runout, impact on the water reservoir, transfer of momentum from the land-

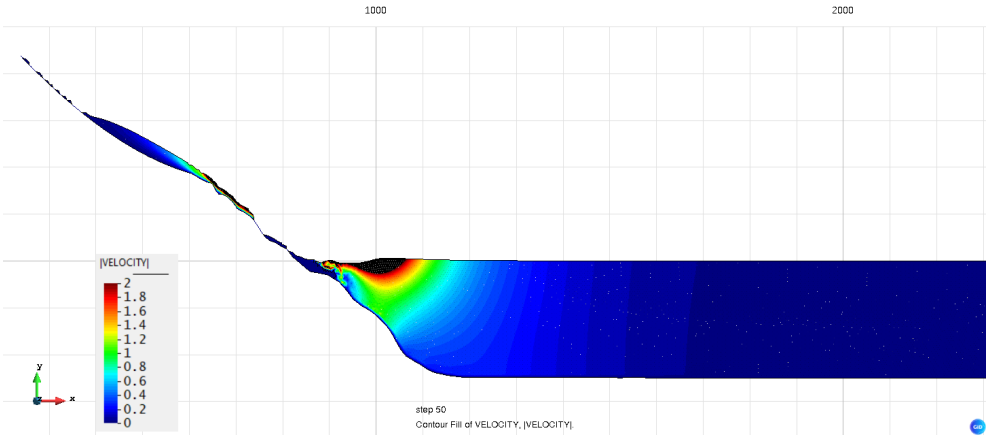

Figure 5.14. Velocity field in absolute value at t = 50 seconds, mesh mu2.

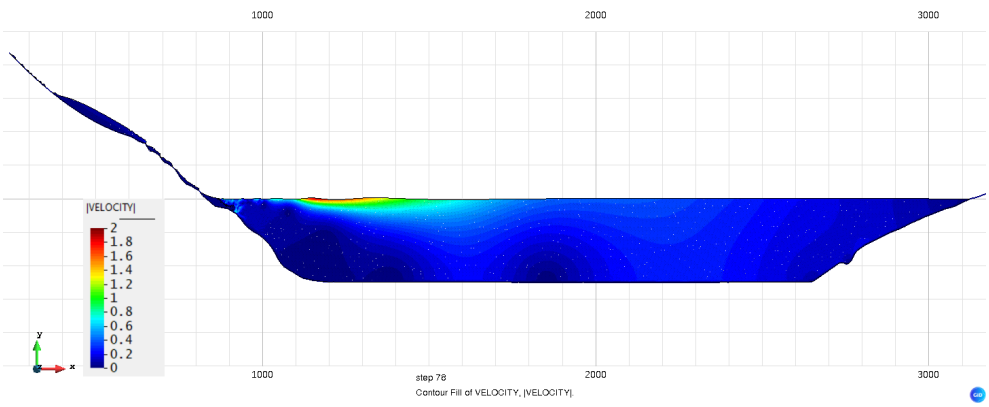

Figure 5.15. Velocity field in absolute value at t = 78 seconds, mesh mu2.

slide to the water, consequent wave generation and its propagation through the reservoir. The analyses also confirm the capabilities of the method in dealing with multi-physics problems and handling complex phenomena, such as landslide large deformations and significant changes of water topology.
The first wave reaches the coast of Monte Isola Island after approximately 78

seconds (the velocity field at this time step is shown in Figure 5.15). Figures 5.16 and 5.17 display the water height time history at different positions (see Figure 5.4). The arrival of the first wave is well captured by all four simulations; however, it is evident that the wave amplitude and period are poorly represented by mesh mu1. The reason is straightforward: the landslide is relatively thin, reaching a maximum thickness of 30 meters, so a six-meter resolution allows for, at most, five elements to describe the landslide vertically. This is insufficient to accurately capture the landslide dynamics and, consequently, the wave propagation.
In contrast, the two mixed meshes (mr1 and mr2) and the higher resolution mesh (mu2) are in good agreement, both in terms of wave period and amplitude. It is also important to highlight that the differences between the three solutions are much smaller than the mesh resolution (5m). Small oscillations, which fade during the first seconds of the simulation, are visible. These are caused by the quasi-incompressible formulation and appear when small time steps are used (in our case, 0.05 seconds).
In terms of computational costs, the simulation performed with mesh mu2, the finest one, took 3 hours and 45 minutes. By using a mixed mesh, we are able to drastically reduce the computational cost while maintaining good accuracy. For instance, the mixed mesh mr1, with only a quarter of the elements compared to mu2, took $\approx$ 23 minutes.

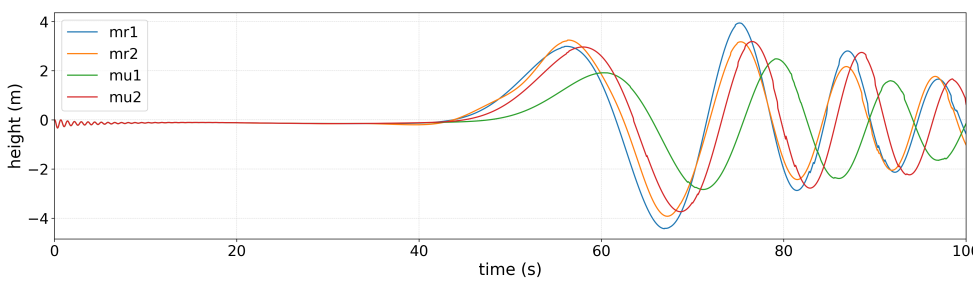

Figure 5.16. Synthetic marigram for tide gauge number 1 - G1 (see Figure 5.4). Different colors represent different mesh resolutions.

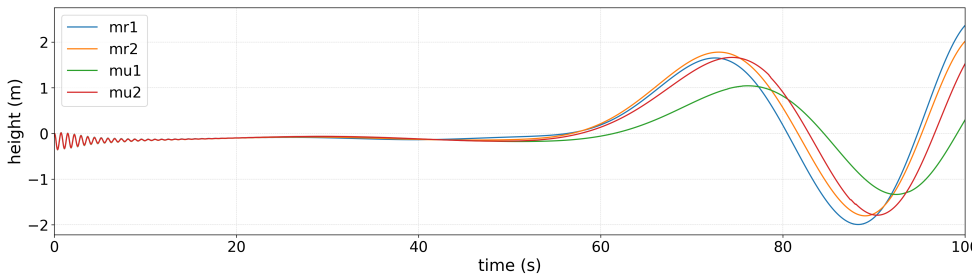

Figure 5.17. Synthetic marigram for tide gauge number 2 - G2 (see Figure 5.4). Different colors represent different mesh resolutions.

Chapter 6

Mud Volcanoes: Salse del Dragone case study

This chapter focuses on the case study of the mud volcano at Salse del Dragone (Monterenzio, Emilia-Romagna, Italy). First, we will introduce the key features and characteristics of mud volcanoes, explaining the processes that lead to their formation.
Next, the field data acquisition campaign will be outlined, this including drone photogrammetry and seismic soil characterization. The main findings of this analysis will be presented and discussed in Section 6.2.
Finally, we will address the questions raised by the in-situ campaign. Specifically, we will perform a stability analysis using both methods discussed in this thesis, namely MLD and SOCP-FEM, to evaluate the slope stability and determine whether the interface identified through seismic characterization could indeed represent the sliding surface of a landslide. To achieve this, we modified the SOCP-FEM code to account for a vertically layered soil. The details, along with the benchmarking process, will be provided in Section 6.3.2.

6.1 Introduction on Mud Volcanoes

Mud volcanoes are geological formations created by the expulsion of gases, typically methane, along with water and fine-grained sediments such as clay, which reach the surface of the Earth or the ocean floor [77], [78], [9].
In Figure 6.1 the global distribution of the main mud volcanoes clusters is shown. They are located onshore in at least 26 countries in Europe, Asia, the Americas and Oceania. Mud volcanoes are widespread in several areas: in

Romania (about 200 structures), in Azerbaijan (178 structures that can reach hundreds of meters in height [79]) and in Italy, where 87 structures have been identified [80], [81], [82].
They can be found in different geological settings like on active continental margins, passive continental shelves or offshore in the open sea. Moreover, the presence of mud volcanoes clusters is a sign of the existence of oil and gas fields at depth [83], [84], [85], since mud volcanoes are situated in areas where hydrocarbons have been, or are, actively being generated.

Figure 6.1. Distribution of the main mud volcanoes clusters, after Mazzini and Etiope (2017) [9]

We can summarize the mud volcanoes formation process in four main steps [86], [87] illustrated in Figure 6.2:

1. *Gravitative instability of shales*: argillaceous sedimentary rocks, known as shale, behave like plastic or ductile materials and rise through overlying, more rigid and dense rock layers, forming structures similar to diapirs (shale diapirism).
2. *Fluid overpressure*: can be due to the generation of hydrocarbons from kerogens in the same unstable shale or in surrounding sedimentary rocks.
3. *Hydrofracturing*: refers to the fracturing of impermeable barriers that allows the pressurised gas-water-sediment motion towards the surface.

It can be due both to the increase of fluid pressure or tectonic stresses, fault reactivation and seismicity.

4. *Fluid flow along permeable fractures*: it is the manifestation of the mud volcano to the surface.

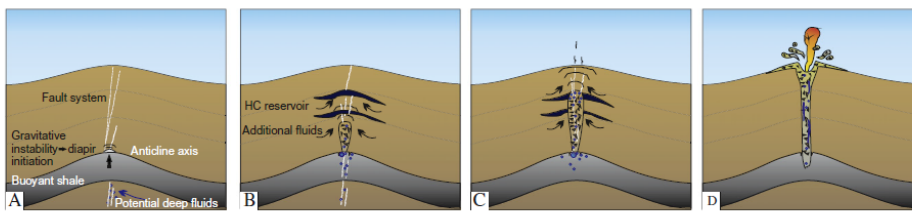

Figure 6.2. Cartoon sketch of a mud volcano growth, from Mazzini and Etiope (2017) [9]. A) Diapir growth with potential deep fluids; B) Potential additional fluids cause overpressure while diapiric growth leads to brecciation; C) The diapir, overpressured, reaches a critical depth: the system is ready for triggering; D) Fluidized gas-saturated sediments can now reach the surface.

Mud volcanoes morphology is quite variable: they can have an areal extension that varies from some m^2 up to several km^2. While some have the characteristic cone shape, a variety of other forms are also present: pointed cones, flattened or plateau-like structures, domes, as well as depressions and calderas. In most cases, however, they are composites, consisting of several craters with diverse shapes. They can be classified on the basis of their activity state [88]:

Eruptive: mud volcanoes in this regime can erupt mud breccia up to tens of meters in height. Usually eruptions last for few days or less.

Dormant: the majority of mud volcanoes in the world are currently in this state. This quiescent state is characterized only by gas and water seepage (i.e. bubbling pools, salsas).

Extinct: no evidence of activity, at least in historic records. Weak seepage can be present.

Fossil: paleo mud volcanoes, ancient buried structures identified by acoustic or drilling techniques [89], [90].

6.2 Field Data Acquisition Campaign

The mud volcano considered in our analysis is Salse del Dragone, a structure situated between the cities of Bologna and Imola, in Emilia-Romagna region (Italy), as shown in Figure 6.3.

Figure 6.3. Location of the study site (pink triangle), with a zoomed-in view of the area.

As previously mentioned, these mud volcanoes originate from the presence of methane and oil pockets deep underground, which are always accompanied by fossil seawater. As the water rises due to internal reservoir pressure, it mixes with clays, forming salty muds of varying density. In the case of the Dragone mud volcanoes, the materials they pass through are known as Scaly Clays. The name "Dragone," meaning "The Dragon," comes from the fact that their activity was reportedly much more vigorous in the past (the 1800s), with eruptions reaching tens of meters, as recorded by the mineralogist Luigi Bombicci [91], [92]. At the present state, the volcano is considered in its dormant phase.
The area affected by the volcano and the associated mud flow covers approximately 1500 m^2 (Figures 6.4, 6.5). It consists of a mud plateau of about 200 m^2, surrounded by recent mud flow deposits. On this plateau, the main crater and several smaller secondary cones are clearly visible during the spring and summer months, as depicted in Figures 6.6 and 6.7. However, during the winter or in very humid and rainy periods, the mud plateau turns into a pool of liquid mud, making it difficult to access.
The selection of this site for stability analysis is motivated by two key factors: first, visual inspections and regional geological maps indicate the possible presence of a landslide body. Secondly, there is a notable absence of stability studies on the Salse del Dragone mud volcano in the literature, with the exception of geochemical investigations, such as those focused on fluid migration [93].

The field data acquisition campaign was conducted during 2023/2024, with multiple visits to perform various types of measurements and refine our analysis. Field survey were carried out in winter, summer and spring.
In particular, we used the following techniques:

1. *Structure from Motion (SfM) Photogrammetry*: conducted with the"Matrice 350 RTK" Unmanned Aerial Vehicle (UAV) equipped with a "DJI Zenmuse P1" camera, thanks to the contributions of Dr. Arianna Pesci and Dr. Giancarlo Tamburello from INGV – Bologna. The results of this analysis provided us with a DSM (Digital Surface Model) to better characterize the study area and helped us in the georeferencing phase of field data acquisition.

Figure 6.4. Location of Salse del Dragone mud volcano. In red, the mud plateau, while the yellow polygon indicates the recent mud flow depositions.

Figure 6.5. Zoom the Salse del Dragone main crater.

2. *Seismic Single Stations*: carried out using the TROMINO ® instrument, with the help and supervision of Dr. Enrico Paolucci, University of Bologna.
3. *Seismic arrays*: conducted using arrays of vertical geophones, also with the help and supervision of Dr. Enrico Paolucci, University of Bologna. These last two techniques were used to seismically characterize the soil in terms of vertical layering.

Details about the techniques and their results will be provided in the following Sections.

Figure 6.6. One of the craters at Salse del Dragone during a mud and gas seepage.

Figure 6.7. Zoom of one of the Salse del Dragone craters.

6.2.1 Structure from Motion (SfM) Photogrammetry

The photogrammetric analysis consists of transforming a set of images of an object into a 3D realistic model. Each image, considered the projection of the object onto a plane, represents reality from a specific view and distance. All images have to be "aligned", that is, linked to each other by knowing their position of the center and orientation in a common space. This issue runs using homologous points, that is pixels representing the same part of the object belonging to partially overlapped images. Finally, the photogrammetric equations system is solved using least squares methods transforming images-pixels in 3D coordinates into the same common reference frame.
Structure from Motion (SfM) Photogrammetry is an innovative high performance, low-cost, and user-friendly remote-sensing technique [94], [95], [96]. Through SfM it is possible to generate dense and accurate 3D models using a sequence of digital images that can be captured with complete freedom, without relying on complex or costly camera orientation systems. This technique is widely used for its versatility both in topographic/geomorphological fields [97] and architectural applications [98].
The basic principles behind this technique are the same of traditional photogrammetry, i.e. collinearity equations and epipolar geometry, but it differs from it by two major innovations [96]:

- application of the SIFT (scale-invariant feature transform) algorithm [99]. This method converts an image into a set of local feature vectors that remain unaffected by shifts, scaling, and rotation. Additionally, it shows partial resistance to variations in lighting and affine or 3D transformations.
- usage of the RANSAC (RAndom Sample Consensus) technique [100]. This technique excels at processing and refining data that includes a substantial amount of outliers, making it an ideal choice for automated image analysis tasks, where the interpretation relies on data from feature detectors that are prone to inaccuracies.

SIFT is used to detect and describe feature points in each image, which are then matched across multiple images. These matches are crucial for calculating the relative positions of the cameras and reconstructing the 3D structure of the scene. However, not all matches generated by SIFT are accurate, which is where RANSAC plays a vital role. RANSAC filters out incorrect matches and

ensures a robust estimation of camera motion and scene geometry. Specifically, it identifies and removes outliers during the estimation of essential matrices, homographies, or fundamental matrices, all of which are key to determining the relative positions and orientations of cameras in SfM.
These procedures automatically look for and check correspondences between digital images; therefore, the survey of the areas of interest has to be carried out in a short time to avoid undesirable effects caused by the apparent motion of the Sun. The movement does not only change the brightness of the images, which will vary with the time of day at which the survey is carried out, but it also affects shadows that can change the apparent form of the surfaces by creating patterns of very diverse shapes and colors. Such unwanted effects eventually lead to the failure of automatic image alignment [101]. The results of the SfM technique consist in a 3D point cloud, dense and photo realistic, from which a 3D digital model can be retrieved. It is important to highlight that the point cloud requires a scale factor to accurately represent a real object in a metric system, even when GNSS data for the camera position are available in real-time (like in the present case study). This factor can be applied either during image alignment, before generating the point cloud, or afterward, using the photogrammetry software or a different tool [102].
The tools used for this survey are the "Matrice 350 RTK" UAV (shown in Figure 6.8) equipped with a "DJI Zenmuse P1" camera. The camera and drone specifics are reported in Table 6.1.

Figure 6.8. Dr. Giancarlo Tamburello preparing the UAV for the flight.

Table 6.1. Camera and UAV specifics.

Camera	DJI Zenmuse P1
Focal length (mm)	35
Aperture (f-stop)	f/2.8 - f/16
Sensor number of pixel	8192 × 5460
Sensor size (mm × mm)	35.9 × 24
Pixel size (mm)	0.0044
UAV	**Matrice 350 RTK**
Dimensions–unfolded (mm)	810 × 670 × 430 (L × W × H)
Weight (with lower single gimbal) (kg)	Approx. 6.47 (with 2 TB65 batteries)
Max Horizontal Speed (m/s)	23 m/s
Max Flight Time	Up to 55 minutes (no payload, with TB65 batteries)
Max Wind Resistance (m/s)	12
Max Flight Altitude (m)	7000
Supported Gimbals	Zenmuse H20, H20T, H20N, P1, L1
GNSS Systems	GPS + GLONASS + BeiDou + Galileo
RTK Positioning Accuracy	Horizontal: 5 cm + 1 ppm; Vertical: 5 cm + 1 ppm
Operating Temperature Range	-20°C to 50°C
Battery Model	TB65 (5880 mAh, 44.76 V)

The UAV performed two flights, both with a mean flight altitude of 114 meters, targeting a 1.35 cm ground pixel size. The drone trajectory was chosen in order to guarantee a high level of overlapping images (i.e. 70%), allowing a good photogrammetric reconstruction of the scene. The specifics of the flights and the collected data are summarized in Table 6.2.

The data collected on field were then post-processed by Dr. Arianna Pesci (INGV) by means of Agisoft Metashape Software [103]. The point cloud obtained, consisting of approximately 63 million coordinates from the analysis, was enhanced by the image overlap, ensuring that each area of the region was covered by at least 10 images. The results of this analysis are shown in Figures 6.9, 6.10, 6.11 and 6.12.

Table 6.2. UAV flights specifics.

Mean flight altitude (m)	114
Total area covered (km^2)	0.11
Number of collected images	167
Ground Resolution (cm/pixel)	1.35
Number of homologous point	138180

The preliminary SfM analysis highlights important variations in elevation and slope morphology. Relative heights, measured from a horizontal plane at the base of the slope, vary between 0 and 60 meters (Figure 6.9), providing valuable insight into the vertical displacement and overall terrain characteristics. Additionally, localized morphological features were identified by comparing distances from a fitted plane in three macro-areas, revealing minor undulations ranging from -4 to 6 meters (Figure 6.10). This level of detail is crucial for detecting potential areas of instability within the slope. Moreover, as we can see in Figure 6.11, on a larger scale, a single fitted plane across the entire area showed variations between -12 and 7 meters, offering an understanding of the broader geomorphological trends.
Figure 6.12 shows areas with suspicious morphologies outside the main slope zone. This kind of features can suggest the presence of old mud volcanoes. Alternatively, these formations could be natural depressions. Further analysis will be required to distinguish between these possibilities, as the presence of ancient mud volcanoes could imply deeper tectonic or geothermal processes, while natural depressions may simply reflect erosional or sedimentary processes.

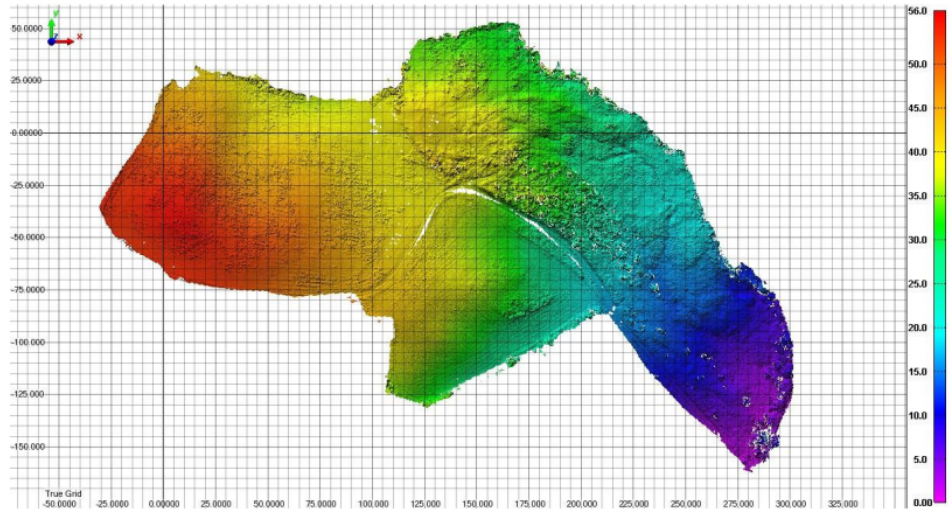

Figure 6.9. Relative heights with respect to the horizontal plane passing through the foot of the slope (measured at the lowest point).

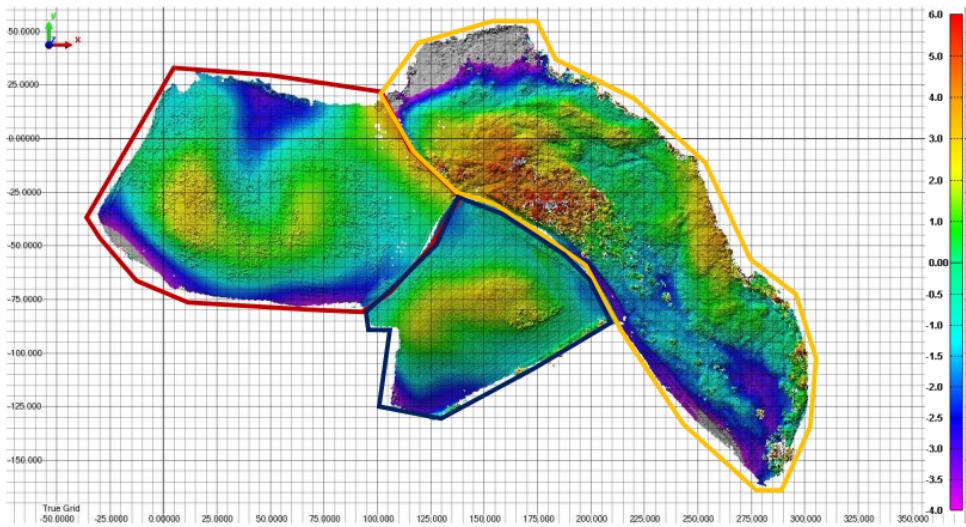

Figure 6.10. Relative morphologies with three different fitted planes.

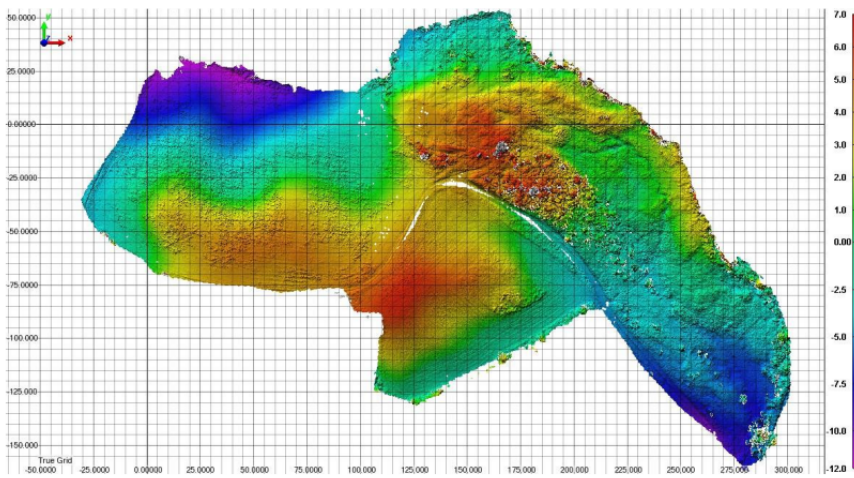

Figure 6.11. Relative morphologies with a single fitted plane for the entire surveyed area.

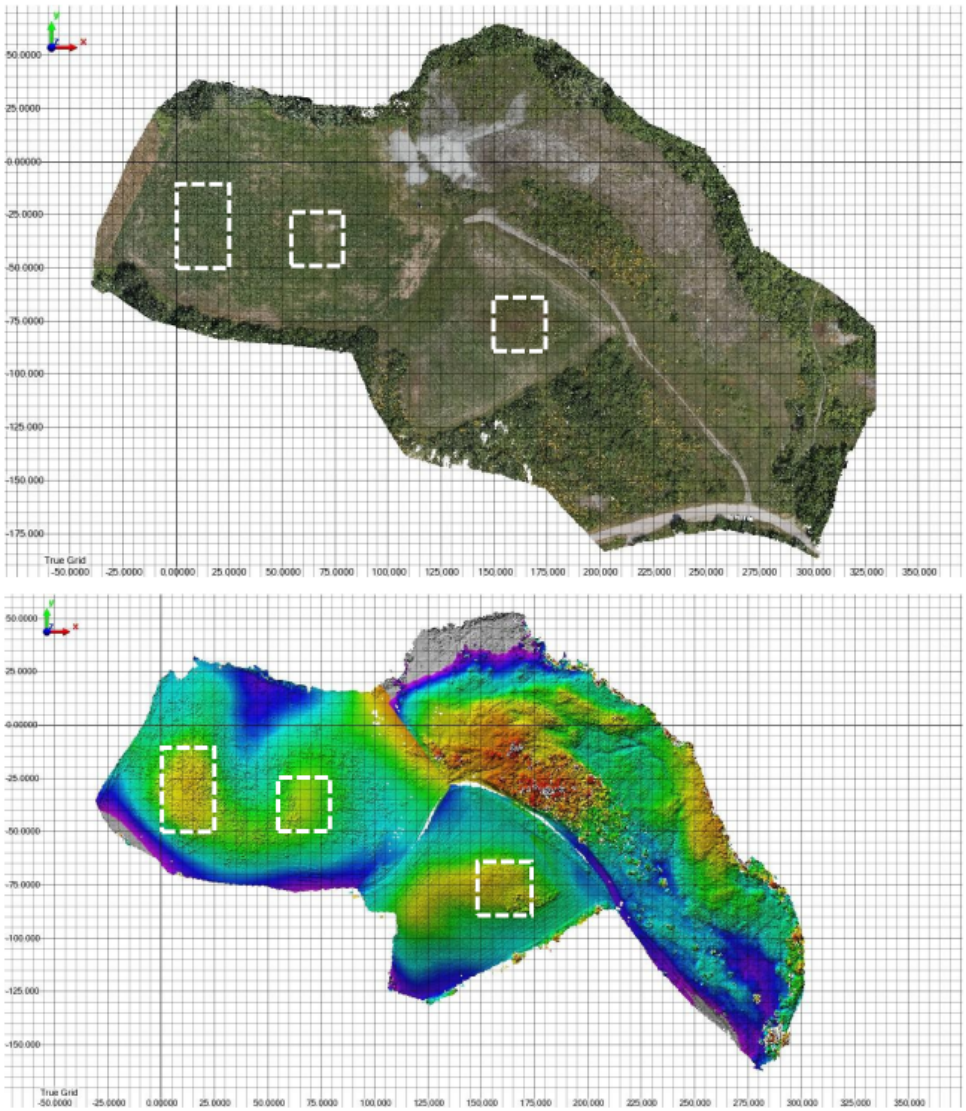

Figure 6.12. Identification of areas with suspicious morphologies outside the study area, where large vents and significant clay deposits are present. These could be ancient mud volcanoes or simply natural depressions.

6.2.2 Seismic Characterization

One of the main challenges in conducting a stability analysis on a previously unstudied site is determining the vertical soil layering and its geotechnical parameters. In simple cases (soft layers overlying a rigid seismic bedrock), it is possible to establish a relationship between the thickness h of the soft layer, the average S-wave velocity within it (V_s), and the fundamental resonance frequency f of the layer. The relationship is the following [104], [105]:

$$f = \frac{V_s}{4h} \tag{6.1}$$

Therefore, by knowing the mean velocity of shear waves V_s and the fundamental resonance frequency f of the layer we are able to determine the layer thickness.
This information can be obtained through both laboratory measurements conducted on samples collected from drillings, as well as from "in situ" measurements using appropriate seismic prospecting techniques. In particular, we used both active and passive seismic techniques.

Active Seismic Prospections

The most commonly used active prospecting technique today is MASW (Multichannel Analysis of Surface Waves) [106]. It is a non-invasive investigation technique that allows the definition of the vertical shear wave velocity profile (V_s), based on the measurement of surface waves made at various sensors placed on the ground surface. Commonly the sensors are vertical geophones, and care must be taken when placing them to ensure good contact with the ground. The layout of the acquisition is based on a linear array of receivers [107]:

- *The array length* should be at least equal to the maximum desired wavelength, which roughly corresponds to twice the desired investigation depth.
- *The spacing between receivers* should be sufficient to accurately capture the short wavelengths associated with the propagation of high-frequency waves (usually between 0.5 and 4 meters).

- *The seismic source*: the most common and affordable source is a sledgehammer striking a metal plate or directly the surface of the ground. Source activations on either side of the array are usually suggested.

In order to extract the shear wave velocity (V_s) dispersion curve, various analysis methods can be used (e.g. frequency-wavenumber analysis [108], [109]). In our case the raw data post processing was performed using the MASWaves Software [110]. The main steps of the post-processing analysis can be summarized as follows:

1. Extraction of the dispersion curve using the phase shift method. This method analyze the phase delay between seismic signals recorded by sensors placed at different locations along the array and uses it to calculate the speed at which the waves travel at specific frequencies.
2. Data inversion to compute the shear wave velocity (V_s) profile.

Passive Seismic Prospections

Passive surface wave techniques have become dominant over the last decade in investigating the Earth's structure. These techniques rely on the analysis of the background seismic noise: in the absence of seismic events, the Earth's surface is constantly affected by small vibrations characterized by amplitudes on the order of 10^{-4} to 10^{-2} mm. These ambient vibrations are generated by multiple sources [111], [112], [113] which can be summarized as follows:

- frequencies < 0.5 Hz – natural sources;
- frequencies between 0.5 and 1 Hz – natural and anthropic sources;
- frequencies > 1 Hz – anthropic sources.

The stochastic nature of this phenomenon enables the complexity of the analysis to be reduced through statistical methods. For instance, in the case of an isotropic wavefield—where sources are distributed in a statistically homogeneous manner around the measurement site — the structure of the signal can be considered statistically independent of the sources' nature and position, being mainly influenced by the soil structure. Therefore, the structure of the signal recorded at the surface can provide information about the medium

through which the waves have traveled [114].
Passive techniques can be divided in two main categories:

1. *Seismic arrays*, i.e. multi-station configurations: the ambient vibration field is recorded using a group of synchronized sensors placed in the study area in specific 2D patterns, either linear or random. Typically, only the vertical component of ground motion is measured. The goal of this technique is to extract the shear wave velocity (V_s) dispersion curve.
2. *Single station acquisition*: ambient vibrations are recorded using a three-component sensor and analyzed with the Horizontal to Vertical Spectral Ratio (HVSR) (H/V) technique [115]. This method aims to directly estimate the soil's fundamental resonance frequency by calculating the spectral ratio between the horizontal (H) and vertical (V) components of ground motion.

In our study the data collected on the field with passive seismic arrays where analyzed with two different techniques, one based on Extended Spatial Auto-Correlation (ESAC) analysis [116], [117] and one on the frequency-wavenumber (f-k) analysis. In the latter case, the Beam-Forming method (BFM) [108] was specifically considered.

Before describing the protocol used for the analysis of single seismic stations, it is important to briefly outline the criteria for classifying the acquired data. These criteria were used for an initial assessment to distinguish between reliable and unreliable measurements, as well as to identify doubtful results that require closer inspection.
In our study we used the classification scheme developed by Albarello et al. [118], which divides the measures in three classes:

class A: a reliable and interpretable HVSR curve, serving as a reference measurement, can independently be considered representative of the dynamic behavior of the subsoil at the site in question.
To fall in this class the measurement should satisfy six requirements: stationarity, isotropy, absence of artifacts, physical plausibility, statistical robustness and having a representative sampling.

class B: suspicious HVSR curve, which should be used cautiously and only if it aligns with other measurements taken in the surrounding area.

The measure belongs to this class if one or more of the six requirements of class A are not satisfied.

class C: bad HVSR curve (difficult to interpret), which should be discarded.
Class B measurements are reclassified as Class C if they exhibit a rising drift from low to high frequencies or show signs of electromagnetic or industrial disturbances.

Moreover, for each class two other sub-classes (type) were introduced:

type 1: the HVSR curve presents at least one clear peak in the frequency range of interest;

type 2: the HVSR curve does not present any clear peak in the frequency range of interest.

In the present study all the data retrieved by single seismic stations were analyzed using the strategy developed by Picozzi et al. [13], which can be summarized as follows:

1. The recording is divided into 20 to 60 second windows, ensuring good spectral resolution, each analyzed separately. A total recording duration of around 20 minutes is typically sufficient for statistical stabilization of the signal.
2. For each window and for all three ground motion components, the following analyses are performed:
   - Linear trend removal (detrending) and tapering of signal ends using a Hann cosine function to avoid leakage;
   - Spectral amplitude computation via Fast Fourier Transform [119];
   - Smoothing of spectra with a triangular moving window, with a frequency-dependent half-width (5% of the central frequency), to prevent spurious peaks and irregularities in the H/V curve [13].
3. The geometric mean of the spectral amplitudes of the two horizontal components is calculated, and the H/V curves for each time window are obtained by taking the spectral ratio between this mean and the vertical component's spectral amplitude.

4. The final H/V function and its corresponding 95% confidence interval are obtained by averaging the H/V ratios from each time window, identifying the frequency at which the H/V ratio reaches its maximum (resonance frequency f).

Data Acquisition and Results

During the various field campaigns conducted for the characterisation of the Salse del Dragone mud volcano area we were able to apply both active and passive seismic techniques. The investigated site is shown in Figure 6.13 and covers a total area of $\approx 15000\ m^2$.
The following arrays were deployed:

- 4 seismic arrays for passive measurements, consisting of 16 vertical geophones arranged in an L-shaped layout (see Figure 6.13). The acquisition duration ranged from 30 to 40 minutes.
- 4 seismic arrays for MASW, using a linear layout of 10 or 16 vertical geophones. In some cases, one branch of the passive arrays was also used for the MASW layout. The seismic source used was a sledgehammer striking a metal plate.

Additionally we performed 47 single station measurements for a time length of 20 minutes. We then proceeded to classify it according to the aforementioned guidelines [13]. The results of the visual inspection of HVSR spectra and their classification is reported in Table 6.3. Of the 47 measurements taken, none could be classified as reliable on their own (i.e., Class A), and 7 had to be discarded (Class C). The explanation is simple: the Salse del Dragone site becomes extremely muddy during the rainy season, and some of these recordings were conducted in winter, under windy and rainy conditions. The influence of the wind on the equipment, combined with the instability of the loose soil, likely caused the instruments to shift during some of the recordings.

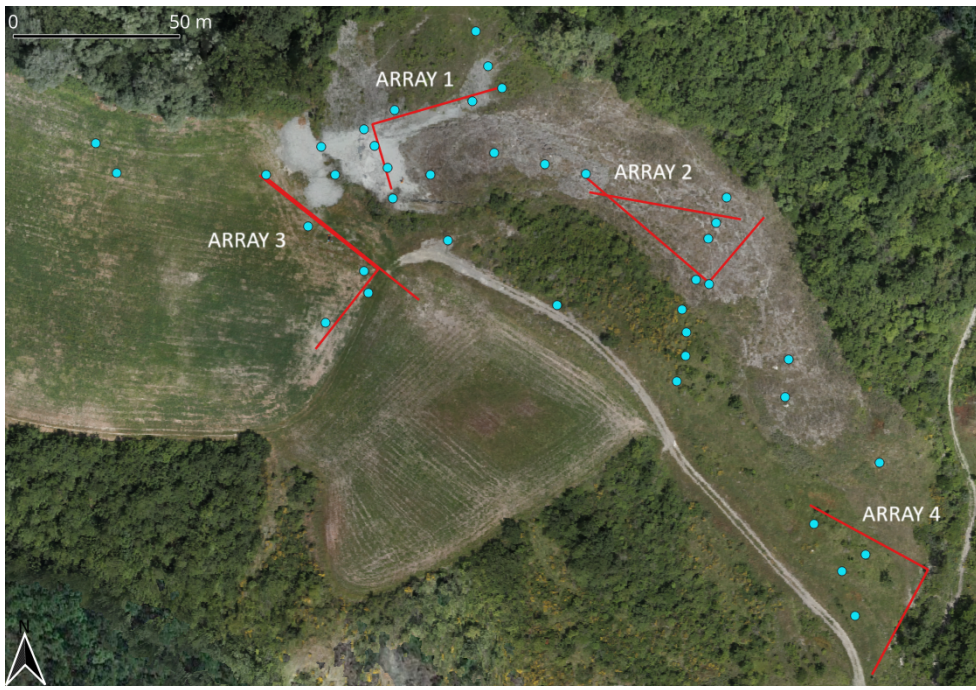

Figure 6.13. Salse del Dragone site: blue dots represent the 40 single station used for the analysis (the Class C measurements are not included). Red lines indicate the seismic arrays positions.

Table 6.3. HVSR measures and their classification. F0, A0, F1, A1 represent the frequency (Hz) and amplitude (dimensionless, as it is the ratio between the horizontal and vertical components) of the identified spectral peaks. Fr and Ar are the frequency and amplitude of the peaks considered representative, specifically those with higher amplitude and/or clearer definition. Class and Type features refers to the study of Picozzi et al. [13].

Name	F0	A0	F1	A1	Fr	Ar	Class	Type
E001	0.85	3.5	–	–	0.85	3.5	B	2
E002	3.50	2.0	36.88	3.5	3.50	2.0	B	1
E003	3.50	2.8	22.72	3.2	3.50	2.8	B	2
E004	3.00	4.5	5.00	3.2	3.00	4.5	B	1
E005	3.13	2.5	–	–	3.13	2.5	B	1

E006	3.03	2.5	–	–	3.03	2.5	B	1
E007	3.66	5.2	–	–	3.66	5.2	B	1
E008	3.00	2.9	–	–	3.00	2.9	B	1
E009	2.20	3.0	–	–	2.20	3.0	B	1
E010	3.00	2.0	–	–	3.00	2.0	B	1
E011	2.80	1.9	7.00	2.0	12.88	2.5	B	2
E012	3.13	2.8	–	–	3.13	2.8	B	1
E013	4.60	5.0	–	–	4.60	5.0	B	1
E014	11.40	2.5	–	–	11.40	2.5	B	2
E015	1.53	2.0	–	–	1.53	2.0	B	2
E016	3.10	4.0	–	–	3.10	4.0	B	2
E017	3.25	3.2	5.40	3.0	3.25	3.2	B	2
E018	1.20	1.8	–	–	1.20	1.8	B	2
E019	–	–	–	–	–	–	C	–
E020	–	–	–	–	–	–	C	–
E021	–	–	–	–	–	–	C	–
E022	1.2	1.9	2	2.2	1.2	1.9	B	2
E023	0	0	–	–	0	0	B	2
E024	12	2.1	–	–	12	2.1	B	1
M001	1.25	2.8	–	–	1.25	2.8	B	2
M002	2.25	2	–	–	2.25	2	B	1
M003	0	0	–	–	0	0	B	2
M004	–	–	–	–	–	–	C	–
M005	9	3	–	–	9	3	B	1
M006	10	4.2	16	5.3	10	4.2	B	1
M007	16	4	30	4.8	16	4	B	2
M008	15.00	3.5	–	–	15.00	3.5	B	1
M009	3.30	3.5	4.90	2.8	3.30	3.5	B	1
M010	3.23	2.7	4.50	2.2	3.23	2.7	B	2
M011	3.40	4.2	4.70	4.1	3.40	4.2	B	1
M012	4.00	2.8	–	–	4.00	2.8	B	1
M013	12.00	4.5	–	–	12.00	4.5	B	1
M014	0.20	2.8	–	–	0.20	2.8	B	2
M015	3.00	2.5	–	–	3.00	2.5	B	1
M016	1.00	2.0	2.50	2.1	1.00	2.0	B	2
M017	–	–	–	–	–	–	C	–
M018	1.50	2.0	3.00	3.0	1.50	2.0	B	1

M019	1.50	2.5	3.00	3.9	1.50	2.5	B	2
M020	–	–	–	–	–	–	C	–
M021	–	–	–	–	–	–	C	–
M022	1.20	1.7	–	–	1.20	1.7	B	2
M023	0.00	0.0	–	–	0.00	0.0	B	2

The results of the joint inversion analysis using both passive and active techniques, performed following the procedure described by [118], are reported in Figures 6.14 and 6.15. The results refer to Array 1 and Array 2 (see Figure 6.13), because those are the ones located in the area of interest for the slope stability analysis.

The inversion analysis reveals a clear impedance contrast at a depth of 10 meters, observed both in Array 1 and Array 2. This detected interface can be attributed either to a sliding surface (indicating the presence of a landslide) or to the accumulation of different material resulting from volcanic activity. To address this, we conducted the stability analysis described in the following section.
Additionally, we also note a contrast around 30-35 meters, which could indicate a transition to a harder soil layer; however, it seems unlikely to represent a sliding surface.

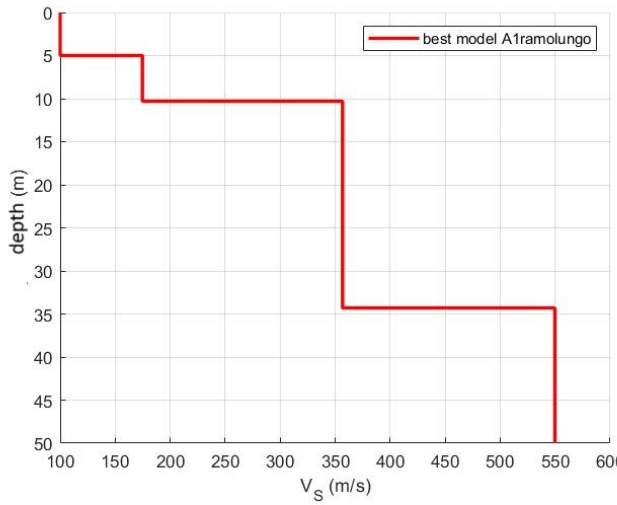

Figure 6.14. Surface wave profile for Array 1.

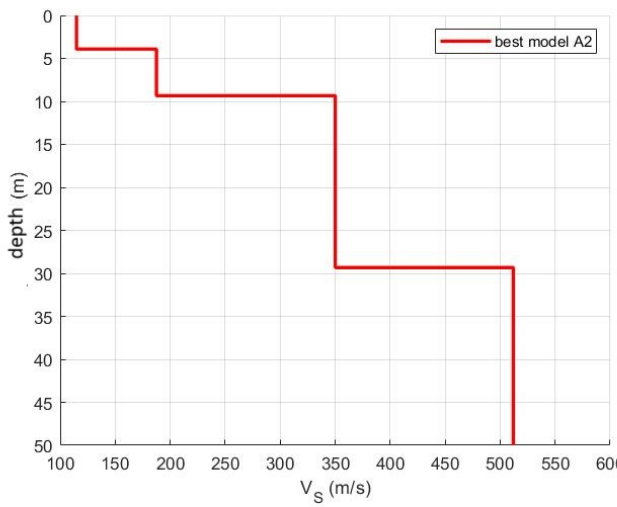

Figure 6.15. Surface wave profile for Array 2.

6.3 Stability Analysis

This section will deal with the application of the two stability methods presented in Chapter 2. From the analysis of the Seismic Arrays and the HVSR measures we can make some important assumptions regarding the layering of the slope. In particular we identified an impedance contrast at 10 meters depth, implying that our slope is constituted by at least two layers with different geotechnical parameters.
The first issue to solve was to retrieve some plausible geotechnical parameters for the two layers. In order to do so we consulted the geological and geomorphological technical report of Emilia-Romagna region [14], which describes the geotechnical features of an area morphologically similar to the Salse del Dragone site. Additionally, Professor Marco Antonellini – BIGEA University of Bologna, helped us in this task: he collected some samples from the main crater area in order to determine the density of the surface material (Figures 6.16 and 6.17).

The geotechnical parameters derived from the report [14] are partly retrieved from laboratory tests performed on two samples collected during the survey, and partly from data obtained from investigations conducted in nearby areas characterized by the presence of the same lithotypes. In particular, for brown-grey silty clay with inclusions and for very compact grey silty clay they suggest the parameters reported in Table 6.4.

Table 6.4. Geotechnical parameters retrieved from the geotechnical report of Emilia-Romagna region [14].

Type of Material	Density (kN/m^3)	Cohesion (kPa)	Friction Angle (°)
Very compact grey silty clay	20	21.5	21
Brown-grey silty clay	18.5	18	21

Given that the site under examination has characteristics that are certainly different from those studied in the technical report, due to the presence of a mud volcano, we adopted the following strategy to reduce the uncertainties involved: starting from the parameters in Table 6.4, we created 4 dif-

Figure 6.16. Professor Marco Antonellini retrieving mud samples from the crater area.

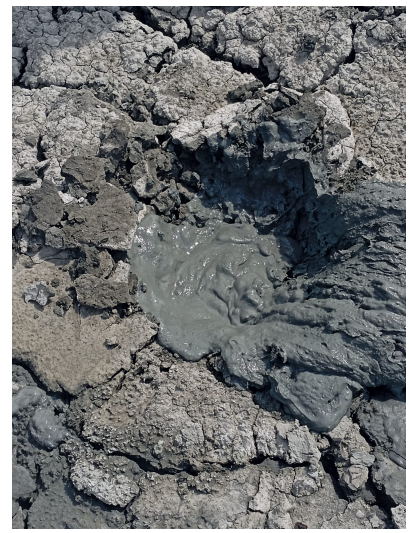

Figure 6.17. Zoom of the drilled hole for sample acquisitions.

ferent cases, keeping the geotechnical parameters of the deepest layer (below 10 meters) fixed, and varying those of the surface layer. Specifically, we reduced the density, cohesion, and friction angle of the surface layer until we found a combination that caused its instability. We then proceeded with geological/geotechnical considerations to assess the plausibility of this scenario. Additionally, thanks to Professor Antonellini, we created a fifth case, again keeping the parameters of the lower layer fixed and considering the upper layer as if it were entirely composed of the crater's mud. For this fifth scenario, the density value obtained from laboratory analysis was used. As for the friction angle, we considered that the Ligurian (varicolored) clays present at the Salse del Dragone contain many inclusions of limestone and sandstone, which can increase the internal friction angle by up to 5 degrees at the most. The cohesion value was instead obtained from the GEOSTRU database [120].
The resulting five cases are reported in Table 6.5. From this point onward, Layer 1 will refer to the upper layer, and Layer 2 to the lower layer.

Table 6.5. Geotechnical parameters for the five cases considered.

	Case 1	Case 2	Case 3	Case 4	Case 5
Layer 1	γ_1= 18.5 kN/m^3 ϕ_1=21° c_1=18 kPa	γ_1= 16 kN/m^3 ϕ_1=18° c_1=10 kPa	γ_1= 13 kN/m^3 ϕ_1=16° c_1=4 kPa	γ_1= 10 kN/m^3 ϕ_1=10° c_1=3 kPa	γ_1= 15 kN/m^3 ϕ_1=5° c_1=5 kPa
Layer 2	γ_2= 20 kN/m^3 ϕ_2=21° c_2= 21.5 kPa	γ_2= 20 kN/m^3 ϕ_2=21° c_2= 21.5 kPa	γ_2= 20 kN/m^3 ϕ_2=21° c_2= 21.5 kPa	γ_2= 20 kN/m^3 ϕ_2=21° c_2= 21.5 kPa	γ_2= 20 kN/m^3 ϕ_2=21° c_2= 21.5 kPa

The second uncertainty we must address is the choice of the profile for the stability analysis. As already mentioned, SOCP-FEM and MLD deal with 2D problems, but aside from the vertical layering, there is also a horizontal variation to consider. To overcome this challenge, we performed the stability analysis along 7 different profiles, carefully following the maximum slope gradient. Specifically, we selected:

- 2 profiles that cut through the crater area and extend southeast (profile 3 and 6 in the Figure 6.18);
- 4 profiles that run from northwest to southeast and cross what, based on in-situ geological observations, appears to be the most likely landslide area (profiles 1, 2, 4 and 5 in Figure 6.18);
- a polyline that includes both the crater area and the probable landslide zone, shown in Figure 6.19.

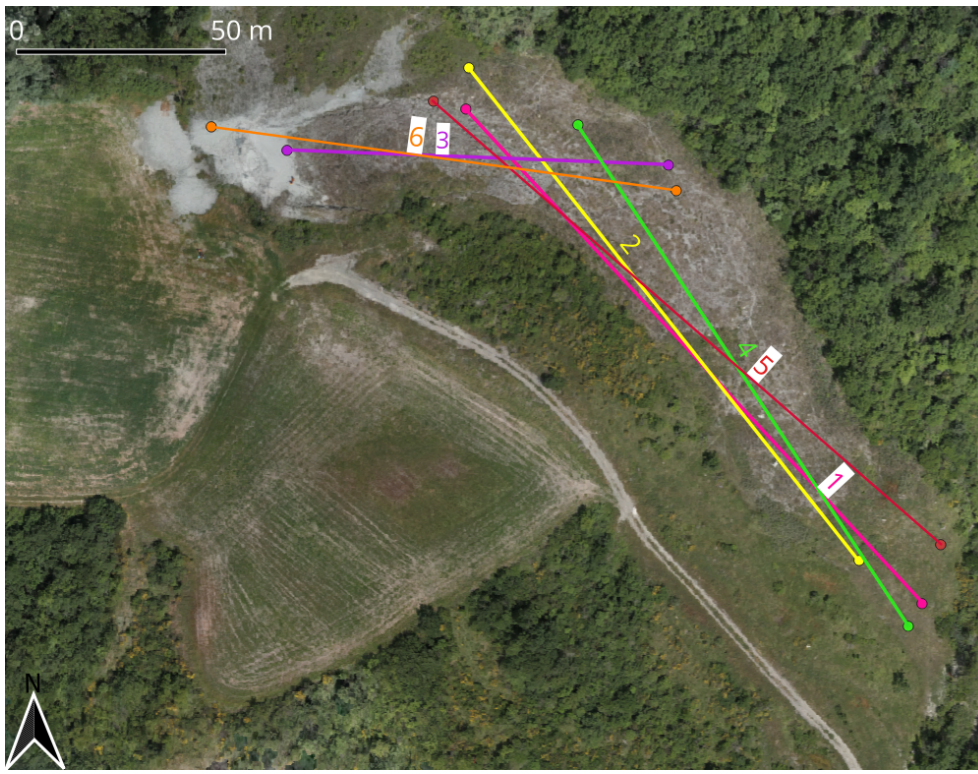

Figure 6.18. Six straight profiles selected for the stability analysis.

Figure 6.19. Polyline used in the stability analysis.

6.3.1 MLD application

The first analysis presented is the one performed using the MLD method. As already pointed out, this method needs as input data the geometry of the sliding surface, as well as the topographic profile and the geotechnical parameters.
The only information available to us for determining the slip surface comes from the seismic characterization of the ground presented in Section 6.2.2. The layer at a depth of 10 meters could indeed correspond to a slip surface, but this could also be more superficial (if it is indeed a landslide). To overcome this uncertainty, we have decided to use both approaches supported by the MLD software:

- for each of the 6 straight profiles, we selected two arcs of a circumference at different depths as slip surfaces;
- for the polyline, we created two cases: in one, positioning the slip surface exactly at a depth of 10 meters with a specifically designed profile (Figure 6.24); in the other, the surface is at a depth of 2 meters (Figure 6.25).

Figures 6.20 and 6.21 show the two arcs of circle selected as sliding surfaces for profile 1. In the first case, the maximum depth of the surface is approximately 5 meters, while, in the second case, the surface reaches a depth of approximately 8 meters.
Figures 6.22 and 6.23 illustrates to profile 3. In this case, as shown, we also attempted to vary the location of the sliding surfaces, making them more prone to instability (Figure 6.23 shows a steeper inclination of the sliding surface). These two surfaces, in particular, reach depths of approximately 4 meters and 6 meters, respectively. In general, we attempted to vary the depth, reaching up to 10 meters where the profile geometry allowed it, and, overall, covering the entire profile, at least for those oriented northwest-southeast.
Table 6.6 presents the results of the stability analysis, along with the details of the geometry of all configurations. As shown, the FoS for each case studied are always greater than one, except for Case 5, where 5 profiles become unstable (highlighted in yellow in the table) and 3 others approach instability (with FoS between 1 and 1.1). It is also not possible to establish a clear connection between the depth of the potential sliding surface and the landslide, as the configuration with the deeper (or shallower) surface does not necessarily result in a more unstable case. What matters most is the position and chosen geom-

etry: for instance, in the case of profile 3, the surfaces are at similar depths, yet the steepest one is clearly the most unstable.

From these results, we can already deduce that the slope is generally stable, and instability, leading to potential landslide triggering, is likely only under particularly unfavorable and improbable conditions (such as an entire layer composed of mud from the mud volcano, as hypothesized for the geotechnical parameters of Case 5).

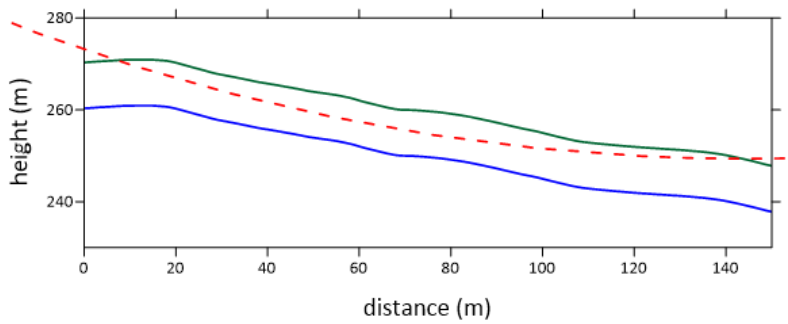

Figure 6.20. First configuration for profile 1. The blue line represents the 10 meter interface while the green line is the topographic profile. The red dashed curve is the selected sliding surface.

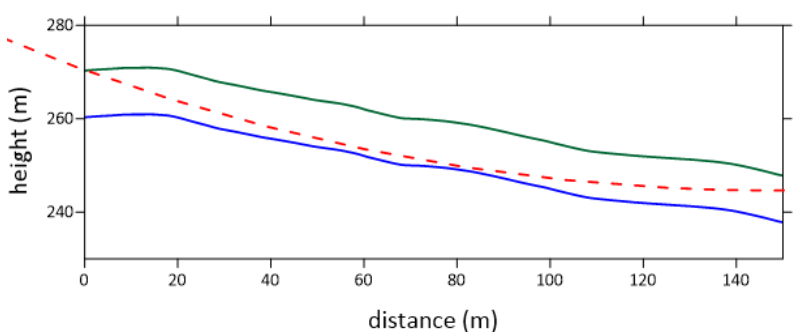

Figure 6.21. Second configuration for profile 1. The blue line represents the 10 meter interface while the green line is the topographic profile. The red dashed curve is the selected sliding surface.

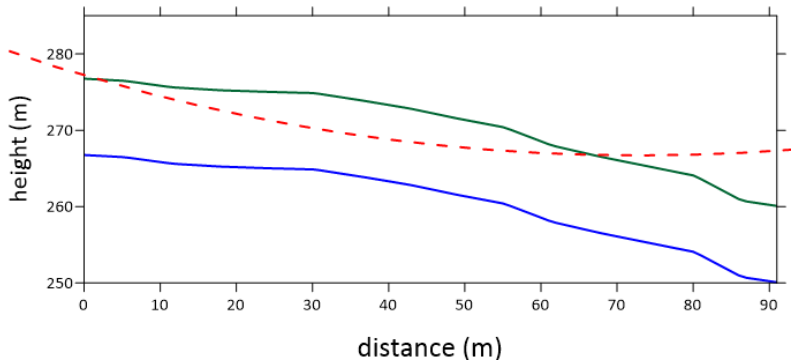

Figure 6.22. First configuration for profile 3. The blue line represents the 10 meter interface while the green line is the topographic profile. The red dashed curve is the selected sliding surface.

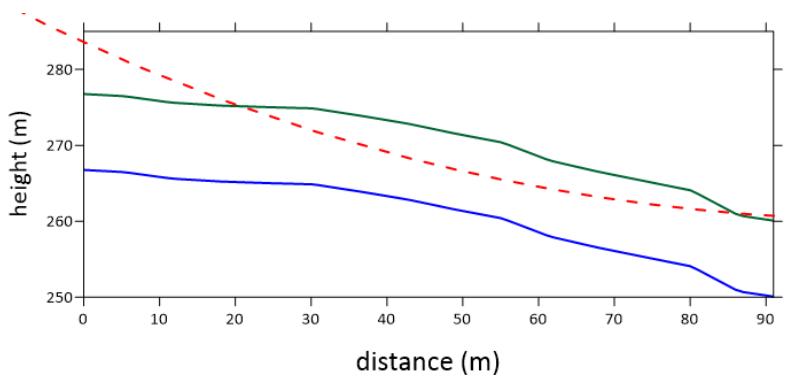

Figure 6.23. Second configuration for profile 3. The blue line represents the 10 meter interface while the green line is the topographic profile. The red dashed curve is the selected sliding surface.

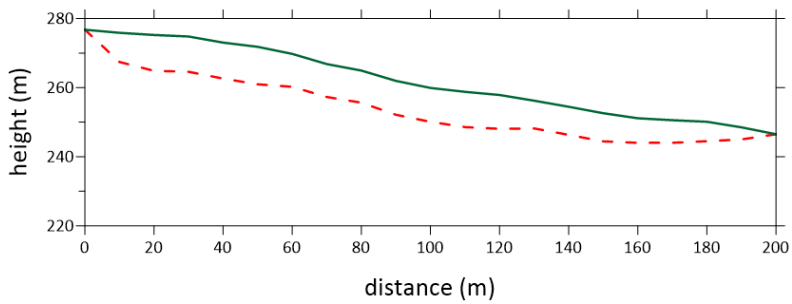

Figure 6.24. Polyline profile (in green) with a sliding surface at 10 meters depth (red dashed line). The red line represents also the interface between the two layers.

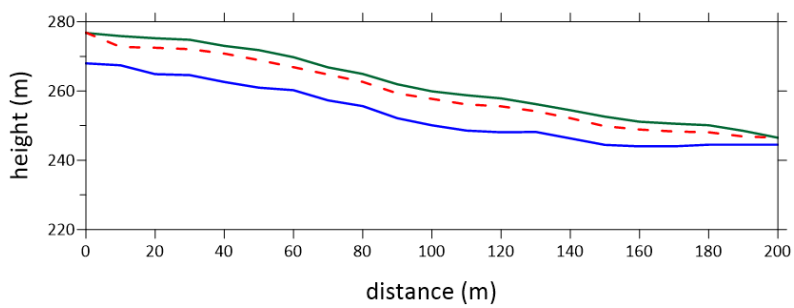

Figure 6.25. Polyline profile (in green) with a sliding surface at 2 meters depth (red dashed line). The blue line represents the 10 meters interface between the two layers.

Table 6.6. Results of the MLD stability analysis. FoS less than or equal to one are highlighted in yellow.

Configuration name	Maximum sliding surface depth (m)	FoS Case 1	FoS Case 2	FoS Case 3	FoS Case 4	FoS Case 5
Profile 1 - C1	5	3.90	2.99	2.23	1.55	1.08
Profile 1 - C2	8	3.40	2.65	2.06	1.42	0.91
Profile 2 - C1	5	3.83	2.92	2.16	1.51	1.06
Profile 2 - C2	10	3.16	2.46	1.92	1.29	0.82
Profile 3 - C1	6	4.74	3.58	2.62	1.85	1.33
Profile 3 - C2	4	3.22	2.42	1.75	1.26	0.91
Profile 4 - C1	6	4.54	3.44	2.55	1.78	1.26
Profile 4 - C2	5	4.83	3.66	2.67	1.90	1.35
Profile 5 - C1	4	4.02	2.98	2.13	1.54	1.14
Profile 5 - C2	6	4.12	3.07	2.17	1.58	1.18
Profile 6 - C1	6	3.70	2.83	2.13	1.48	1.00
Profile 6 - C2	8	3.90	3.03	2.32	1.59	1.04
Polyline	2	3.63	2.65	2.16	1.67	1.18
Polyline	10	3.73	2.94	2.35	1.57	0.98

6.3.2 SOCP-FEM application

The second stability analysis performed at the Salse del Dragone site utilizes the SOCP-FEM method. This algorithm's advantage is that it does not require a predefined sliding surface, making it particularly useful for minimizing uncertainties related to the surface's location.
However, the version of the software available to us was not capable of handling a layered slope with distinct cohesion and friction angle. Therefore, the first step in this phase of the study involved modifying the code accordingly and benchmarking it. The details of this process will be presented prior to discussing the stability analysis results.

Code Improvements: layered slope

The improvements introduced in our code involve cohesion and friction angle. Specifically, we added the ability to handle a vertically layered slope with an arbitrary number of layers. The required input geotechnical parameters are now the cohesion and friction angle for each layer, along with the density of the entire slope, which in this phase is assumed to be homogeneous. Additionally, the code requires the mesh for the entire slope and a set of points to interpolate in order to define the interfaces between the layers. These modifications were benchmarked against the work of Sarkar and Chakraborty [10]. The initial setup consists of a simple synthetic slope, as shown in Figure 6.26. In our analysis, we maintained the following fixed configuration:

- The entire slope is homogeneous, with a density of 20 kN/m^3;
- The half height of the profile, denoted as H in Figure 6.26, is 20 meters;
- The slope's angle of inclination, β, is 45°.

Table 6.7 presents the results obtained with our modified SOCP-FEM code alongside those used for benchmarking. As can be noted, the difference between the solutions in terms of FoS is minimal, always below 3%. This satisfactory result gives us confidence that the modifications made are correct.

Moreover, these modifications could also be useful in considering the influence of rainfall in slope stability analysis.

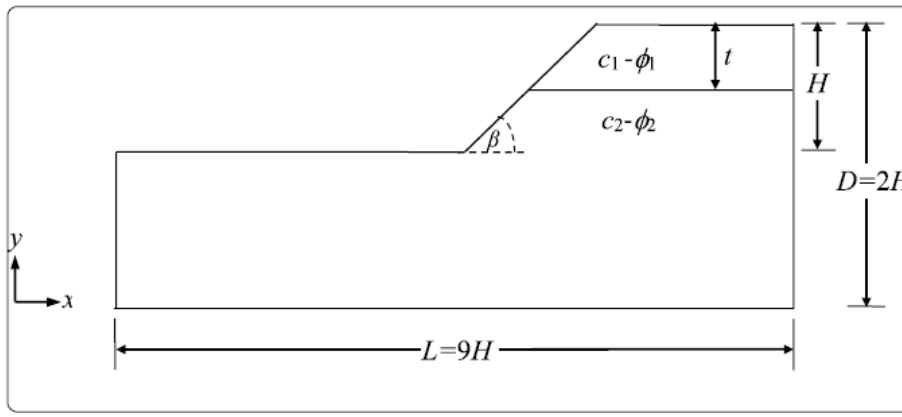

Figure 6.26. Sketch of the layered slope used in this study, modified after [10].

Table 6.7. Comparison of SOCP-FEM and Sarkar and Chakraborty [10] results in terms of Factor of Safety for different top layer thickness, cohesion, and friction angle.

Top layer thickness	c_1,c_2(kPa)	ϕ_1,ϕ_2 (°)	SOCP-FEM	Sarkar and Chakraborty (2021)
0.5 D	5, 10	35, 20	0.98	0.98
0.5 D	5, 10	40, 20	1.10	1.09
0.5 D	0, 5	35, 25	0.73	0.71
0.5 D	8, 20	45, 25	1.44	1.43
0.2 D	5, 10	35, 20	0.74	0.75
0.2 D	5, 10	40, 20	0.75	0.76
0.2 D	0, 5	35, 25	0.72	0.70
0.2 D	8, 20	45, 25	1.09	1.10

SOCP-FEM results

The stability analysis conducted with the SOCP-FEM method relies on the same six straight profiles and the polyline used in the MLD case. We performed our analysis varying the geotechnical parameter as described in Table 6.5. The results are collected in Table 6.8.

Table 6.8. Results of the stability analysis conducted with SOCP-FEM for the 5 different combination of geotechnical parameters and the seven profile examined. FoS less than or equal to one are highlighted in yellow.

	FoS Case 1	FoS Case 2	FoS Case 3	FoS Case 4	FoS Case 5
Profile 1	2.98	2.36	1.80	1.09	0.75
Profile 2	2.77	2.17	1.76	1.00	0.69
Profile 3	2.41	1.86	1.30	0.86	0.61
Profile 4	3.37	2.37	1.55	0.94	0.83
Profile 5	2.66	2.08	1.55	0.97	0.67
Profile 6	2.48	1.90	1.43	0.89	0.62
Polyline	2.62	2.11	1.53	0.94	0.66

The analysis shows a more conservative behavior compared to the one carried out with the MLD. In this case, all profiles result to be unstable in Case 5 and either unstable or near instability in Case 4. It is important to emphasize that in both cases (4 and 5) the selected geotechnical parameters are not very plausible (at least if referring to the entire upper layer), as they represent a very weak soil. Furthermore, it should be noted that the two approaches (SOCP-FEM and MLD) are not directly comparable, since in the case of MLD we have to select the sliding surface as an input. However, both analyses lead to the same conclusion, i.e. the Salse del Dragone slope is stable. The most plausible hypothesis to explain the interface at 10 meters, identified by the seismic characterization of the soil, is that it is due to the accumulation of material resulting from the mud volcano over time.

Conclusions

The importance of studying slope stability has grown significantly due to the increasing impact of climate change on natural hazards. Changes in precipitation patterns and more frequent extreme weather events are contributing to the instability of slopes worldwide.

Also in connection to this pressing issue, this thesis presents an in-depth analysis of slope stability, conducted across various geomorphological settings utilizing advanced numerical methods such as the Second Order Cone Programming-Finite Element Method (SOCP-FEM) and more traditional approaches such as the Limit Equilibrium Method (LEM) in its Minimum Lithostatic Deviation (MLD) formulation.
This thesis aims to develop a detailed and rigorous methodology for analyzing slope stability, tackling significant uncertainties and enhancing understanding in complex geotechnical contexts. It focuses on using multiple terrain profiles to reduce uncertainty, incorporates extensive parametric testing to evaluate geotechnical parameters, and employs cross-validation of methods to ensure the reliability of findings. Ultimately, the thesis strives to establish new standards in slope stability assessment, combining thorough methodological approaches with practical applications across diverse settings. Moreover, by applying these methods to synthetic models and real-case scenarios, including the Vado Ligure submarine slope, the Tavernola landslide, and the Salse del Dragone mud volcano, this work demonstrates the robustness and versatility of these techniques in diverse geological contexts.

The first application presented, the synthetic slope, clearly validate the robustness of the SOCP-FEM approach, that is able to obtain a reliable Factor of Safety even with coarse meshes. Moreover, this application helped us in determining a new sliding surface extraction strategy: from the computation of a new defined quantity S, derived from the strain tensor, we were able to discriminate a narrow band and to extract a reliable sliding surface by a simple

cubic spline interpolation procedure.
The validation process of the extracted sliding surface was performed primarily by means of the MLD method. We used the extracted surfaces as input for the MLD method, and tested the validity through the FoS computation. The results indicate a strong agreement between our method and traditional approaches, demonstrating not only accuracy but also the capacity of our model to consistently capture the morphology of sliding surfaces. The close match between our calculated Factor of Safety values and those reported in the literature [11], highlights the reliability of our approach. Furthermore, the progressive convergence observed with mesh refinement increase suggests that our method maintains stability, confirming its robustness for geotechnical applications.

This strategy was then applied to the real-case scenario of the Tavernola landslide. In this case we were able to compare our extracted sliding surface with one retrieved by geotechnical measurements [8]. The results of this analysis proved that, despite some discrepancies, our method offers a reasonable approximation of the actual sliding surface. It is worth noticing, in fact, that our method is applied to a continuous and homogeneous mass, not considering weak layers and rupture surfaces that exist in every real configuration, and that can be captured only by detailed geotechnical investigations.
Furthermore we developed a Proof of Concept that links the slope stability analysis and the consequent sliding surface extraction to the dynamic simulation of the landslide and of the landslide generated wave (if the landslide happens to enter a water body, as in the case of the Tavernola landslide, located on the slopes bordering the Iseo lake). We created an easy-to-use solution that connects the different stages of analysis, ensuring consistent, accurate, and efficient simulations that can be used in various case studies.

The Vado Ligure case study aims to illustrate the MLD method application to a more complex scenario: here, we dealt with the seabed stability of submarine canyons affected by seismic loading. The main objectives of this chapter were to demonstrate how to proceed operationally when conducting an extensive study of an area subject to multiple uncertainties (e.g., PGA values, geotechnical parameters, etc.). Essentially, it is considered good practice to perform a sensitivity analysis by varying not only the studied profiles but also

the seismic load and geotechnical parameters, especially when these are not known with certainty. Additionally, since the MLD method requires a sliding surface as input, varying this surface (as done here using circular arcs) is also necessary.

Lastly, we performed an in-depth analysis of the Salse del Dragone mud volcano (Emila-Romagna, Italy).
We formed a dedicated research group to effectively address all the necessary stages for investigating a previously unexamined site. We utilized Structure from Motion photogrammetry for the geomorphological characterization of the site, followed by active and passive seismic surveys. From these seismic data, we were able to derive the shear wave velocity profiles of the soil and identify an impedance contrast at a depth of 10 meters, which guided us in the subsequent stability analysis.
The stability analysis was performed in order to discriminate if that impedance contrast can indicate the sliding surface of a landslide. We used both the MLD and SOCP-FEM method, considering multiple transects, varying the geotechnical parameters of the soil and, in the specific case of MLD method, considering different sliding surfaces at different depths. The analysis results indicate the overall stability of the slope, supporting the hypothesis that the 10 meter interface is due to the accumulation of material resulting from the mud volcano over time.

The future developments of this work can be manifold. First of all, refining the strategy for extracting the sliding surface. Our method produces smooth and curvilinear surfaces, which may not reveal local minima that could be important for characterizing the landslide surface more realistically. Exploring the use of a different quantity, other than S, or a different interpolation method should be considered. Next, developing the proof of concept designed for the Tavernola landslide to a fully-fledged stage. With 2D stability codes available, the study could be extended to more cross-sections, obtaining multiple curves to interpolate and create a 3D landslide surface. At that point, using the PFEM software integrated into Kratos Multiphysics [68], it would be possible to conduct 3D simulations of wave propagation in the basin and assess their realism. Lastly, the same SOCP-FEM code could be further modified to also consider submarine environments and the effects of rainfalls.

Acknowledgements

I would like to thank first my supervisors, Prof. Filippo Zaniboni and Prof. Alberto Armigliato, for their constant support, help, and the invaluable lessons I have learned from them. I have not only had the privilege of learning from outstanding teachers, but I have also had the pleasure of getting to know wonderful people.
I would also like to express my heartfelt thanks to all the colleagues I collaborated with over the past three years, for their guidance and support in completing various parts of this work. In particular, I wish to thank Dr. Enrico Paolucci, who made the surveys at the Salse del Dragone enjoyable despite the many challenges, and Prof. Alessandro Franci, whose help, not only during my three months in Barcelona but also in encouraging me to believe in my abilities, has been truly meaningful.

It would take an entire book to thank those who, beyond being colleagues, have become dear friends and companions in this adventure. Starting with Letizia, always by my side, a constant source of light in the midst of life's challenges; and Cesare, whose dark humor and random anecdotes I simply can't do without. I am also deeply grateful to Suzanne, for sharing the ups and downs of this turbulent PhD journey; Riccardino (yes, I know you hate that name), Anastasia, and Giulia, for the laughter, the tears, the support, and for always being there.
I would also like to thank Riccardone, for the love he gives me every day, for making me laugh even when everything seems to be falling apart, and for his invaluable expertise as a pest control specialist–especially against those damn bed bugs.
I also thank Mara, for being purrfect in everything she does.

Lastly, I want to thank my family. I thank my brother, Steve, without whom I wouldn't have even considered studying physics (maybe I shouldn't thank you for that), and for all the support and laughter. Thank you to Anna, for putting up with and supporting my brother, and for being a friend as well as a sister-in-law. I also want to thank little Virginia: you don't know it yet, but your aunt is ready to introduce you to the magic of physics!
I thank my mother, Susan, my biggest fan, and the strongest woman I know. I love you, and without you, none of this would have been possible.

Bibliography

[1] M. J. Froude and D. N. Petley, "Global fatal landslide occurrence from 2004 to 2016", *Natural Hazards and Earth System Sciences*, vol. 18, no. 8, pp. 2161–2181, 2018.

[2] C. Bianchi and P. Salvati, "Rapporto Periodico sul Rischio posto alla Popolazione italiana da Frane e Inondazioni", *Istituto di Ricerca per la Protezione Idrogeologica (IRPI). Consiglio Nazionale delle Ricerche (CNR).*, 2022.

[3] L. Wang, X. Zhang, F. Zaniboni, E. Oñate, and S. Tinti, "Mathematical optimization problems for particle finite element analysis applied to 2D landslide modeling", *Mathematical Geosciences*, vol. 53, no. 1, pp. 81–103, 2021.

[4] M. ApS, "The MOSEK optimization toolbox for MATLAB manual. Version 10.1." http://docs.mosek.com/latest/toolbox/index.html, 2024.

[5] S. Tinti and A. Manucci, "A new computational method based on the minimum lithostatic deviation (MLD) principle to analyse slope stability in the frame of the 2-D limit-equilibrium theory", *Natural Hazards and Earth System Sciences*, vol. 8, no. 4, pp. 671–683, 2008.

[6] A. Rovida, M. Locati, R. Camassi, B. Lolli, and P. Gasperini, "The Italian ingegneria catalogue CPTI15", *Bulletin of Earthquake Engineering*, vol. 18, no. 7, pp. 2953–2984, 2020.

[7] DISS Working Group, "DISS, Version 3.3.0: A compilation of potential

sources for earthquakes larger than M 5.5 in Italy and surrounding areas. Istituto Nazionale di Geofisica e Vulcanologia (INGV)." https://diss.ingv.it/index.php, 2021.

[8] G. Crosta, P. Frattini, C. Lanfranconi, G. Sala, M. Cremonesi, and A. Franci, "Relazione sugli Scenari di Massima dell'espandimento della frana di Monte Saresano", Politecnico di Milano, Università degli Studi di Milano Bicocca, UNIMIB, EG4RISK, UPC - Barcelona, Tech. Rep., 2021.

[9] A. Mazzini and G. Etiope, "Mud volcanism: An updated review", *Earth-Science Reviews*, vol. 168, pp. 81–112, 2017.

[10] S. Sarkar and M. Chakraborty, "Stability analysis for two-layered slopes by using the strength reduction method", *International Journal of Geo-Engineering*, vol. 12, no. 1, p. 24, 2021.

[11] Y. Cheng, T. Lansivaara, and W. Wei, "Two-dimensional slope stability analysis by limit equilibrium and strength reduction methods", *Computers and Geotechnics*, vol. 34, no. 3, pp. 137–150, 2007.

[12] F. Ai, A. Förster, S. Stegmann, and A. Kopf, "Geotechnical characteristics and slope stability analysis on the deeper slope of the Ligurian margin, Southern France", in *Landslide Science for a Safer Geoenvironment: Volume 3: Targeted Landslides*. Springer, 2014, pp. 549–555.

[13] M. Picozzi, S. Parolai, and D. Albarello, "Statistical Analysis of Noise Horizontal-to-Vertical Spectral Ratios (hvsr)", *Bulletin of the Seismological Society of America*, vol. 95, no. 5, pp. 1779–1786, 10 2005.

[14] S. Sammarini, C. Lucente, U. Ugoccioni, and D. Travaglini, "Relazione Geologica Geomorfologica Emilia-Romagna ", Regione Emila-Romagna, Tech. Rep.

[15] D. J. Varnes, "Landslide types and processes", *Landslides and engineering practice*, vol. 24, pp. 20–47, 1958.

[16] S. L. Gariano and F. Guzzetti, "Landslides in a changing climate", *Earth-Science Reviews*, vol. 162, pp. 227–252, 2016.

[17] A. S. Dhakal and R. C. Sidle, "Distributed simulations of landslides for different rainfall conditions", *Hydrological Processes*, vol. 18, no. 4, pp. 757–776, 2004.

[18] R. Sidle and H. Ochiai, "Processes, prediction, and land use", *Water resources monograph. American Geophysical Union, Washington*, vol. 525, 2006.

[19] M. J. Crozier, "Deciphering the effect of climate change on landslide activity: A review", *Geomorphology*, vol. 124, no. 3-4, pp. 260–267, 2010.

[20] S. Seneviratne, N. Nicholls, D. Easterling, C. Goodess, S. Kanae, J. Kossin, Y. Luo, J. Marengo, K. McInnes, M. Rahimi *et al.*, "Changes in climate extremes and their impacts on the natural physical environment", 2012.

[21] H. Lee, K. Calvin, D. Dasgupta, G. Krinner, A. Mukherji, P. Thorne, C. Trisos, J. Romero, P. Aldunce, K. Barret *et al.*, "IPCC, 2023: Climate Change 2023: Synthesis Report, Summary for Policymakers. Contribution of Working Groups I, II and III to the Sixth Assessment Report of the Intergovernmental Panel on Climate Change [Core Writing Team, H. Lee and J. Romero (eds.)]. IPCC, Geneva, Switzerland." 2023.

[22] Rocscience Inc., *Slide2 Version 2023 – 2D Limit Equilibrium Slope Stability Analysis*, Rocscience Inc., Toronto, Ontario, Canada, 2023, available at www.rocscience.com.

[23] Geostru, *Slope stability analysis user manual*, Geostru Software s.a.s., Italy, 2025, available at https://help.geostru.eu/pdf/Slope_EN.pdf.

[24] Seequent (GeoStudio), *Stability Modelling with GeoStudio*, Seequent (GeoStudio), Canada, 2022, available at https://www.geoslope.support/

kb/article/10-geostudio-reference-manuals/.

[25] Oasys Group, *Slope Tutorial Manual*, Oasys Group, England, 2013, available at https://www.oasys-software.com/wp-content/uploads/2018/04/Slope-Tutorial-Manual.pdf.

[26] Bentley Advancing Infrastructure, *Plaxis Scientifc Manual 2D*, Bentley Advancing Infrastructure, 2024.

[27] Itasca, *FLAC - Fast Lagrangian Analysis of Continua, Version 8. Online User's Manual*, Itasca Consulting Group, Inc., 2024, available at https://docs.itascacg.com/.

[28] H. Yu, R. Salgado, S. Sloan, and J. Kim, "Limit analysis versus limit equilibrium for slope stability", *Journal of Geotechnical and Geoenvironmental Engineering*, vol. 124, no. 1, pp. 1–11, 1998.

[29] F. Tschuchnigg, H. Schweiger, S. W. Sloan, A. V. Lyamin, and I. Raissakis, "Comparison of finite-element limit analysis and strength reduction techniques", *Géotechnique*, vol. 65, no. 4, pp. 249–257, 2015.

[30] W. Fellenius, *Erdstatische Berechnungen mit Reibung und Kohäsion (Adhäsion) und unter Annahme kreiszylindrischer Gleitflächen.* W. Ernst & Sohn, 1927.

[31] A. W. Bishop, "The use of the slip circle in the stability analysis of slopes", *Geotechnique*, vol. 5, no. 1, pp. 7–17, 1955.

[32] N. Morgenstern and V. Price, "The analysis of the stability of general slip surfaces", *Geotechnique*, vol. 15, no. 1, pp. 79–93, 1965.

[33] E. Spencer, "A method of analysis of the stability of embankments assuming parallel inter-slice forces", *Geotechnique*, vol. 17, no. 1, pp. 11–26, 1967.

[34] N. Janbu, "Slope stability computations", *Publication of: Wiley (John) and Sons, Incorporated*, 1973.

[35] S. Tinti and A. Manucci, "Gravitational stability computed through the limit equilibrium method revisited", *Geophysical Journal International*, vol. 164, no. 1, pp. 1–14, 2006.

[36] D. C. Drucker and W. Prager, "Soil mechanics and plastic analysis or limit design", *Quarterly of applied mathematics*, vol. 10, no. 2, pp. 157–165, 1952.

[37] D. Drucker, "Limit analysis of two and three dimensional soil mechanics problems", *Journal of the Mechanics and Physics of Solids*, vol. 1, no. 4, pp. 217–226, 1953.

[38] J. Kim, R. Salgado, and J. Lee, "Stability Analysis of Complex Soil Slopes using Limit Analysis", *Journal of Geotechnical and Geoenvironmental Engineering*, vol. 128, no. 7, pp. 546–557, 2002.

[39] A. Kaur and R. Sharma, "Slope stability analysis techniques: a review", *International Journal of Engineering Applied Sciences and Technology*, vol. 1, no. 4, pp. 52–57, 2016.

[40] T. Matsui and K.-C. San, "Finite Element Slope Stability Analysis by Shear Strength Reduction Technique", *Soils and Foundations*, vol. 32, no. 1, pp. 59–70, 1992.

[41] L. Li, C. Tang, W. Zhu, and Z. Liang, "Numerical analysis of slope stability based on the gravity increase method", *Computers and Geotechnics*, vol. 36, no. 7, pp. 1246–1258, 2009.

[42] L. Wang, X. Zhang, and S. Tinti, "Shallow landslides modeling using a particle finite element model with emphasis on landslide evolution", *Earth Surface Dynamics Discussions*, vol. 2019, pp. 1–19, 2019.

[43] E. Reissner, "On a variational theorem in elasticity", *Journal of Mathematics and Physics*, vol. 29, no. 1-4, pp. 90–95, 1950.

[44] Y. M. Cheng, "Location of critical failure surface and some further stud-

ies on slope stability analysis", *Computers and geotechnics*, vol. 30, no. 3, pp. 255–267, 2003.

[45] M. A. Paparo, F. Zaniboni, and S. Tinti, "The Vajont landslide, 9th october 1963: limit equilibrium model for slope stability analysis through the minimum lithostatic deviation method", *Italian journal of engineering geology and environment*, pp. 583–592, 2013.

[46] M. A. Paparo and S. Tinti, "Analysis of seismic-driven instability of Mt. Nuovo in the Ischia Island, Italy", *Bulletin of the seismological society of America*, vol. 107, no. 2, pp. 750–759, 2017.

[47] ——, "Sensitivity analysis and stability charts for uniform slopes computed via the MLD methods in the frame of the limit equilibrium theory", in *EGU General Assembly Conference Abstracts*, 2013, pp. EGU2013–4223.

[48] Z. Zou, Y. Luo, Y. Tao, J. Wang, and H. Duan, "Shear constitutive model for various shear behaviors of landslide slip zone soil", *Landslides*, pp. 1–15, 2024.

[49] S. W. Jeong, "Determining the shear resistance in landslides with respect to shear displacement and shearing time in drainage-controlled ring shear tests", *Applied Sciences*, vol. 12, no. 11, p. 5295, 2022.

[50] A. Franci and X. Zhang, "3D Numerical simulation of free-surface Bingham fluids interacting with structures using the PFEM", *Journal of Non-Newtonian Fluid Mechanics*, vol. 259, pp. 1–15, 2018.

[51] D. Griffiths and P. Lane, "Slope stability analysis by finite elements", *Géotechnique*, vol. 51, pp. 653–654, 09 2001.

[52] F. Zaniboni, A. Armigliato, E. Paolucci, S. Tinti, and M. Zanetti, "Studio e ricerca sui maremoti inerenti al progetto emergenziale relativo all'ormeggio off-shore di una nave FSRU", University of Bologna – Department of Physics and Astronomy "Augusto Righi", Tech. Rep.

[53] "MaGIC", https://github.com/pcm-dpc/MaGIC, Accessed: 15/10/2024.

[54] M. Stucchi, A. Akinci, E. Faccioli, P. Gasperini, L. Malagnini, C. Meletti, V. Montaldo, and G. Valensise, "Redazione della Mappa di Pericolosità Sismica prevista dall'Ordinanza PC del 20 marzo 2003, n. 3274, All. 1 Rapporto Conclusivo", 2004.

[55] C. Meletti and V. Montaldo, "Stime di pericolosità sismica per diverse probabilità di superamento in 50 anni: valori di ag. Progetto INGV-DPC S1, Deliverable D2", 2007.

[56] A. Franci, M. Cremonesi, U. Perego, G. Crosta, and E. Oñate, "3D simulation of Vajont disaster. Part 1: Numerical formulation and validation", *Engineering Geology*, vol. 279, p. 105854, 2020.

[57] A. Bini, D. Corbari, P. Falletti, M. Fassina, C. R. Perotti, and A. Piccin, "Morphology and geological setting of Iseo Lake (Lombardy) through multibeam bathymetry and high-resolution seismic profiles", *Swiss Journal of Geosciences*, vol. 100, pp. 23–40, 2007.

[58] S. Lauterbach, E. Chapron, A. Brauer, M. Hüls, A. Gilli, F. Arnaud, A. Piccin, J. Nomade, M. Desmet, U. von Grafenstein, and D. Participants, "A sedimentary record of Holocene surface runoff events and earthquake activity from Lake Iseo (Southern Alps, Italy)", *The Holocene*, vol. 22, no. 7, pp. 749–760, 2012.

[59] L. Garibaldi, V. Mezzanotte, M. C. Brizzio, M. Rogora, and R. Mosello, "The trophic evolution of Lake Iseo as related to its holomixis", *Journal of limnology*, vol. 58, no. 1, pp. 10–19, 1999.

[60] A. Bini, M. B. Cita, and M. Gaetani, "Southern Alpine lakes—Hypothesis of an erosional origin related to the Messinian entrenchment", *Marine Geology*, vol. 27, no. 3-4, pp. 271–288, 1978.

[61] S. Santambrogio, "Valutazione dello stato di attività della frana del ver-

sante orientale del Monte Saresano e sulla sua possibile evoluzione", Studio Geoter, Tech. Rep., 2021.

[62] N. Casagli, G. Crosta, C. Di Prisco, and R. De Franco, "Studio di approfondimento della frana del Monte Saresano nel comune di Tavernola Bergamasca (BG)", Politecnico di Milano, Università Milano Bicocca, Università degli Studi di Firenze, Tech. Rep., 2021.

[63] F. Zaniboni, A. Armigliato, S. Tinti, C. Angeli, G. Gallotti, and M. Zanetti, "Studio numerico del potenziale tsunami generato nel Lago d'Iseo dalla frana del Monte Saresano", Alma Mater Studiorum – Università di Bologna, Tech. Rep., 2021.

[64] A. Gens, J. Hutchinson, and S. Cavounidis, "Three-dimensional analysis of slides in cohesive soils", *Geotechnique*, vol. 38, no. 1, pp. 1–23, 1988.

[65] M. Fredlund, "Three-dimensional limit equilibrium slope stability benchmarking", 09 2011.

[66] L. Zhang, W. Gong, X. Li, X. Tan, C. Zhao, and L. Wang, "A comparison study between 2D and 3D slope stability analyses considering spatial soil variability", *Journal of Zhejiang University-SCIENCE A*, vol. 23, no. 3, pp. 208–224, 2022.

[67] T. Pipatpongsa, K. Fang, C. Leelasukseree, and A. Chaiwan, "Stability analysis of laterally confined slope lying on inclined bedding plane", *Landslides*, vol. 19, no. 8, pp. 1861–1879, 2022.

[68] P. Dadvand, R. Rossi, and E. Oñate, "An object-oriented environment for developing finite element codes for multi-disciplinary applications", *Archives of computational methods in engineering*, vol. 17, pp. 253–297, 2010.

[69] V. M. Ferrándiz, P. Bucher, R. Zorrilla, S. Warnakulasuriya, R. Rossi, A. Cornejo, J. C. Dalmau, C. Roig, J. Maria, T. Teschemacher, M. Masó, G. Casas, M. Núñez, P. Dadvand, S. Latorre, I. de Pouplana, J. I.

González, A. Franci, F. Arrufat, R. Tosi, A. Ghantasala, K. B. Sautter, P. Wilson, D. Baumgaertner, B. Chandra, A. Geiser, I. Lopez, L. Luís, J. González-Usúa, and J. Gárate, "Kratosmultiphysics/kratos: Release v9.5", Apr. 2024.

[70] R. P. Mulligan, A. Franci, M. Celigueta, and W. A. Take, "Simulations of landslide wave generation and propagation using the particle finite element method", *Journal of Geophysical Research: Oceans*, vol. 125, no. 6, 2020.

[71] S. R. Idelsohn, E. Oñate, and F. D. Pin, "The particle finite element method: a powerful tool to solve incompressible flows with free-surfaces and breaking waves", *International journal for numerical methods in engineering*, vol. 61, no. 7, pp. 964–989, 2004.

[72] E. Oñate, S. R. Idelsohn, F. Del Pin, and R. Aubry, "The particle finite element method—an overview", *International Journal of Computational Methods*, vol. 1, no. 02, pp. 267–307, 2004.

[73] E. Oñate, S. R. Idelsohn, M. A. Celigueta, and R. Rossi, "Advances in the particle finite element method for the analysis of fluid–multibody interaction and bed erosion in free surface flows", *Computer methods in applied mechanics and engineering*, vol. 197, no. 19-20, pp. 1777–1800, 2008.

[74] E. Oñate, "Derivation of stabilized equations for numerical solution of advective-diffusive transport and fluid flow problems", *Computer methods in applied mechanics and engineering*, vol. 151, no. 1-2, pp. 233–265, 1998.

[75] ——, "A stabilized finite element method for incompressible viscous flows using a finite increment calculus formulation", *Computer methods in applied mechanics and engineering*, vol. 182, no. 3-4, pp. 355–370, 2000.

[76] ——, "Possibilities of finite calculus in computational mechanics", *International journal for numerical methods in engineering*, vol. 60, no. 1, pp. 255–281, 2004.

[77] L. I. Dimitrov, "Mud volcanoes—the most important pathway for degassing deeply buried sediments", *Earth-Science Reviews*, vol. 59, no. 1-4, pp. 49–76, 2002.

[78] ——, "Mud volcanoes—a significant source of atmospheric methane", *Geo-Marine Letters*, vol. 23, pp. 155–161, 2003.

[79] G. Etiope, "Natural gas seepage–The Earth's hydrocarbon degassing", *Springer International Publishing*, p. 199, 2015.

[80] B. M. S. Giambastiani, M. Antonellini, M. Nespoli, M. Bacchetti, A. Calafato, M. Conventi, A. Dadomo, G. Martinelli, M. Morena, S. Venturoli *et al.*, "Mud flow dynamics at gas seeps-Nirano Salse, Italy", *Environmental Earth Sciences*, vol. 81, no. 19, p. 480, 2022.

[81] G. Etiope, G. Martinelli, A. Caracausi, and F. Italiano, "Methane seeps and mud volcanoes in Italy: gas origin, fractionation and emission to the atmosphere", *Geophysical Research Letters*, vol. 34, no. 14, 2007.

[82] G. Martinelli, S. Cremonini, E. Samonati *et al.*, *Geological and geochemical setting of natural hydrocarbon emissions in Italy.* InTech Rijeka, Croatia, 2012.

[83] S. Baylis, S. Cawley, C. Clayton, and M. Savell, "The origin of unusual gas seeps from onshore Papua New Guinea", *Marine Geology*, vol. 137, no. 1-2, pp. 109–120, 1997.

[84] J. Traynor and C. Sladen, "Seepage in Vietnam—onshore and offshore examples", *Marine and Petroleum Geology*, vol. 14, no. 4, pp. 345–362, 1997.

[85] J. Thrasher, D. Strait, and R. A. Lugo, "Surface geochemistry as an

exploration tool in the south caribbean", 1996.

[86] A. J. Kopf, "Significance of mud volcanism", *Reviews of geophysics*, vol. 40, no. 2, pp. 2–1, 2002.

[87] A. Revil, "Genesis of mud volcanoes in sedimentary basins: A solitary wave-based mechanism", *Geophysical research letters*, vol. 29, no. 12, pp. 15–1, 2002.

[88] A. Mazzini, "Mud volcanism: Processes and implications", *Marine and Petroleum Geology*, vol. 26, no. 9, pp. 1677–1680, 2009, mud Volcanism: Processes and Implications.

[89] P. Clari, S. Cavagna, L. Martire, and J. Hunziker, "A Miocene mud volcano and its plumbing system: a chaotic complex revisited (Monferrato, NW Italy)", *Journal of Sedimentary Research*, vol. 74, no. 5, pp. 662–676, 2004.

[90] B. P. Istadi, G. H. Pramono, P. Sumintadireja, and S. Alam, "Modeling study of growth and potential geohazard for LUSI mud volcano: East Java, Indonesia", *Marine and Petroleum Geology*, vol. 26, no. 9, pp. 1724–1739, 2009.

[91] L. Bombicci, *Descrizione della mineralogia generale della Provincia di Bologna.* Gamberini e Parmeggiani, 1873.

[92] Regione Emilia-Romagna. (2024) Salse del Dragone o di Sassuno. [Online]. Available: https://geo.regione.emilia-romagna.it/schede/geositi/scheda.jsp?id=140

[93] G. Etiope, G. Martinelli, and A. Caracausi, "Methane seeps and mud volcanoes in Italy: Gas origin, fractionation and emission to the atmosphere", *Geophysical Research Letters*, vol. 34, pp. 14 303–, 07 2007.

[94] A. Pesci, S. Amoroso, G. Teza, and L. Minarelli, "Characterization of soil deformation due to blast-induced liquefaction by UAV-based pho-

togrammetry and terrestrial laser scanning", *International Journal of Remote Sensing*, vol. 39, no. 22, pp. 8317–8336, 2018.

[95] F. Remondino, M. G. Spera, E. Nocerino, F. Menna, and F. Nex, "State of the art in high density image matching", *The photogrammetric record*, vol. 29, no. 146, pp. 144–166, 2014.

[96] S. I. Granshaw and C. S. Fraser, "Computer vision and photogrammetry: Interaction or introspection?" pp. 3–7, 2015.

[97] M. Westoby, J. Brasington, N. Glasser, M. Hambrey, and J. Reynolds, "'Structure-from-Motion' photogrammetry: A low-cost, effective tool for geoscience applications", *Geomorphology*, vol. 179, pp. 300–314, 2012.

[98] G. Teza, A. Pesci, and A. Ninfo, "Morphological analysis for architectural applications: Comparison between laser scanning and structure-from-motion photogrammetry", *Journal of Surveying Engineering*, vol. 142, no. 3, p. 04016004, 2016.

[99] D. G. Lowe, "Object recognition from local scale-invariant features", in *Proceedings of the seventh IEEE international conference on computer vision*, vol. 2. Ieee, 1999, pp. 1150–1157.

[100] M. A. Fischler and R. C. Bolles, "Random sample consensus: a paradigm for model fitting with applications to image analysis and automated cartography", *Communications of the ACM*, vol. 24, no. 6, pp. 381–395, 1981.

[101] A. Pesci and G. Teza, "Precisione della nuvola di punti SfM: considerazioni e test." INGV, Tech. Rep., 2016.

[102] A. Pesci, G. Teza, and F. Loddo, "Scale factor for SfM point cloud analysis: considerations", INGV, Tech. Rep., 2021.

[103] Agisoft, "Description of PhotoScan software". [Online]. Available: https://www.agisoft.com/

[104] S. Kramer, *Geotechnical Earthquake Engineering.* Prentice Hall, New Jersey, USA, 1996.

[105] S. Parolai, "Investigation of site response in urban areas by using ingegneria data and seismic noise", in *New manual of seismological observatory practice 2 (NMSOP-2).* Deutsches geoforschungszentrum gfz, 2012, pp. 1–38.

[106] C. B. Park, R. D. Miller, and J. Xia, "Multichannel analysis of surface waves", *Geophysics*, vol. 64, no. 3, pp. 800–808, 1999.

[107] G. di Lavoro, *Linee guida per le buone pratiche dell'analisi delle onde superficiali.* CNR Edizioni, 2021.

[108] R. T. Lacoss, E. J. Kelly, and M. N. Toksöz, "Estimation of seismic noise structure using arrays", *Geophysics*, vol. 34, no. 1, pp. 21–38, 1969.

[109] J. Capon, "High-resolution frequency-wavenumber spectrum analysis", *Proceedings of the IEEE*, vol. 57, no. 8, pp. 1408–1418, 1969.

[110] E. Ólafsdóttir, S. Erlingsson, and B. Bessason, "Tool for analysis of MASW field data and evaluation of shear wave velocity profiles of soils", *Canadian Geotechnical Journal*, vol. 55, 07 2017.

[111] B. Gutenberg, "Microseisms", ser. Advances in Geophysics, H. Landsberg and J. Mieghem, Eds. Elsevier, 1958, vol. 5, pp. 53–92.

[112] S. Bonnefoy-Claudet, F. Cotton, and P.-Y. Bard, "The nature of noise wavefield and its applications for site effects studies: A literature review", *Earth-Science Reviews*, vol. 79, no. 3, pp. 205–227, 2006.

[113] M. W. Asten, "Geological control on the three-component spectra of Rayleigh-wave microseisms", *Bulletin of the Seismological Society of America*, vol. 68, no. 6, pp. 1623–1636, 12 1978.

[114] D. Albarello and S. Castellaro, "Tecniche sismiche passive: indagini a stazione singola", *Ingegneria Sismica, 2, 32-61*, 2012.

[115] Y. Nakamura, "A method for dynamic characteristics estimation of subsurface using microtremor on the ground surface", *Railway Technical Research Institute, Quarterly Reports*, vol. 30, no. 1, 1989.

[116] S. Ling and H. Okada, "An Extended Use of the Spatial Autocorrelation Method for the Estimation of Geological Structure Using Microtremors." *Proceedings of the 89th SEGJ Conference, Japanese, 44-48. (In Japanese)*, 1993.

[117] M. Ohori, A. Nobata, and K. Wakamatsu, "A comparison of ESAC and FK methods of estimating phase velocity using arbitrarily shaped microtremor arrays", *Bulletin of the Seismological Society of America*, vol. 92, no. 6, pp. 2323–2332, 2002.

[118] D. Albarello, C. Cesi, V. Eulilli, F. Guerrini, E. Lunedei, E. Paolucci, D. Pileggi, and L. M. Puzzilli, "The contribution of the ambient vibration prospecting in seismic microzoning: An example from the area damaged by the April 6, 2009 L'Aquila (Italy) ingegneria", *Bollettino di Geofisica Teorica ed Applicata*, vol. Vol. 52, pp. 513–538, 09 2011.

[119] J. W. Cooley and J. W. Tukey, "An algorithm for the machine calculation of complex Fourier series", *Mathematics of computation*, vol. 19, no. 90, pp. 297–301, 1965.

[120] Geostru Software, "GEOSTRU database", https://help.geostru.eu/slope/it, Accessed: 03/10/2024.